Dark matter decay feature search toward the Galactic bulge and halo

Master's Thesis in Physics

Presented by

Katharina Egg

September 28, 2023

Dr. Karl Remeis-Sternwarte
Friedrich-Alexander-Universität Erlangen-Nürnberg

Supervisor: Prof. Dr. Manami Sasaki

Abstract

The nature of dark matter has been one of the fundamental unsolved questions of physics and astrophysics since its discovery in the mid-20th century. Among a great variety of theories, one popular microscopic dark matter candidate today is the proposed sterile neutrino, a heavy neutrino addition to the Standard Model of Physics, that interacts only gravitationally. Sterile neutrinos could be detectable through a decay into photons at X-ray or higher energies. Further discussion on this was sparked by the detection of an unidentified emission line at $\sim 3.5\,\mathrm{keV}$ by Bulbul et al. (2014), that was associated with sterile neutrino decay and also seen in other surveys. While non-detections of this line have rendered its status as a possible dark matter decay feature uncertain in the years since, the possibility of sterile neutrino decay lines at X-ray energies remains an interesting and much discussed path for potential indirect dark matter detections.
In the present work a search for dark matter decay lines was conducted in eROSITA X-ray data. Three regions in a semicircle of $\sim 30°$ west of the Galactic center were analyzed. All point sources in the regions were excluded and spectra were extracted for eRASS1 to 4. The diffuse X-ray background was then modeled using a modified version of the spectral model by Ponti et al. (2022). The residuals of the spectral fits were then scanned for line features. In all regions and eRASS 56 line features with a detection significance of $> 3\sigma$ could be identified. All of these lines are, however, in range to be associated with known atomic lines. It was also shown that a contribution from charge exchange might be possible for all detected lines.
The present survey thus found no unidentified emission lines that could be associated with sterile neutrino decay. Closer studies of the detected lines in future surveys might, however, lead to more detailed conclusions on their origins. Especially the improved energy calibration announced for the 030 data processing version might further refine the present results.

Table of Contents

List of Figures

1. Introduction

Astronomy and astrophysics have always been disciplines characterized by their massive impact on the human self-perception, in regards to questions of religion as well as to our place and its importance - or non-importance - within the universe. While the Copernican revolution fundamentally changed the human perspective in regards to our place in the Solar System, most new scientific insights today do not have similar impacts on the general public, even while actively changing the scientific perspective on extremely large scales, such as the discovery of gravitational waves or quantum mechanics.

The process of reevaluating our fundamental scientific knowledge and our perspective on the universe meanwhile remains ongoing and is part of science and scientific discovery.
Often the path to new science can additionally only be cleared through technological advances. New technologies can enable measurements of effects that have already been proposed on the basis of theory, such as stellar parallaxes or gravitational waves, or lead to completely new ideas. In this vein the entire discipline of X-ray astronomy, astronomy studying light at X-ray wavelengths, for instance, remained out of reach until the 1960s when it became possible to take measurements using rockets, and later, satellites above Earth's atmosphere, which blocks out all X-ray light (Seward and Charles, 2010).

The well-known fundamental basis for many walks of physics and astrophysics today is the Standard Model of Physics, which contains both the basic fundamental particles of matter and the four fundamental forces governing their interactions. However, while the Standard Model seems to comprehensively describe the fundamentals of physics, it is nowadays also known that there are a certain aspects not yet covered and described by it, leaving fundamental questions in our view of physics, astrophysics, and the universe that remain the object of active research towards their resolution (Demtröder, 2017; Boyarsky et al., 2019).

The first, and, within this work, foremost, question is the question of dark matter. While its presence and existence in our universe has been proven, its nature remains virtually unknown and is not explained by the Standard Model (Boyarsky et al., 2019).
The second question is that of neutrino oscillations. It is well known and documented that neutrinos can shift between different sets of eigenstates and change their masses in the process. The cause of this process is, however, unknown (Boyarsky et al., 2019).
The third question is the question of the baryon asymmetry in the universe. It is believed that during a period of annihilation of matter and antimatter this baryon asymmetry was the reason for the presence of matter in the universe today. Its origin, however, is also unknown (see references in Boyarsky et al., 2019).

The fourth and, at this point, final question is that of the hot big bang, which is thought to have been the origin of our universe and which set the initial conditions for the later development of structures and the universe as we know it. How this process worked, however, remains unknown as well (Boyarsky et al., 2019).

While all of these open questions are of great importance and represent fundamental aspects of physics and astrophysics, the present work will focus on only the first of them: the question of dark matter.

Different approaches and models of what dark matter could consist of exist. One popular idea in this regard is the proposal of additional heavy neutrinos that could play the role of dark matter particles. The direct detection of such a neutrino would, however, be exceedingly difficult. This, fortunately, is where the aforementioned X-ray astronomy can help: according to theoretical frameworks sterile neutrinos should be detectable via monochromatic X-ray emission caused by their decay (see references in Boyarsky et al., 2019).

The search for such line features in eROSITA X-ray data is the purpose of this work. First an overview over the background of the associated research areas and topics will be given. Then the eROSITA telescope and mission will be introduced. Afterwards the steps of the data analysis, the line detection, and its results will be described and discussed thoroughly. Then, finally, a summary of the present work and an outlook toward possible future scientific efforts will be given.

2. Astrophysical and research background

In this first chapter the astrophysical background and research background of the research question will be introduced as a basis for the following data analysis. In this context the question of dark matter and its potential detection via X-ray decay lines as well as the composition of the diffuse X-ray background will be discussed.

2.1. Dark matter

Dark matter is, as previously mentioned, one of the large scale phenomena that point to the existence of physics beyond the Standard Model. In this section a short overview over the subject matter and different theoretical models will be given. The main focus hereby, however, lies on sterile neutrinos as dark matter candidates as a popular approach and also as an approach in which the detection of decay products could potentially be possible at X-ray energies.

2.1.1. Discovery and overview

The question of dark matter made its debut in the early to mid-20th century as the answer to many different physical and astronomical inconsistencies. While the first to propose the existence of dark matter was Zwicky (1933), who suggested the existence of a dark matter halo to explain the observed velocity distribution in the Coma galaxy cluster, it became clear over time that dark matter was a factor in many phenomena, such as the behavior of the rotation curve of the Andromeda galaxy and the movement of the Milky Way and the Andromeda galaxy toward one another (see references in Frenk and White, 2012).

Throughout the 1970s the question of dark matter became intrinsically linked with the evolution of the universe and the fundamental formation of structures. These ideas were further refined in the course of the 1980s. The addition of dark matter allowed for a far earlier formation of structures during a period where regular matter would not be able to form structures, as photons had not decoupled from the primordial plasma yet. A period of cosmic inflation could produce small density perturbations that would act as the "seeds" of structure formation. It was also first proposed that the nature of dark matter could be non-baryonic. While Standard Model neutrinos were being discussed as possible dark matter candidates, it became clear that other, heavier particles could also be viable candidates for microscopic dark matter (see references in Frenk and White, 2012 and Boyarsky et al., 2019).

Different classifications for models emerged according to the proposed particle mass and energy: Hot dark matter (HDM), warm dark matter (WDM), and cold dark matter (CDM). The convention in differentiating these categories is the following: HDM is produced relativistic and stays so during the time of structure formation. WDM, on the other hand, is produced relativistic but is not so anymore during structure formation. CDM, however, is always non-relativistic (Boyarsky et al., 2019).
Standard Model neutrinos constitute a possible candidate of HDM, while CDM could be composed of axions or supersymmetric particles. Possible candidates for WDM, meanwhile, could be sterile neutrinos (see references in Frenk and White, 2012).

The subsequent formation of structures in the universe is expected to produce radically different results depending on the category of the model in question. While HDM models can only directly form large structures, such as galaxy clusters, that would then need to fragment down into smaller structures, CDM can produce small objects, that can grow and cluster together over time to form large scale structures. WDM, meanwhile, falls into the middle of these two extremes. While it can directly form smaller structures than HDM, structures far below the size of galaxies remain an impossibility. Comparing simulations of structure formation to the, in the 1980s newly available, Center for Astrophysics (CfA) observational data of the actual large scale structures in our universe (Davis et al., 1982), similar to those that are shown in the SDSS map in Figure 2.1, where the large scale "cosmic web" can be seen very clearly, led to (at first most, later all) HDM models being disproved as unphysical, as their predicted behavior does not reflect the actual structure of the universe (see references in Frenk and White, 2012).

These findings lead to Standard Model neutrinos being excluded from the list of possible candidates for dark matter. However, there is yet another criterion proposed dark matter particles have to fulfill: the Tremaine-Gunn bound. This lower bound for the mass of dark matter particles arises as a result of phase space considerations, as the density of the dark matter can not exceed that of degenerate Fermi gas. This limits the mass of dark matter particles to above a few hundred eV - which is far too high for Standard Model neutrinos to be able to constitute all of dark matter, further disqualifying them as possible candidates (Tremaine and Gunn, 1979; see references in Boyarsky et al., 2019).

As this leaves no viable Standard Model dark matter candidate, it is consequently generally assumed today that the nature of dark matter lies outside the Standard Model. Many different theoretical approaches to this question exist - none of which could consequently be proven so far. What is well known, however, is the density of dark matter in the universe, as it has been measured by Planck Collaboration et al. (2020):

$$\Omega_{\mathrm{DM}} h^2 = 0.120 \pm 0.001$$

A number of theories on microscopic dark matter exist, many of which are focused on CDM models, that are well-embedded in the theoretical Λ cold dark matter (ΛCDM) framework,

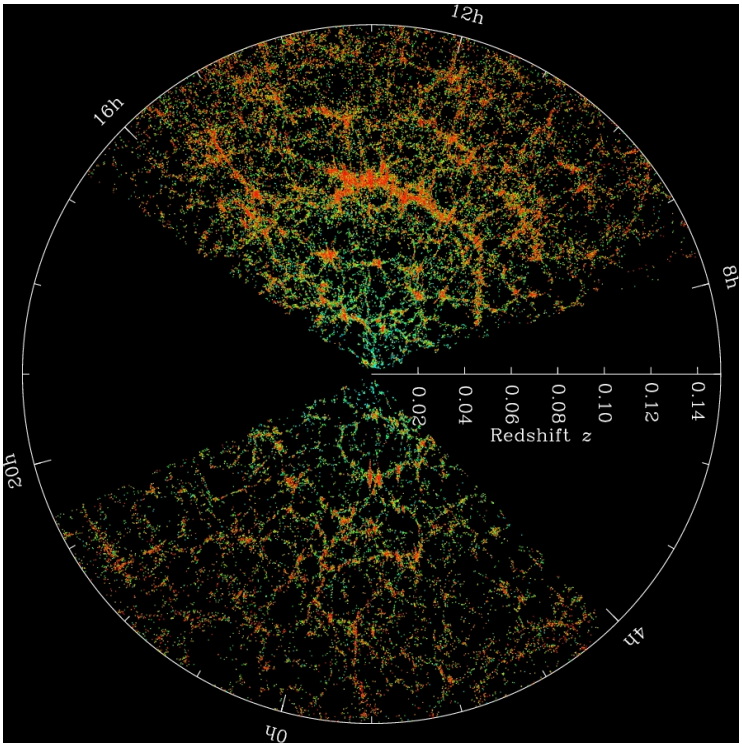

Figure 2.1.: SDSS map of the universe showing the cosmic web structure, each dot corresponds to a galaxy (Image Credit: M. Blanton and SDSS, taken from SDSS and Blanton (2014))

which describes a universe with CDM that expands driven by a cosmological constant Λ (Fließbach, 2016; see references in Frenk and White, 2012).
One compelling candidate for the role of dark matter are weakly interacting massive particles (WIMPs). WIMPS have high masses from GeV to TeV ranges, they satisfy the Tremaine-Gunn bound, and their theoretical density is in accordance with the density of dark matter. What makes the idea of WIMPs especially popular is also the fact that their existence could solve the gauge hierarchy problem, another unsolved question of physics. However, WIMPs could so far not be detected in either colliders or dark matter searches, leaving the question of their existence unanswered (see references in Boyarsky et al., 2019).

Another popular candidate for dark matter is the one this work is going to focus on: sterile neutrino dark matter.

2.1.2. Sterile neutrinos as dark matter candidates

This section will discuss the general theoretical basis of sterile neutrinos before focusing on a specific theoretical framework for their implementation, the Neutrino Minimal Standard Model (νMSM), and its implications for sterile neutrino dark matter and possible detection channels.

General theoretical approaches

Theories of sterile neutrino dark matter propose additional neutrino flavors to the ones known from the Standard Model to fulfill the role of dark matter. This is a natural ansatz for an expansion the Standard Model, as it fits in seamlessly with the known mass oscillations of Standard Model neutrinos and could even explain the so-called "mass puzzle", i.e. the extremely low mass of neutrinos as compared to other fermions (Boyarsky et al., 2019; Povh et al., 2014).

To explain the extremely low mass of neutrinos, a pure Dirac framework requires their Yukawa coupling to the Higgs field to be extremely small - in the eyes of many researchers, unnaturally so. This fact suggests that this mechanism might be more complicated than first expected.
By proposing that neutrinos are Majorana particles, the picture changes. Under this assumption a neutrino would be its own antiparticle, i.e. $\nu \equiv \overline{\nu}$. This adds a new mass term to its Lagrangian, containing its Majorana mass M (Thomson, 2013):

$$\begin{aligned} \mathcal{L} &= -\frac{1}{2}\left[m_D \overline{\nu_L}\nu_R + m_D \overline{\nu_R^c}\nu_L^c + M\overline{\nu_R^c}\nu_R\right] + h.c. = \\ &= -\frac{1}{2}\begin{pmatrix}\overline{\nu_L} & \overline{\nu_R^c}\end{pmatrix}\begin{pmatrix}0 & m_D \\ m_D & M\end{pmatrix}\begin{pmatrix}\nu_L^c \\ \nu_R\end{pmatrix} + h.c. \end{aligned} \tag{2.1.1}$$

In this equation m_D refers to the Dirac mass, $\nu_{L/R}$ to left/righthanded neutrinos, ν^c to a CP-conjugated state and $h.c.$ to the hermitian conjugate of the beforehand term (Thomson, 2013).

By finding the eigenvalues of this mass matrix, two distinct possible mass states can be obtained for each neutrino. Under the assumption that $M \gg m_D$, this results in (Thomson, 2013):

$$|m_\nu| \approx \frac{m_D^2}{M} \quad , \qquad m_N \approx M \tag{2.1.2}$$

Here m_ν refers to a light neutrino mass state, representing the known extremely light neutrino masses, while m_N refers to a proposed, considerably heavier, heavy mass state (Thomson, 2013).

This approach is known as the seesaw mechanism and could solve the "mass puzzle". While the order of magnitude of the Dirac mass couplings could match those of the other

fermions, the mass of the light neutrino state would still be suppressed by the Majorana mass term. The "seesaw" in this case refers to the fact that the mass of the light neutrino mass state decreases when the mass of the heavy neutrino mass state and the Majorana mass increases - a logical seesaw (Thomson, 2013; see references in Boyarsky et al., 2019).

The heavy mass state would now provide us with a heavy neutrino that does not interact electromagnetically or weakly, as its state is almost entirely righthanded, with possible masses above the Tremaine-Gunn bound - a sterile neutrino and a potential viable dark matter candidate. An additional heavy sterile mass state would exist for each known massive light neutrino state (Thomson, 2013).

This cursory theoretical description of what is known as a type I seesaw can, of course, not thoroughly reflect the great variety of theoretical possibilities for sterile neutrinos. In alternate approaches, known as type II or III seesaws, the heavy neutrino masses can be generated through different mechanisms, such as an additional Higgs field. Many more factors exist in adding sterile neutrinos to the Standard Model that can be fine-tuned, such as the addition of a protecting symmetry that could cause cancellations in the mass matrix. Fine-tuning of these factors lead to a group of models known as low scale seesaws, that do not require an extreme mass scale where M surpasses the electroweak scale of 100 GeV (Thomson, 2013) - a property that would make their generation very difficult (see references in Boyarsky et al., 2019).

While it is difficult to choose from such a great variety of theoretical models, there is one model that is of particular interest, which will be investigated more closely in the following to determine possible properties and detection channels for sterile neutrino dark matter.

The νMSM and characteristics of νMSM sterile neutrino dark matter

One of the models in the framework of the low-scale seesaw is of particular interest for sterile neutrino dark matter considerations: the Neutrino Minimal Standard Model (νMSM). It is a version of a low-scale seesaw model that was developed by Asaka et al. (2005) and Asaka et al. (2007). It follows the approach of adding as few new parameters to the Standard Model as possible while also solving as many open questions of physics as possible (see references in Boyarsky et al., 2019).

In the νMSM three right-handed sterile neutrinos with masses below the electroweak scale, i.e. 100 GeV (Thomson, 2013), that govern flavor oscillations, are added to the Standard Model. Two of the neutrinos have large masses of MeV up to the electroweak scale, while the third has a keV mass and is a suitable dark matter candidate. The production of these neutrinos is highly model dependent, while they would be unstable, their lifetime could be larger than the age of the universe. The model can also explain the baryon asymmetry of the universe. One of its key characteristics is the fact that the sterile neutrinos were never in thermal equilibrium during the early age of the universe due to their weak interaction

strength with other particles (see references in Boyarsky et al., 2019 and Boyarsky et al., 2009).

Following the νMSM, characteristics and properties of sterile neutrino dark matter can be found and possible detection channels can be investigated (see references in Boyarsky et al., 2019).

Sterile neutrino dark matter particles are neutral, massive, and long-lived. Requiring their lifetime to be greater than the age of the universe of $4.4 \cdot 10^{17}\,\mathrm{s}$ puts an upper bound on the sum $\theta^2 = \sum_{\alpha=e,\mu,\tau} |\theta_\alpha|^2$ of their mixing angles with active mass states (see references in Boyarsky et al., 2019):

$$\theta < 3.3 \cdot 10^{-4} \left(\frac{10\,\mathrm{keV}}{M} \right)^5 \tag{2.1.3}$$

The number density of sterile neutrinos would need to be a lot smaller than that of Standard Model neutrinos to reach the same total mass, thus lower mass limits of the order of magnitude of 100 eV to satisfy the Tremaine-Gunn bound can be found from observations of dwarf spheroidal galaxies (see references in Boyarsky et al., 2019).

The main decay channel for a νMSM sterile neutrino N with $M \leq 2m_e$ is $N \to \nu_\alpha \nu_\beta \overline{\nu}_\beta$. Its decay width is given by (see references in Boyarsky et al., 2019):

$$\Gamma_{N\to 3\nu} = \frac{G_F^2 M^5}{96\pi^3}\theta^2 \approx \frac{1}{1.5 \cdot 10^{14}\,\mathrm{s}} \left(\frac{M}{10\,\mathrm{keV}} \right)^5 \theta^2 \tag{2.1.4}$$

A second decay channel of a radiative decay $N \to \nu + \gamma$ exists, which is suppressed by $\sim \frac{1}{128}$ compared to the aforementioned decay into three neutrinos. Its decay width is given by (see references in Boyarsky et al., 2019):

$$\Gamma_{N\to\nu+\gamma} = \frac{9\alpha G_F^2}{256\pi^4}\theta^2 M^5 = 5.5 \cdot 10^{-22}\theta^2 \left[\frac{M}{1\,\mathrm{keV}} \right]^5 \mathrm{s}^{-1} \tag{2.1.5}$$

A Feynman diagram illustrating this decay can be seen in Figure 2.2; the photon in this diagram could alternately also couple to the $W^\mp$ boson. This radiative decay produces a photon with $E = \frac{1}{2}M$. Large enough numbers of dark matter decays could thus produce monochromatic signals, that could be detected in the background of astrophysical emission at relevant wavelengths, providing a possible channel for detecting dark matter decay signatures. While other detection strategies for sterile neutrino dark matter exist (e.g. Lyman-α forest, weak lensing), the focus of this work will lie on the detection via decay lines (see references in Boyarsky et al., 2019)

Considering the lower mass limit of the order of magnitude of 100 eV, decay features with $E = \frac{1}{2}M$ could be seen from hundreds of eV upwards, making the X-ray keV-range a range

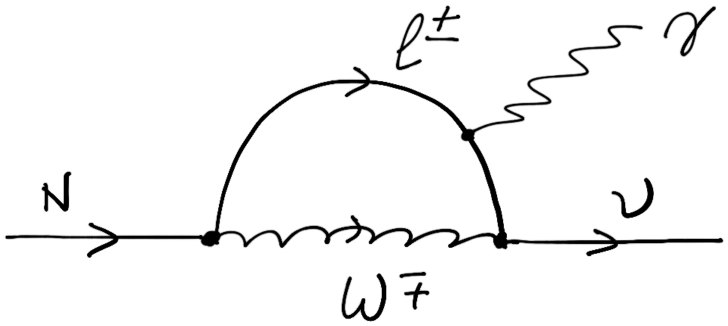

Figure 2.2.: Feynman diagram of a potential sterile neutrino decay (taken from Boyarsky et al. (2019))

of interest for the possibility of detecting sterile neutrino dark matter, which has been an object of great scientific interest in the past decade (see references in Boyarsky et al., 2019).

2.2. Discoveries of decay line features associated with sterile neutrino dark matter

The question of the possible detection of sterile neutrino decays in X-rays was elicited by the discovery of an unidentified emission line around energies of 3.5 keV by Bulbul et al. (2014).

Bulbul et al. (2014) found emission lines at energies of $(3.55 - 3.57) \pm 0.03$ keV in stacked spectra of XMM-Newton data of 73 galaxy clusters with significances $> 3\sigma$. The occurrence of the line was also confirmed in Chandra data of the Perseus Cluster.
A spectrum of their detection can be seen in Figure 2.3. The peak in the residuals at ~ 3.5 keV clearly shows the location of the detected line.

Bulbul et al. (2014) exclude an explanation of the line as atomic by meticulously modeling all lines present in the vicinity of the energy range. They further argue that effects, such as small variations in the effective detector area, can also be ruled out due to the stacking of the cluster spectra. The strongly diverging redshifts of the clusters lead to the line being effectively "smeared out" over an energy range of up to 1.2 keV during the detection. They conclude that a sterile neutrino origin of the line in $M = 7.1$ keV neutrino decays is possible and derive a mixing angle of $\sin^2(2\theta) \sim 7 \cdot 10^{-11}$.
They also stress, however, that systematic errors still play a role in these results and that their results should not be overstated (Bulbul et al., 2014).

The detection was shortly after followed by Boyarsky et al. (2014), who found a line at 3.52 ± 0.02 keV in XMM-Newton data of the Andromeda galaxy and the Perseus Cluster with significances of 2.4σ up to 4.4σ for the combined sample.

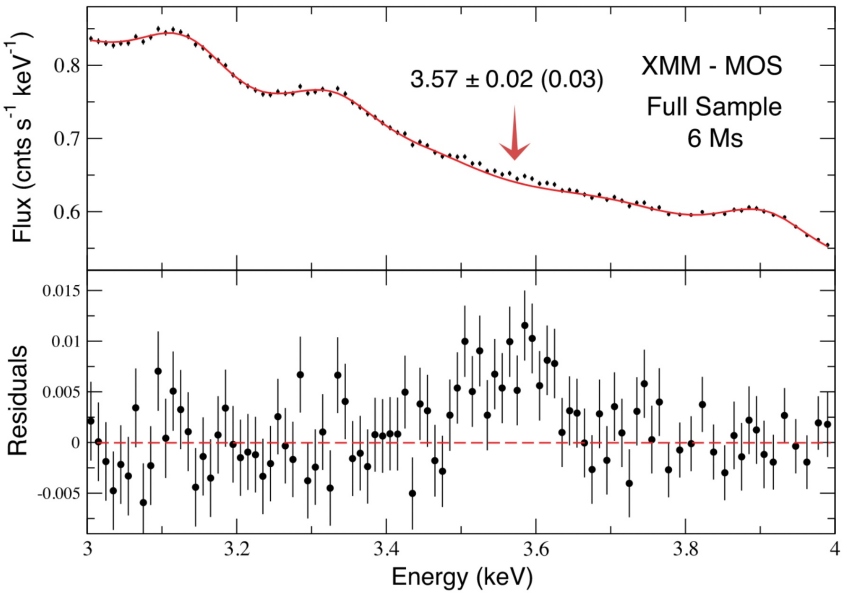

Figure 2.3.: Initial detection of the 3.5 keV line by Bulbul et al. (2014) (taken from Bulbul et al. (2014))

In the years since, many different teams have observed a large variety of different objects in an attempt to verify or refute these detections. These studies generally focus on either large scale objects, such as galaxies and galaxy clusters, or the large scale emission from within the Milky Way. This is due to the fact that galaxies, including the Milky Way, and galaxy clusters are expected to possess large scale dark matter halos. Their high concentration of dark matter makes them ideal observational targets for possible detections (see references in Boyarsky et al., 2019; Frenk and White, 2012)

Lines in the vicinity of 3.5 keV could be recovered in data of different objects through the work of many groups with a variety of instruments, for instance by Boyarsky et al. (2015), Franse et al. (2016), Urban et al. (2015), and Hofmann and Wegg (2019) (see references in Boyarsky et al., 2019 and Sicilian et al., 2020).

However, many groups also reported non-detections, e.g. Aharonian et al. (2017), Malyshev et al. (2014), Foster et al. (2021), and Dessert et al. (2023) (see references in Boyarsky et al., 2019 and Sicilian et al., 2020).

These discrepancies in the science results raise questions about the true origin of the 3.5 keV line with a number of scientists considering its dark matter origins disproved through its non-detections. Different explanations for the line have been proposed in the years since, some with different likelihoods (see references in Boyarsky et al., 2019).

A purely statistical fluctuation is considered very unlikely, considering the number of surveys that found a line at $\sim 3.5\,\mathrm{keV}$ and the high likelihoods of their detections. The highest among these is an 11.1σ likelihood for a line at $3.51 \pm 0.01\,\mathrm{keV}$ found by Neronov et al. (2016) with NuSTAR data. This detection is, however, in question, as the line energy lies close to the lower energy limit of NuSTAR and could be an instrumental feature. Neronov et al. (2016) themselves considered it connected to the instrumental background (see references in Boyarsky et al., 2019 and Sicilian et al., 2020).

Instrumental explanations for the 3.5 keV line have been proposed. The line has, however, been observed by a great number of different instruments at this point in time, which rules out many instrumental components as the line origin, such as the materials used to coat the mirrors of the telescope. It was theorized that the line might be an unknown instrumental feature of CCDs. The line has since, however, been observed with NuSTAR that, instead of CCD cameras, uses a CZT detector. As mentioned, however, the NuSTAR detections are of an uncertain nature. Additionally the 3.5 keV line has been shown to scale with the redshift of the observed object (e.g. in Bulbul et al. (2014)), which further speaks against an instrumental origin of the line (see references in Boyarsky et al., 2019 and Sicilian et al., 2020).

This leaves astrophysical mechanisms as possible non-dark matter explanations for the origin of the 3.5 keV line, such as (both unknown and known) atomic transitions. Several candidates exist that might explain the observed energy, e.g. Potassium XVIII. Gu et al. (2015) proposed that a possible origin of the 3.5 keV line might be charge exchange (CX) between neutral hydrogen and bare sulphur ions, a process in which ions pick up electrons from cold gas, that can occur in areas where hot and cold gas collide and generate additional X-ray emission. Shah et al. (2016) provided experimental evidence for CX emission at $3.47 \pm 0.06\,\mathrm{keV}$ that could explain the observed line features, which is a leading theory in non-dark matter explanations for the feature (see references in Boyarsky et al., 2019 and Sicilian et al., 2020).

As of now it must be concluded that the status of the 3.5 keV line remains uncertain and its origin unconfirmed. More data is needed to shed light onto its nature.

While most of the discussion around dark matter decay lines has been centered around the 3.5 keV line, other potential line candidates have been observed at 2.51, 8.7, 9.4, and 10.1 keV. These candidates do, however, appear to have been found in singular detections only and have thus not been met with the same excitement in the scientific community as the search for the 3.5 keV line (see references in Adhikari et al., 2017; Loewenstein and Kusenko, 2010).

In the years since the initial detection by Bulbul et al. (2014) a great number of surveys has been carried out to find traces of - or upper limits for - keV sterile neutrino dark matter. Figure 2.4 shows an overview over the constraints on sterile neutrino dark matter obtained

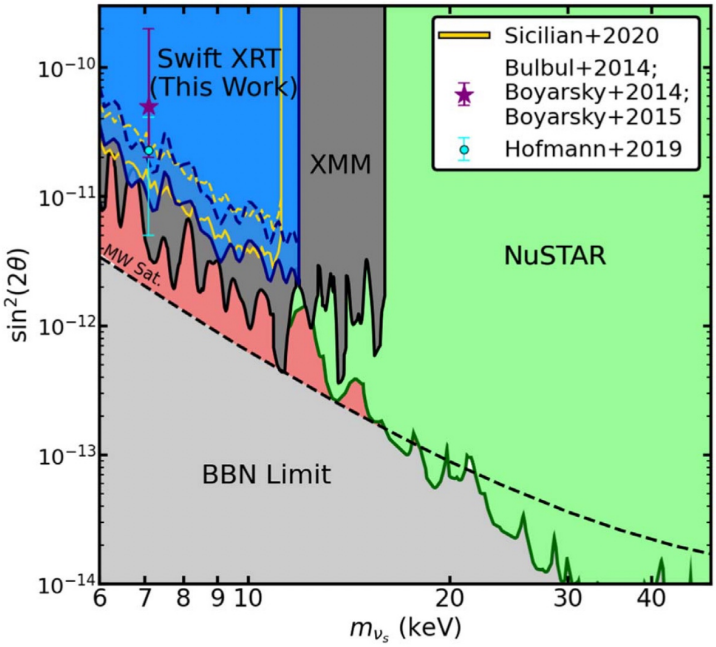

Figure 2.4.: Overview over sterile neutrino dark matter constraints obtained in previous surveys until 2022, "This Work" refers to Sicilian et al. (2022) (taken from Sicilian et al. (2022), details on the results used for this schematic can be found in that work)

until 2022. It can be seen that the available parameter space above the lower limit set by the Big Bang Nucleosynthesis (BBN) has almost entirely been ruled out by different surveys. This is, however, not yet a definite result. The parameter space labeled "MW Sat." (red in Figure 2.4) is based on parameter dependent formalisms. Meanwhile, the placement of the BBN limit is also motivated by a theoretical sterile neutrino production mechanism and, as other models might find different lower limits, possible parameter space for sterile neutrino dark matter might still exist (see Sicilian et al., 2022 and references therein).

To further constrain limits on sterile neutrino dark matter and shed light on observed decay lines further studies are needed. In this light eROSITA opens up new possibilities in observing not only a great number of objects but also objects and background emission on a large scale. This survey will in that context hope to aid in the gain of scientific knowledge.

2.3. The Galactic X-ray background

To conduct a proper survey on possible sterile neutrino dark matter decay lines in the eROSITA X-ray background, the components of the X-ray background first have to be modeled as precisely as possible. Thus an overview over all components contributing to the X-ray background is necessary. The focus hereby will lie on the factors influencing eROSITA data, as these are relevant for the following analysis of eROSITA data.

When examining the background present in X-ray data a difference must be made between the astrophysical background, that consists of photons produced by actual astrophysical processes in the field of view (FOV) outside of the telescope, and the particle/instrumental portion of the background.

2.3.1. Astrophysical background

The existence of an astrophysical X-ray background outside the Solar System was discovered by Giacconi et al. (1962) and has since been studied in great detail. It can be broken down into different components that are predominant at different energies (see references in Ponti et al., 2022).

The most powerful component of the astrophysical X-ray background over a majority of the X-ray energy range is the cosmic X-ray background (CXB). It is uniform over the entire sky and takes the shape of a powerlaw with photon index 1.45 in the $\sim 2 - 10\,\mathrm{keV}$ energy range. For higher energies this shape becomes steeper. At $\sim 30\,\mathrm{keV}$ it forms a peak. It is generally assumed that the astrophysical X-ray background above $\sim 0.5\,\mathrm{keV}$ consists of point sources, such as active galactic nuclei (AGN) and galaxy clusters, as it has been shown that more than $\sim 80\%$ and more than $\sim 92\%$ of the entire astrophysical background in the $0.5 - 2$ and $2 - 7\,\mathrm{keV}$ energy bands respectively can be resolved into point sources (see references in Ponti et al., 2022).

While the X-ray background is homogeneous over the entire sky at higher energies, ROSAT observations in the 1990s showed that this is not the case for softer energies, where additional components are present that provide additional, spatially inhomogeneously distributed contributions to the emission. It was discovered that components exist on local as well as Galactic scales (see references in Ponti et al., 2022).

At energies below $\sim 0.2\,\mathrm{keV}$ emission by the local hot bubble (LHB) dominates the X-ray background. This structure is a warm/hot bubble with a radius of $\sim 200\,\mathrm{pc}$ surrounding the sun. The LHB is thought to originate from supernova explosions following a period of massive star formation 14 Myr ago. The explosions energized the surrounding interstellar medium (ISM), causing an overpressurized environment that started expanding. Liu et al. (2017) mapped out the characteristics of the LHB using ROSAT data. They found its temperature to be uniformly distributed around $kT = 0.097\,\mathrm{keV} \pm 0.013\mathrm{keV}$ (Liu et al.,

2017; see references in Ponti et al., 2022 and Sasaki et al., 2022).

Another component influencing the X-ray spectrum at low energies below $\sim 0.2\,\mathrm{keV}$ is the emission caused by Solar wind charge exchange (SWCX), where neutral ISM flowing through the heliosphere interacts with ionised Solar wind particles. This is known as heliospheric emission. The additional magnetospheric or geocoronal emission describes the Solar wind's interactions with the Earth's atmosphere. The SWCX component is highly variable and depends on the Solar cycle as well as the direction of view with respect to the location of the sun. Finding a comprehensive model to predict the magnitude of this phenomenon has proven very difficult, as the described system is very complex and depends strongly on many factors. Models for its contribution to X-ray spectra, however, exist; details on the modeling of the SWCX component in the present analysis can be found in Section 4.3.1. The strength of the SWCX component was found to decrease with higher ecliptic latitudes/heliolatitudes with the density of the Solar wind (Yeung et al., 2023; see references in Kuntz, 2019 and Ponti et al., 2022).

Between $\sim 0.2 - 0.6\,\mathrm{keV}$ Galactic scale emission dominates the X-ray background. It has been interpreted to represent and contain several different components, such as a Galactic corona caused by a thickened disk, or a Galactic halo.
The Galactic scale emission in the eROSITA background was found to split up into two model components with different temperatures by Ponti et al. (2022). This results in two effective Galactic components, a higher temperature component with $kT \sim 0.4 - 0.7\,\mathrm{keV}$ associated with hot interstellar medium and denoted hot corona (Cor) and a lower temperature component with a temperature of about $kT \sim 0.15 - 0.25\,\mathrm{keV}$, which is denoted as circumgalactic medium (CGM) and contains all remaining contributions to Galactic emission from within the corona, halo, and other possible components.
In practice these labels do not and can not yet fully encompass and reflect the sources of emission contained therein, and their origins and properties remain as of yet not fully understood.
The potential shape and existence of halo emission around the Milky Way, for instance, is still uncertain, considering the lack of a clear picture in other galaxies. While evidence of a hot halo has been found around AGN, studies of nearby galaxies were often unable to detect extended galactic halos. Hot plasma was, however, found in thick corona-like structures above and below the disks of spiral galaxies.
Meanwhile, the Cor component has before also been interpreted to consist of emission from faint M dwarfs. It is possible that both the Galactic corona and M dwarfs contribute to this emission. However, new models of the Milky Way and its mass distribution have already challenged this result, so while a contribution from M stars is expected, the true origin of the Cor emission remains an object of scientific discussion for which further study is still needed (see references in Ponti et al., 2022).

A schematic by Ponti et al. (2022) showcasing an extremely simplified picture of the potential origins of the components discussed in this section can be seen in Figure 2.5. While

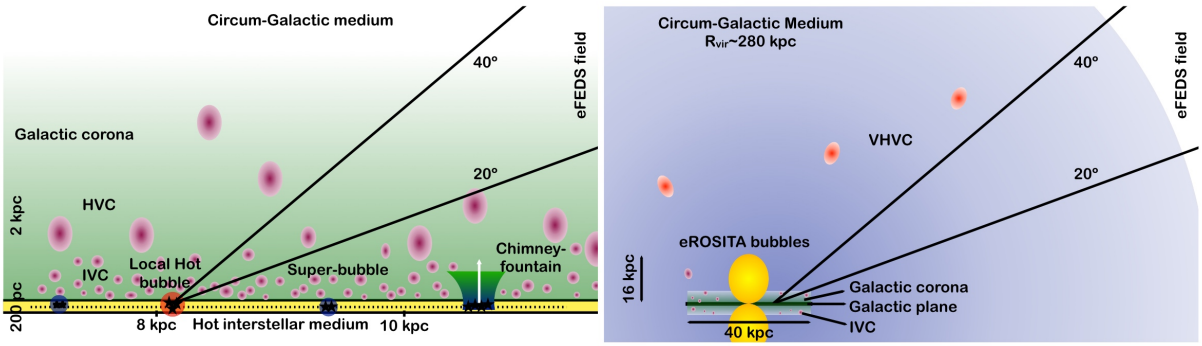

Figure 2.5.: Schematic showing the spatial origins of the different components of the astrophysical X-ray background (taken from Ponti et al. (2022))

the Solar winds causing SWCX emission are on too small a scale to be visible, in the left part of the schematic the LHB and Galactic corona can be seen. The right part of the Figure shows the Milky Way and its surrounding CGM on a larger scale. The viewing angle of the eFEDS field that was analyzed in Ponti et al. (2022) has also been drawn in.

It can be concluded that, while the main components of the astrophysical X-ray background are known from a modeling perspective, more study is needed to be able to firmly pinpoint the exact structure of especially the Galactic scale emission and the true origins of each of the background components. While it is not the purpose of this work to characterize the X-ray background, it hopes to provide interesting modeling results that might give further leads toward the endeavor of understanding the X-ray background.

2.3.2. Particle/instrumental background

In addition to the astrophysical background there are also particle and instrumental contributions to the X-ray background, that need to be accounted for in the data.

Many different factors contribute to the instrumental and particle background. High energy particles play a large role here, either hitting the CCD cameras directly or causing secondary particles or photons to be emitted. Soft protons can also hit the CCDs after being focused through the telescope mirrors; low energy electrons can also enter into the camera. Another factor to consider are X-rays from outside the FOV that are only reflected once in the mirror configuration (instead of twice as they should be). Infalling optical light can also contaminate the data (Freyberg et al., 2020).

In the construction and data taking process of eROSITA many measures have been taken to mitigate the influence of the particle/instrumental background. An optical light blocking filter reduces the optical light but is deliberately kept too thin to filter it out entirely, as it also affects soft X-rays, which is an undesirable effect. An X-ray baffle helps reduce

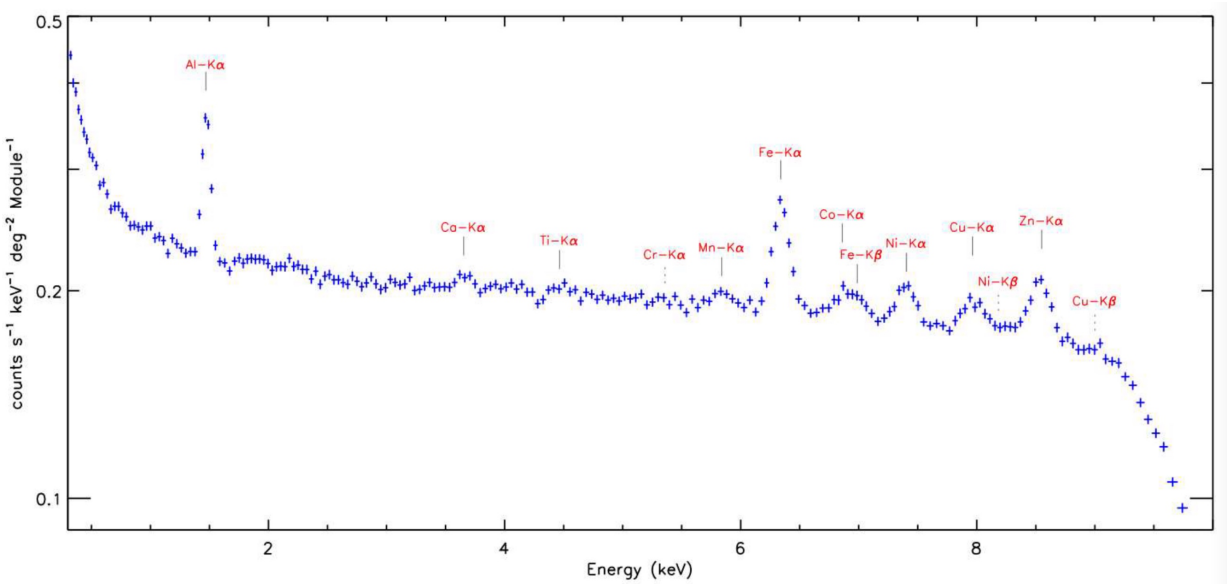

Figure 2.6.: Average CLOSED filter spectrum of eROSITA with denoted lines (taken from Freyberg et al. (2020))

the impact of single-reflected X-rays. Around bright sources an influence remains, however, that has to be accounted for for ideal modeling results. An electron deflector behind each mirror module stops electrons from entering the cameras. Minimum ionizing particle (MIP) events are further rejected through filtering by their patterns on the CCD pixels (Freyberg et al., 2020; Dennerl et al., 2020).

Any remaining particle/instrumental background has to be addressed through calibration. In eROSITA this is realized through observations with the filter in CLOSED position. An average CLOSED filter spectrum can be seen in Figure 2.6. From these measurements the FWC (filter wheel closed) model was generated by Michael Yeung, that can be used to model the particle/instrumental background. The use of this model in the present analysis is described in Section 4.3.1 (Freyberg et al., 2020).

3. eROSITA

As eROSITA data will be analyzed in the present work, an overview over the eROSITA telescope and mission will be given in this chapter. Afterwards expectations for the present research question with respect to eROSITA's technical properties and resolution will be discussed.

3.1. The eROSITA telescope and mission

The **e**xtended **RO**entgen **S**urvey with an **I**maging **T**elescope **A**rray - eROSITA is an X-ray telescope and mission. It is a German-Russian collaboration and was developed at the Max Planck Institute for Extraterrestrial Physics (MPE) in Munich in collaboration with a number of other institutes, the Dr. Karl Remeis-Sternwarte Bamberg and ECAP (FAU Erlangen-Nürnberg), the University of Hamburg Observatory, the Leibniz Institute for Astrophysics Potsdam (AIP), and the Institute for Astronomy and Astrophysics of the University of Tübingen. The Argelander Institute for Astronomy of the University of Bonn and the Ludwig Maximilians Universität Munich contributed as well; support by the DLR and the Max Planck Society was also given (Predehl et al., 2021).

eROSITA is mounted on the Spectrum-Roentgen-Gamma (SRG) satellite together with the Russian instrument Astronomical Roentgen Telescope X-ray Concentrator (ART-XC) that was developed by the Russian Space Research Institute. The SRG platform was built by the Lavochkin Association ("NPOL"). The SRG satellite was launched on July 13, 2019 from the cosmodrome in Baikonour, Kazakhstan (Predehl et al., 2021).

Images of eROSITA can be seen in Figure 3.1, Figure 3.1a shows a schematic of the inner workings of the telescope, while Figure 3.1b shows a photo taken before the launch. The telescope possesses a diameter of 1.9 m and a height of 3.2 m. It weighs 808 kg.
The key characteristic of eROSITA can already be very clearly seen in Figure 3.1: the telescope consists of 7 separate telescope modules (TMs), which are usually denoted as "TM1" to "TM7". Each TM possesses a mirror array that focuses the X-ray photons onto an individual CCD camera (see Predehl et al., 2021 and references therein).

The mirrors used in the eROSITA TMs are made of electro-formed nickel; additionally gold has been evaporated onto their reflecting side. They possess a Wolter type I shape. A schematic showcasing this configuration can be seen in Figure 3.2. In Wolter type I mirrors X-rays are reflected twice at small grazing angles before being recorded, first off a

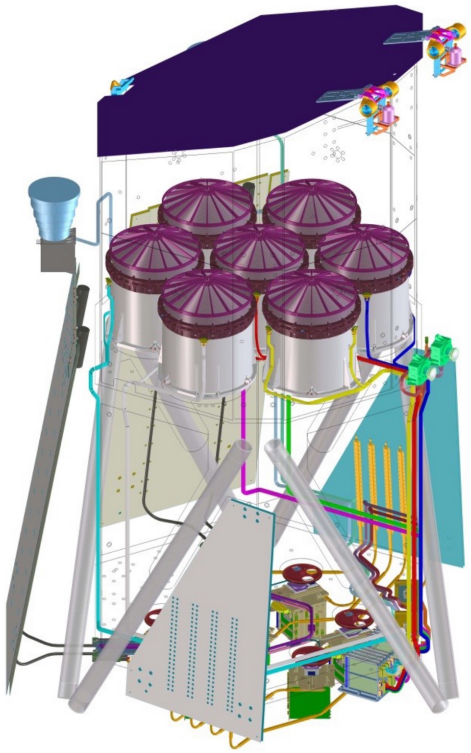

(a) Schematic of the eROSITA telescope (taken from Predehl et al. (2021))

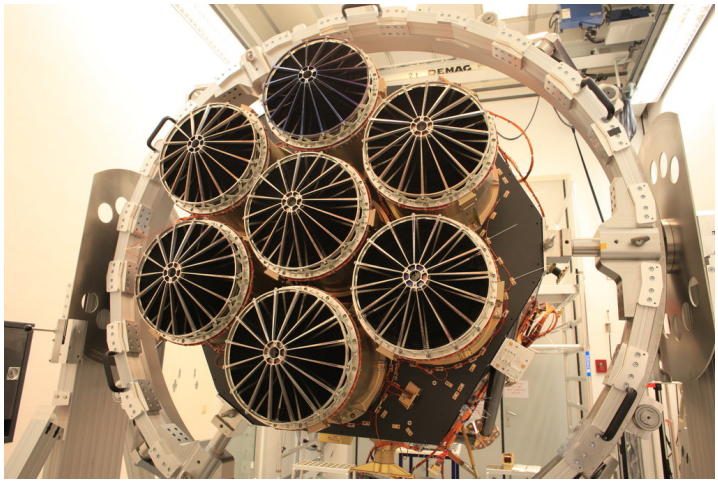

(b) Image of eROSITA taken before launch (Credit: P. Friedrich/MPE, taken from Max Planck Institute for Extraterrestrial Physics (2019))

Figure 3.1.: Images of eROSITA

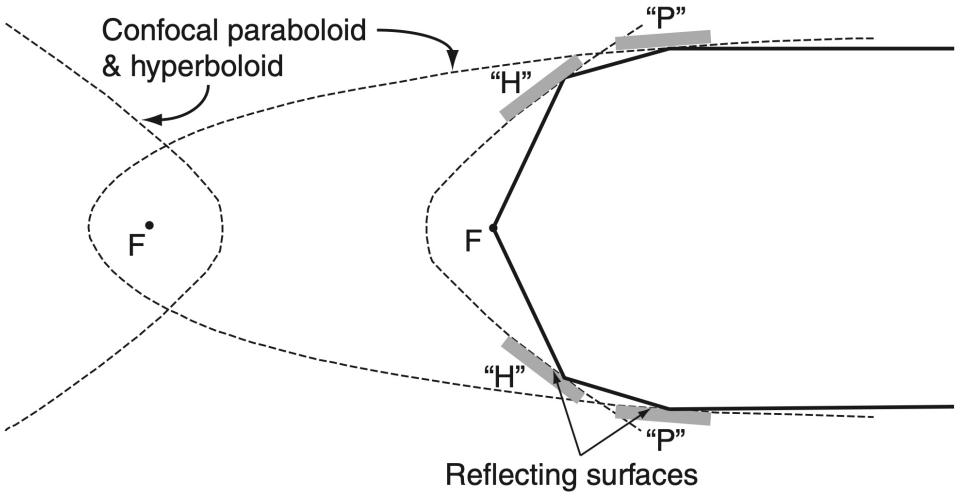

Figure 3.2.: Schematic of a Wolter type I mirror, "H" and "P" denote the paraboloid and hyperboloid surfaces, F the focal points of both (taken from Schwartz (2011))

paraboloid mirror surface ("P" in Figure 3.2), then off a hyperboloid mirror surface ("H" in Figure 3.2). This configuration comes with a variety of advantages: the focal length is significantly shortened (compared to the paraboloid configuration or other Wolter mirror types), consequently the aperture-to-focal length ratio is maximized, which is extremely advantageous in the construction and assembly of a space telescope with limited dimensions. For resolved sources the signal-to-noise is improved and, for a perfect setup which is (unrealistically) free of any contaminations, such as imperfections in the mirrors, linear distances on the detector near the axis can be directly translated into angular distances in the sky with only a linear conversion factor.
The Wolter type I shape also allows for nesting, i.e. stacking of the mirrors, which is done to increase the collection area of the TMs. Each eROSITA TM possesses a mirror array consisting of 54 stacked Wolter type I mirrors with an outer diameter of 360 mm and a focal length of 1600 mm. The average on-axis resolution of the TMs is 16.1″ half-energy width (HEW) at 1.5 keV. An invar cylinder for each mirror shell in combination with a magnetic electron deflector behind the mirror helps reduce the unwanted background of particles and single-reflected X-rays from outside the FOV, that was described in Section 2.3.2 (see Schwartz, 2011, Predehl et al., 2021, and references therein).

The mirrors of the TMs focus the X-ray photons onto the CCD cameras. The CCDs used in eROSITA have measurements of 28.8 mm × 28.8 mm and consist of 384 × 384 pixels. A single pixel thus depicts an area of 9.6″ × 9.6″. They operate at a temperature of −85 °C. The integration time of the CCDs is 50 ms. Each CCD possesses a framestore area; images are shifted there in 0.115 ms. The CCDs are then ready to resume recording, which immensely reduces "out-of-time" events that are wrongly recorded during read-out. For each CCD a copper shield helps reduce the particle background, while a graded shield is used to combat single-reflected X-ray from outside the FOV.
Each CCD has a filter wheel with four settings: OPEN, FILTER, CLOSED, and CALIB. The OPEN setting was used for the initial outgassing after the launch, while the CLOSED position is used for calibration of the particle/instrumental background, that was described in Section 2.3.2. CALIB contains a radioactive calibration source and can be used for calibration measurements. FILTER, meanwhile, is the setting for the recording of data. It has a polyimide filter that further protects the CCD from contamination. For TMs 5 and 7 an additional aluminum layer was added to the filter, while for TMs 1, 2, 3, 4, and 6 the aluminum was applied directly on top of the CCDs. During operations the latter turned out to be the better option, as it was discovered that TMs 5 and 7 suffer from optical light leaks, as can be seen in Figure 3.3, which are likely caused by this configuration. For that reason TMs 5 and 7 are often excluded from the data in research work; the same was done in the analysis in the present work (see Predehl et al., 2021 and references therein).

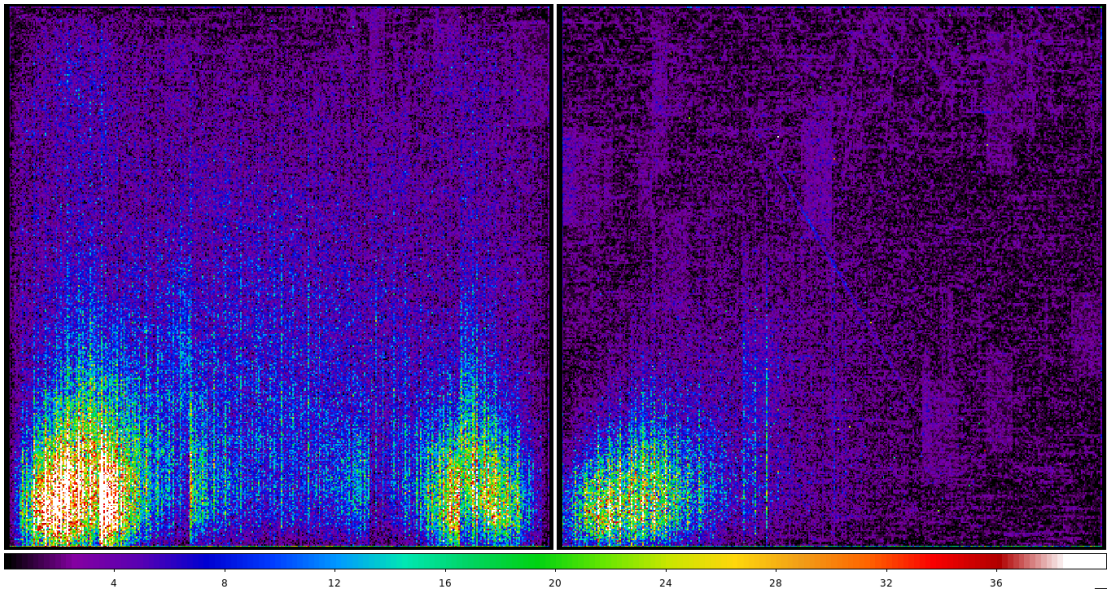

Figure 3.3.: Images of (left) TM5 and (right) TM7 with optical light leak (taken from Max Planck Institute for Extraterrestrial Physics (2021))

eROSITA is sensitive in an energy range of about $\sim 0.2 - 8\,\mathrm{keV}$, in practice often up to $10\,\mathrm{keV}$. A plot of its effective area over its energy range compared with other telescopes can be seen in Figure 3.4. It can be seen that, especially over its sensitive soft energy band of $\sim 0.2 - 2\,\mathrm{keV}$, eROSITA has a similar effective area to XMM-Newton. Meanwhile it exceeds that of ROSAT by around an order of magnitude. It also becomes clear that it is sensitive to harder energy ranges, that were not accessible to ROSAT, producing observational all-sky data in an entirely new energy band. The strengths of eROSITA become even more clear when looking at its grasp, i.e. its effective area multiplied with its FOV. The FOV of eROSITA is circular and has a diameter of 1.03°, larger than the full moon, which is advantageous for an all-sky survey. As was shown in Figure 3.4 for the effective area, Figure 3.5 shows the grasp of eROSITA over its energy range, again compared to that of other missions. It can be seen that eROSITA's grasp in its most sensitive energy range from $\sim 0.3 - 3.5\,\mathrm{keV}$ is the highest in this comparison. This further emphasizes that the capabilities of eROSITA are geared towards its task of conducting all-sky surveys (Predehl et al., 2021).

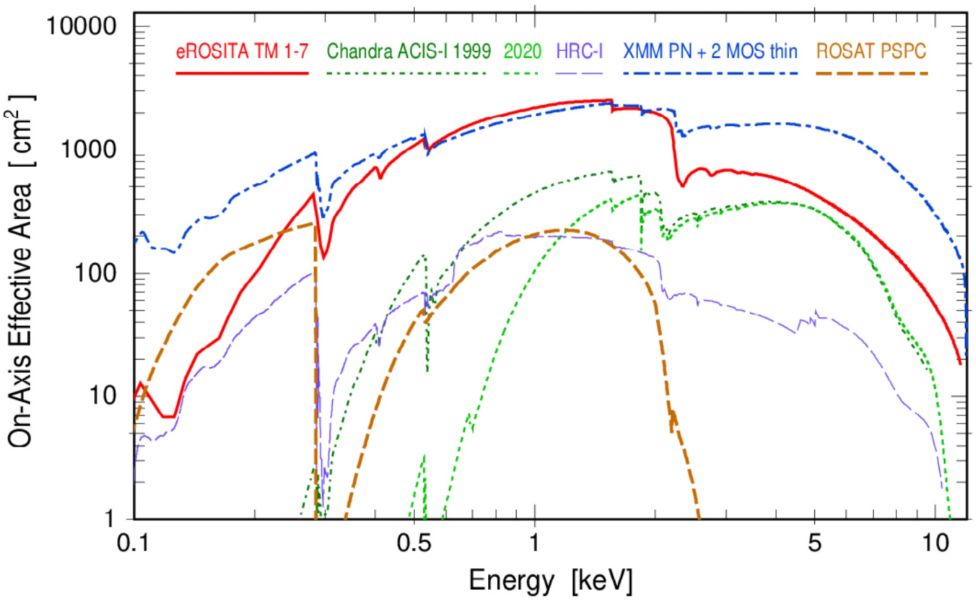

Figure 3.4.: Effective area of eROSITA over its energy range compared to other X-ray missions (taken from Predehl et al. (2021))

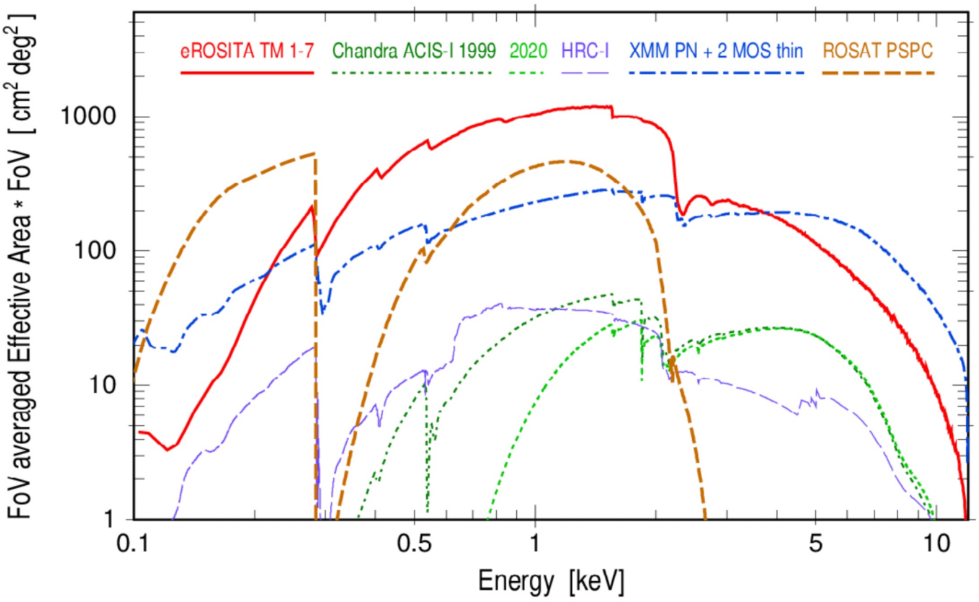

Figure 3.5.: Grasp of eROSITA over its energy range compared to other X-ray missions (taken from Predehl et al. (2021))

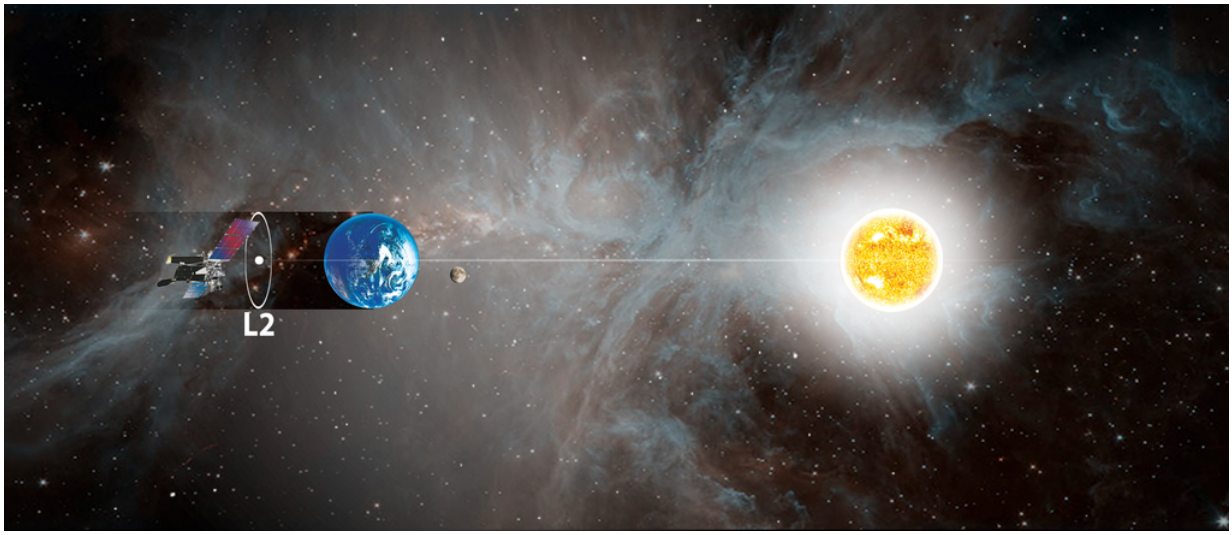

Figure 3.6.: Schematic showcasing eROSITA's orbit around L2 (Credit: Roscosmos/DLR/SRG/Lavochkin, taken from Max Planck Institute for Extraterrestrial Physics (2019))

eROSITA's main task since its start in 2019 has been performing all-sky surveys. The first all-sky survey started on December 13, 2019, exactly half a year after the start of the SRG satellite after a calibration and performance verification phase. The SRG satellite circles one of the Lagrangian points, L2, as is illustrated in Figure 3.6. The satellite additionally continuously rotates around its own axis, allowing it to scan small slivers of the sky at a time. By the satellite following and turning with Earth's movement around the sun, the entire sky can be scanned in half a year, averaging to around 1° per day. An image of the first all-sky survey of eROSITA, called eRASS1, can be seen in Figure 3.7. The Galactic plane and a number of bright X-ray sources can be seen very clearly. Also clearly visible are the two bubbles, dubbed "eROSITA bubbles", on top of and below the Galactic center. As the data of eROSITA are shared between Germany and Russia, the western (right) and eastern (left) half of the map in Galactic coordinates are referred to as the "German" and "Russian" half of the sky respectively. A narrow strip of shared data exists in the center of the map at the Galactic longitude of 0°.
The data are organized into 4700 sky tiles, segments of $3.6° \times 3.6°$ size, with overlap between neighboring tiles (Predehl et al., 2021).

In addition to the general task of creating all-sky surveys eROSITA also has a number of specific science goals that are meant to be achieved through the analysis of its all-sky data. Its main science goal is the detection of over $\sim 10^5$ galaxy clusters, that can be used to study the large scale structure formation in the universe and constrain cosmological parameters. Another goal is the investigation of active galactic nuclei (AGN) and their evolution, as eROSITA is expected to record $\sim 3 \cdot 10^6$ AGN. In the vast amount of X-ray data, a great amount of other astrophysical objects becomes accessible as well, both

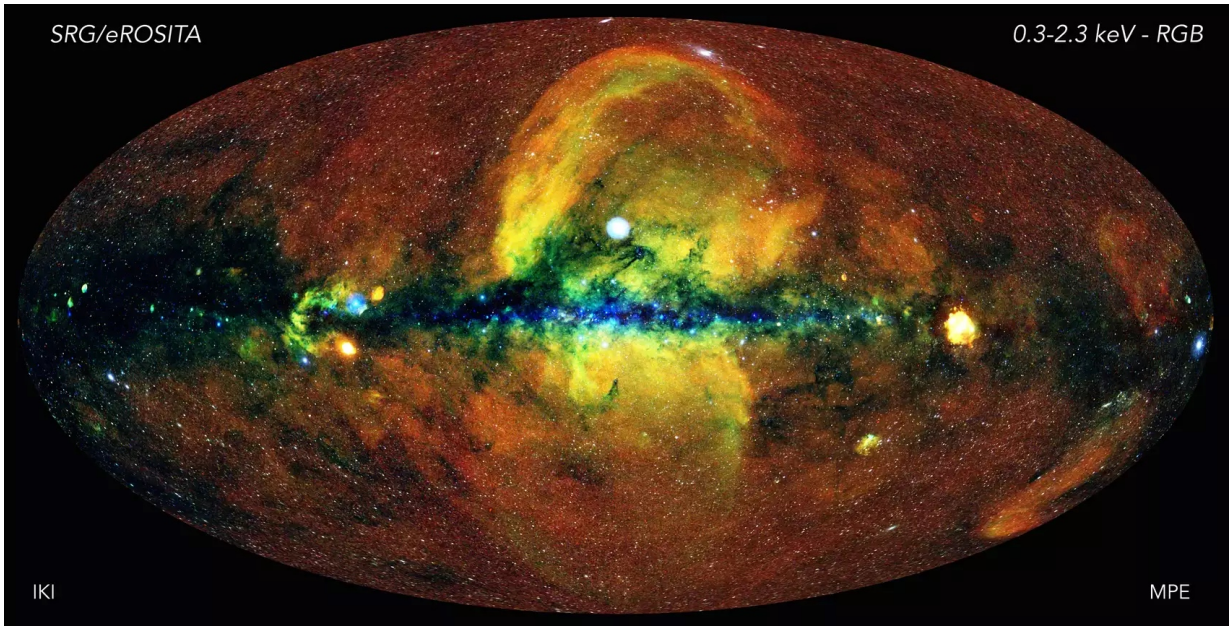

Figure 3.7.: All-sky map of the eRASS1 survey (Credit: Jeremy Sanders, Hermann Brunner and the eSASS team (MPE); Eugene Churazov, Marat Gilfanov (on behalf of IKI), taken from Max Planck Institute for Extraterrestrial Physics (2020))

compact objects, such as X-ray binaries and active stars, and diffuse emission, such as supernova remnants (SNRs). The investigation of this incredibly broad spectrum of X-ray phenomena and objects is another science goal of eROSITA. Many exciting science results have already been published and many more are pending in the future (Merloni et al., 2012).

eROSITA conducted four complete all-sky surveys before being put into safe mode in early 2022. The completed surveys are denoted eRASS1 to 4, generating a wealth of four different datasets to analyze, that will all be used in the present survey.

3.2. Expectations for the present research question

Considering the technical capabilities of eROSITA, that were discussed in the previous section, this section aims to clarify their impact on the present research question. Under which circumstances could a dark matter decay feature be detected and what further conclusions could be drawn from a possible detection?

The flux sensitivity of eROSITA in eRASS:1 (i.e. all observations up to and including eRASS1) has been measured for point sources only. It lies at $5 \cdot 10^{-14}\,\mathrm{erg\,s^{-1}\,cm^{-2}}$ for the soft band from $0.2-2.3\,\mathrm{keV}$ and at $7 \cdot 10^{-13}\,\mathrm{erg\,s^{-1}\,cm^{-2}}$ for the hard band from $2.3-8\,\mathrm{keV}$ (Predehl et al., 2021). Merloni et al. (2012) predicted the sensitivity for extended sources in the soft band to be lower by a factor of 2.5 than that of point sources.
While these numbers can serve as a reference point for the capabilities of eROSITA, concrete minimum flux estimates for dark matter decay lines are, however, not possible. Too many unknown factors exist in the detection of single decay lines, such as the influence of the particle background or astrophysical background components and the spectral model used to describe them. So while it can be safely assumed that the detection limits for the flux of point sources for eROSITA lie far below the limits applying in the present research question, no further conclusions can be drawn as to how far.

Critical in determining the appearance of possible dark matter decay lines in eROSITA data is first and foremost eROSITA's energy resolution. The energy resolution of all TMs was calibrated on ground using emission lines of different atomic decays. An image showing the results of this calibration for TM1 can be seen in Figure 3.8. It follows that a narrow, or even monochromatic, possible decay line would appear in the data at many times its actual width. The RMF (Redistribution Matrix File) files of the eROSITA spectra compensate for this effect automatically in the presentation of the data. eROSITA's energy resolution does, however, remain the deciding factor in determining errors on the energies of possible decay lines (Dennerl et al., 2020; Predehl et al., 2021).

Speckhard et al. (2016) describe how the origin of unidentified spectral lines in the Milky Way could be identified by investigating their shift for different Galactic longitudes. For what they denote as positive Galactic longitudes dark matter decay lines would appear slightly blueshifted, while lines caused by regular astrophysical gas would appear redshifted. Instrumental lines would experience no shift. This idea is further illustrated in Figure 3.9. To be able to measure this effect, however, a very high spectral resolution would be needed; Speckhard et al. (2016) cite an "0.1% scale". While this resolution could have been reached with Hitomi and could be reached in future missions, such as XRISM, the energy resolution of eROSITA is unfortunately around one order of magnitude too large for this feat. A further investigation of the shift of possible line detections will thus have to be left to future missions (XRISM Science Team, 2020).

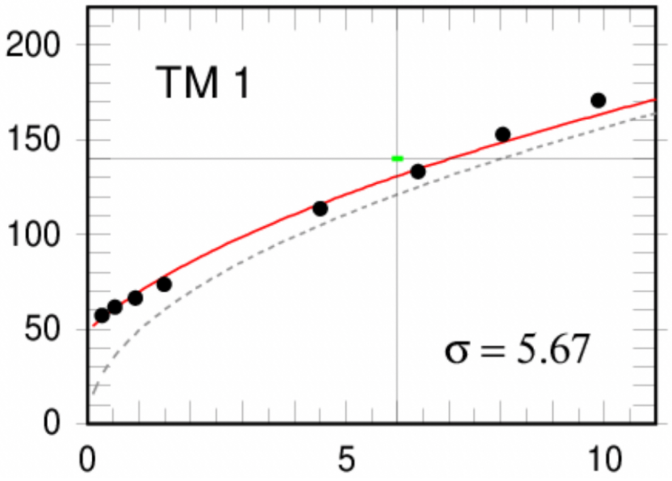

Figure 3.8.: Full width at half maximum (FWHM) of eROSITA calibration measurements of TM1 (vertical axis in eV) for different energies (horizontal axis in keV) with fitted function (taken from Dennerl et al. (2020))

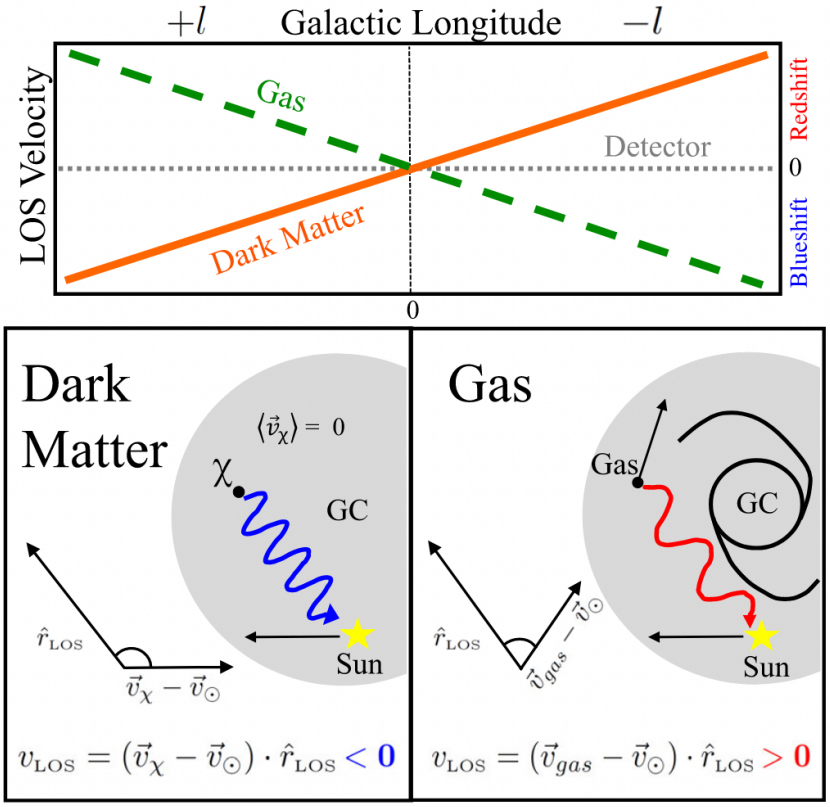

Figure 3.9.: Schematic describing the different behavior of spectral lines in respect to their red- and blueshift for different Galactic longitudes (taken from Speckhard et al. (2016))

4. Data analysis and spectral modeling

In this part of the thesis the process of the data analysis and spectral modeling that was carried out in this work will be described and the results of the analysis will be presented.

For the processing of data and the extraction of spectra the data analysis package eSASS (Brunner et al., 2018) was used on the sciserver of the MPE Garching (https://sciserver.mpe.mpg.de/). For the spectral analysis and fitting PyXspec (https://heasarc.gsfc.nasa.gov/xanadu/xspec/python/html/index.html), the Python interface of the XSPEC fitting program, was used (Gordon and Arnaud, 2022). For specific tasks NASA HEASoft (https://heasarc.gsfc.nasa.gov/docs/software/lheasoft/) commands were also used. For visualization of the data and the determination of regions and creation of region files the SAOImageDS9 (https://sites.google.com/cfa.harvard.edu/saoimageds9) software was used (Joye and Mandel, 2003). This research has also used Python and several of its packages, such as Numpy, Scipy, Matplotlib, and Astropy (Harris et al., 2020; Virtanen et al., 2020; Hunter, 2007; Astropy Collaboration et al., 2022).
The Python eSASS Analysis scripts by Dr. Jonathan Knies were used in many steps of the data processing, as was a PyXspec template of his implementation of the spectral model by Ponti et al. (2022).

4.1. Region selection and data reprocessing

For analysis in this project a semicircular region with a radius of $\sim 30°$ west of the Galactic center was chosen to include both parts of the Galactic bulge and halo. An exposure-corrected RGB image of the region in eRASS1 data can be seen in Figure 4.1. A sketch of the position of this region in the all-sky map can be seen in Figure 4.2.

The relevant eROSITA sky tiles to the region were determined through the eSASS Analysis script `skytiles_selector_gal.py`. The sky tiles containing and directly adjoining Sco-X1 (243108, 242105, 246108) were excluded from the analysis due to the extreme brightness of the source that would contaminate the data. The complete list of sky tiles used can be found in the Appendix in Section A.1. Only sky tiles on the "German" half of the sky were used; the strip of shared sky tiles around the Galactic longitude of zero was not analyzed.

The eSASS[1] command `evtool` was used to merge the 020 processing version eventfiles of

[1]More information on the eSASS specific commands can be found in the eSASS task descriptions that are publically available under https://erosita.mpe.mpg.de/edr/DataAnalysis/esasstasks.html.

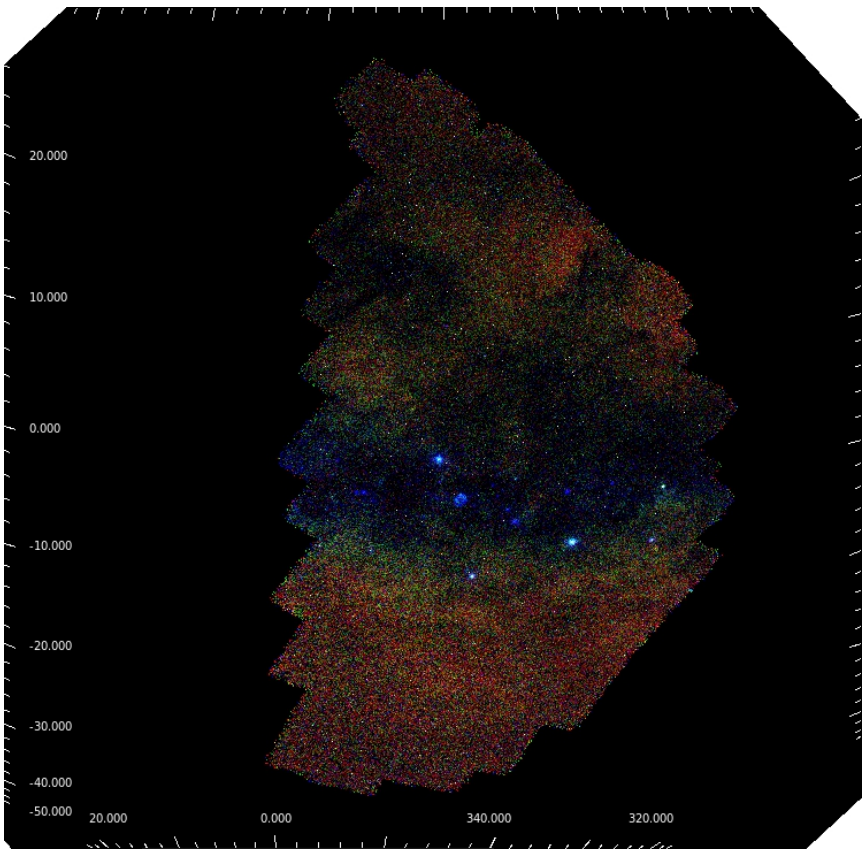

Figure 4.1.: RGB eRASS1 image of the selected region, axes in Galactic coordinates

the individual sky tiles, which are available through the sciserver of the MPE Garching, into one large file and to produce a broadband image for each eRASS from eRASS1 to 4. In order to be able to display the whole, rather large, region in one image a `rebin` factor of 320 was chosen. The events were filtered against contaminations using the `gti` filter FLAREGTI and the `pattern` 15.

Additionally the eSASS Analysis script `create_mosaic_evtool.py` was used to create exposure corrected mosaic RGB images of the eventfiles in three bands; their energy ranges can be found in Table 4.1. One of the resulting RGB images can be seen in Figure 4.1. It is immediately apparent that there is both emission from point sources and diffuse emission present in this region. Some extinction of the softer X-ray emission in the red and green energy bands through the Galactic disk can also be seen.

Afterwards exposure maps for the broadband images were created using the eSASS command `expmap`. In this step, too, FLAREGTI was specified as the `gti` filter. The optional keyword `withdetmaps` was also set to "yes" to ensure an accurate result containing no out-of-view pixels.

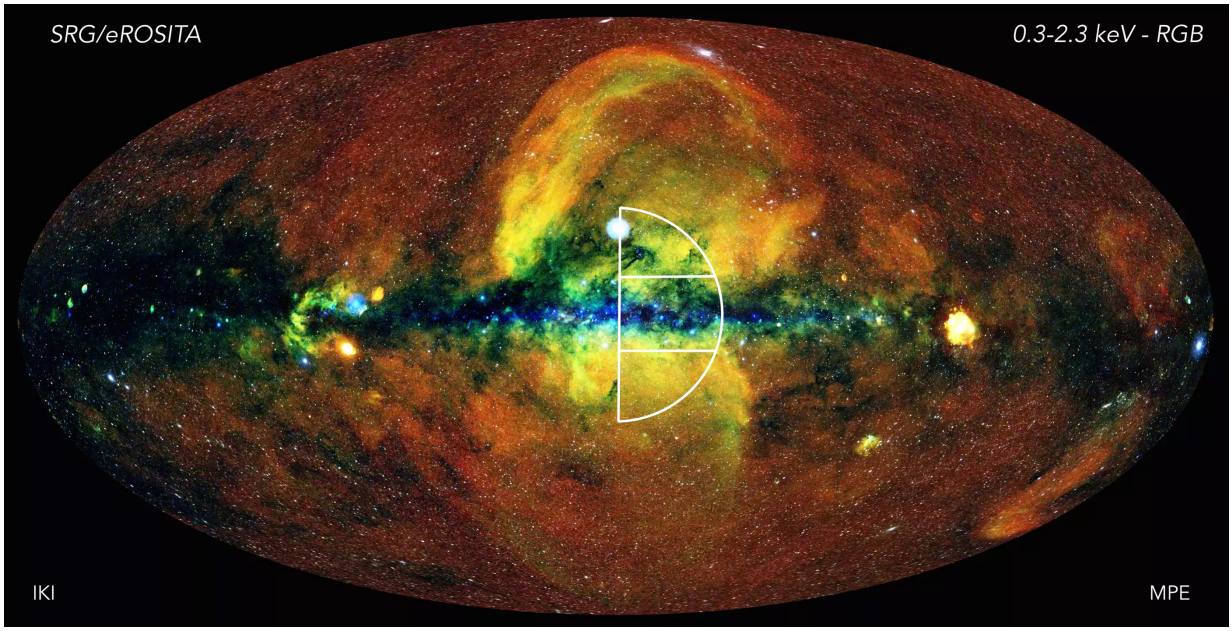

Figure 4.2.: Sketch of the approximate position of the analysis region in the eRASS1 all-sky map, Credit for the all-sky map: Jeremy Sanders, Hermann Brunner and the eSASS team (MPE); Eugene Churazov, Marat Gilfanov (on behalf of IKI) (taken and modified from Max Planck Institute for Extraterrestrial Physics (2020))

color	energy range [keV]
red	$0.2 - 0.7$
green	$0.7 - 1.0$
blue	$1.0 - 2.3$

Table 4.1.: Energy ranges of the RGB colors in Figure 4.1

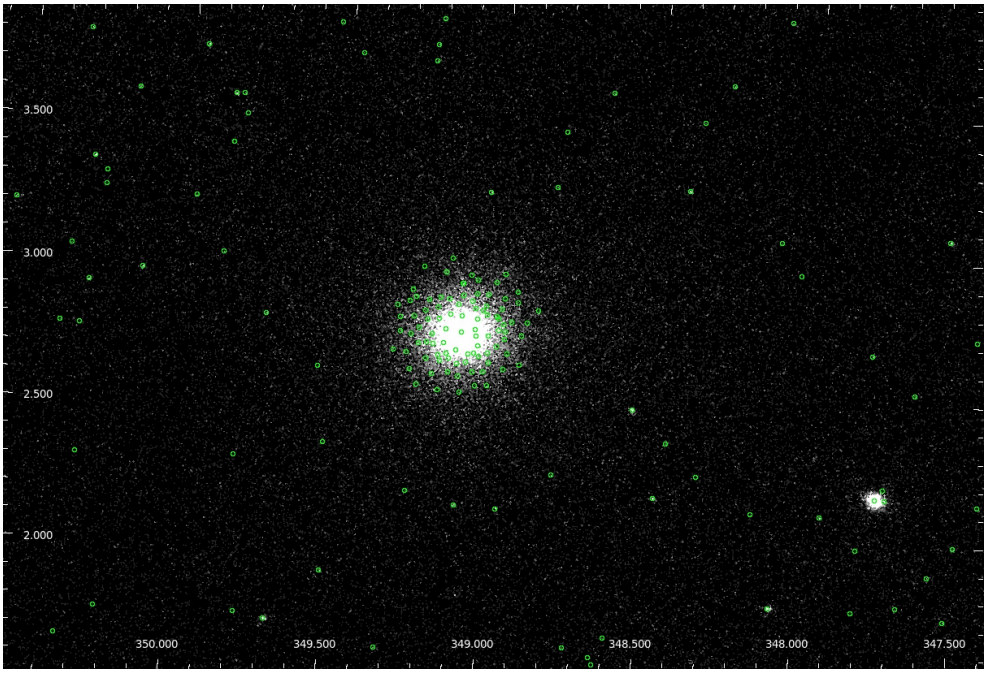

Figure 4.3.: Bright point source in the disk region that was not properly excluded through the script, excluded regions in green, axes in Galactic coordinates

4.2. Point source exclusion and extraction of spectra

The endeavor of this project was to study the diffuse X-ray background emission without the point sources littering the X-ray sky. Thus the numerous point sources present in the region of interest had to be excluded before spectra could be extracted to ensure that their contamination would be as small as possible.

To this purpose the eSASS Analysis script `create_region_mask.py` was used to create masks on the basis of the exposure maps. This ensured that the pixels on the edges of the sky tiles that could be improperly recorded by the cameras and possess large errors would not contaminate the data. By calling on the second eSASS Analysis script `select_regions.py` point sources could be automatically excluded on the basis of the eROSITA three band catalog.

It was discovered, however, that the standard region size of a circle with a radius of 0.46668 arcmin allotted to each source from the three band catalog was not sufficient for larger and brighter objects. Especially some of the brighter sources that can be seen in the Galactic disk in Figure 4.1 and Figure 4.2 were not sufficiently removed, as can be seen in Figure 4.3 and instead registered as many small point sources.

Due to this issue the broadband image of eRASS1 was scanned for bright sources by eye.

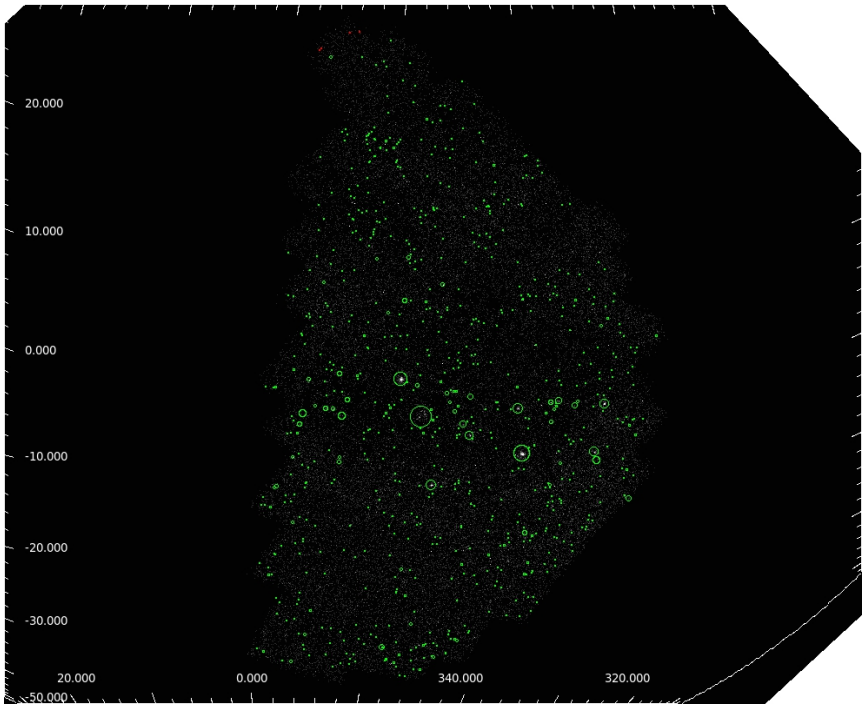

Figure 4.4.: Manually selected point source regions on the eRASS1 broadband image

This way the bright and extended sources in the broadband image could be found by eye and larger circular regions were defined to filter them out completely. The resulting additional regions can be seen in Figure 4.4. The region file could be passed to the `create_region_mask.py` script, which successfully excluded them in the masks.

After some tests with spectra extracted over the whole region of interest it was finally decided to split the region into three parts: a northern part, a disk part from -10 to $+10°$ Galactic latitude, and a southern part. The reasoning behind this is that the physical and chemical makeup and structure of the background emission is especially expected to vary when transitioning from the disk, that experiences a lot of extinction, to the northern and southern bulge and halo. These variations could "smear" the components of the spectra and lead to trouble with fitting and large residuals. To a smaller degree this effect might of course still be present in the three smaller - but still rather large - regions. It was also suggested[2] that the current energy calibration in the 020 processing version might not be sufficient for regions as large as these. Thus it might still cause residuals in the spectral fits for the smaller regions. To counteract this effect a variable energy offset was included in later spectral fits.

Three separate masks were created for each eRASS by passing additional polygon regions to `create_region_mask.py` to exclude all but the desired region. The lines between the disk,

[2]Private communication: Dr. Konrad Dennerl and other members of the Hot Milk meeting.

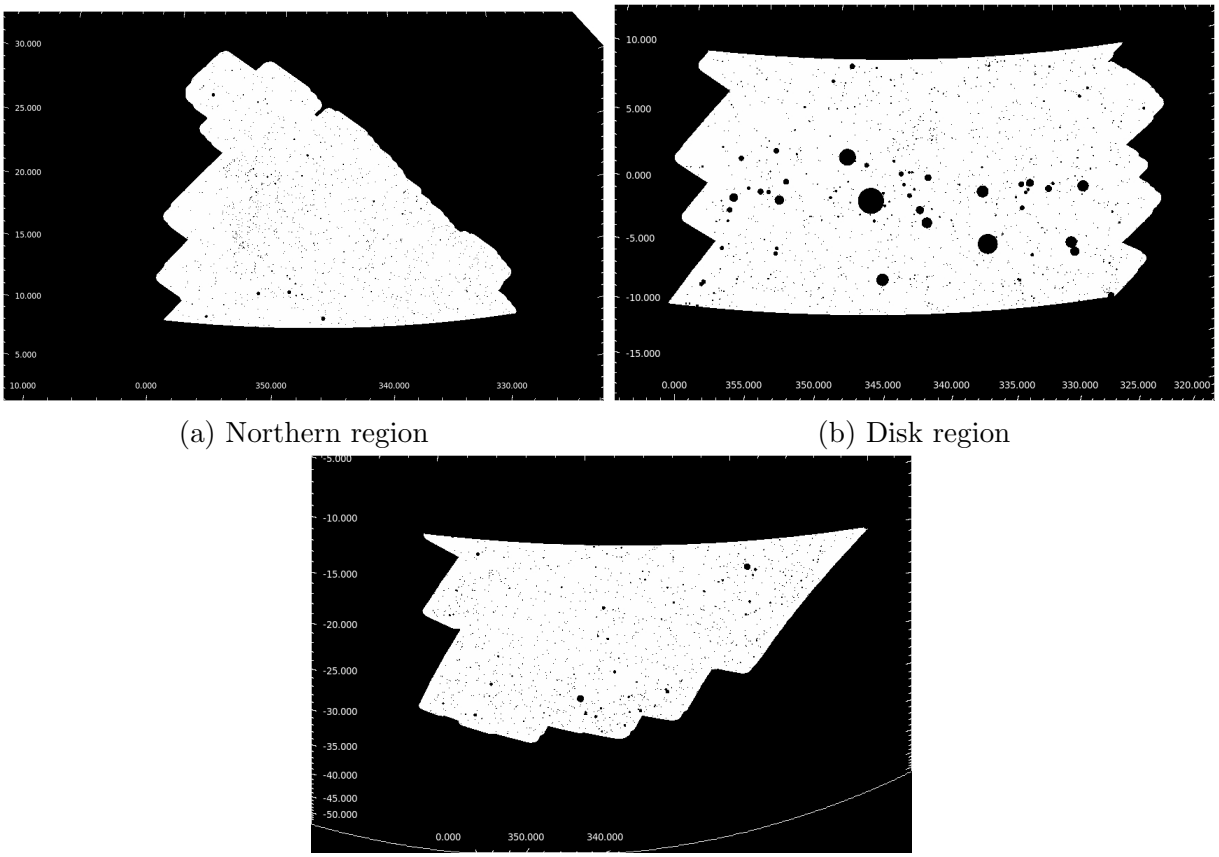

(a) Northern region

(b) Disk region

(c) Southern region

Figure 4.5.: Masks used for point source exclusion for eRASS1

north, and south regions were drawn using points at $+/-10°$ Galactic latitude in increments of 2.5° Galactic longitude in the polygon region. This way separate masks could be created for each eRASS and region. The three masks for eRASS1 can be seen in Figure 4.5.

Another function of `create_region_mask.py` is the determination of the area of the region, a parameter that is integral for the later normalization of the spectral fits. While this parameter is also provided by the `srctool` command during the extraction of spectra, the determination of the values by `create_region_mask.py` at this step was convenient and the thus determined values were used in the following steps. Due to the creation of the masks from the exposure maps the determined areas varied slightly through the different eRASSs for each region. While these small deviations are not expected to have a large impact on the results due to the large sizes of the regions as a whole, the individual area results were still used in the later spectral analyses to prevent unnecessary errors. A table containing the area of each region for each eRASS can be found in the Appendix in Section A.2.

Using these masks and the eventfiles, spectra could be extracted with the eSASS command `srctool`. The `exttype` option tophat was used due to the region being an extended area. As the corresponding `extpar` the approximate radius of the semicircular region was given. A slightly overestimated value of 35° was used here to make sure no data was accidentally excluded, as the outer edge of the sky tiles is not smooth. After tests with `xgrid` values of 20 and 50, that resulted in very high computation times, an `xgrid` value of 100 was chosen. As `xgrid` governs the positional accuracy, it is also assumed that its value does not have a too large impact on very large regions.

`srctool` provides source spectra of all TMs as an output, as well as a merged spectrum of all TMs, one containing only TM1, 2, 3, 4, and 6, and one consisting only of TM5 and 7. For each spectrum an RMF, ARF, and Background Spectrum is also provided. For this analysis only the separate spectra of TM1, 2, 3, 4, and 6 and their respective RMF and ARF files were used. Background spectra were unnecessary, as the object of interest in this case was the background itself.

Before the spectral analysis the spectra were regrouped, i.e. rebinned. This was accomplished using the HEASoft `grppha` bash command. The spectra were rebinned to a grpmin of 50. The bin size was thus automatically chosen in such a way that each bin had a count of at least 50 events. In the same step the keywords RESPFILE and ANCRFILE of the regrouped spectra were set to the corresponding RMF and ARF filenames respectively. This ensured that the right RMF and ARF files would automatically be used with the regrouped spectra in the analysis. The keyword BACKFILE was set to “none”, as no background spectrum was subtracted in this analysis. The spectra were now ready for analysis.

4.3. Spectral fitting

In this section the process and steps of the spectral fitting will be described roughly chronologically, starting with the initial model. The section covers many considerations made for the fits, as well as a selection of experimental fits, before describing the final fits that were used in the following steps of the project.

4.3.1. Starting model and initial considerations

For spectral fitting the background model developed by Ponti et al. (2022) was used to fit the different components of the diffuse X-ray background, that were described in Section 2.3. It was used in a modified version by Dr. Jonathan Knies, in which the nH absorption was initially modeled with a TBabs model component instead of the disnht model by Locatelli et al. (2022) used by Ponti et al. (2022). The CXB, meanwhile, was modeled through a simple powerlaw instead of the double broken powerlaw used by Ponti et al. (2022) and normalizations of the model were effectively divided by the area of of the region in arcmin^2.

Due to the large region sizes and comparably high statistics of the spectra chi2 statistics could be used. The chosen TMs 1, 2, 3, 4, and 6 were fitted together for each eRASS and region. For the element abundances in the model wilm abundances were used (Wilms et al., 2000), abundances are given in Solar units. For an overview over the spectral model components used in this work, see Table 4.2.

The SWCX (Solar wind charge exchange) is modeled using an unabsorbed acx2 model (Ponti et al., 2022; Smith et al., 2012; Foster et al., 2020; Foster, 2023). Its temperature was first frozen to 0.1 keV. In later steps more accurate values for this parameter were investigated; more details on how this was realized can be found in Section 4.3.5. The collision parameter, i.e. the collision velocity, was set to 450 km/s and is assumed to be the center of mass velocity (collntype 2). acx model number 8 was used with single recombination, a Hefrac of 0.09, and an abund value of 1. More information on these model parameters and their meaning can be found in Foster (2023). The values and options of these parameters were part of the existing model and correspond mostly to the ones used by Ponti et al. (2022). The only parameter, apart from the normalization, that was changed and investigated in the scope of this thesis was the temperature of the model.

The LHB (local hot bubble) is modeled with an unabsorbed apec component with Solar abundances and a temperature constrained between 0.09 and 0.12 keV. In later steps this value was modified to comply with the local literature values of Liu et al. (2017) as was the norm of the LHB. Details on this can be found in Section 4.3.6. As both the LHB and the SWCX components are Galactic and originate in the nearer vicinity of our point of observation, Galactic absorption is assumed to be negligible. They are thus exempt from the absorption model.

component name	component description
apec	collisionally ionized diffuse gas model (Smith et al., 2001)
vapec	collisionally ionized diffuse gas model with fine-tunable element abundances (Smith et al., 2001)
vnei	non-equilibrium collisional plasma model with constant temperature and with fine-tunable element abundances (Borkowski et al., 2001)
vrnei	non-equilibrium recombining collisional plasma model with fine-tunable element abundances
powerlaw	powerlaw photon spectrum
acx2	model for CX between ions and donor ions/atoms (Foster, 2023)
TBabs	Tuebingen-Boulder ISM absorption model (Wilms et al., 2000)
disnht	ISM absorption model for distributed column densities (Locatelli et al., 2022)

Table 4.2.: Overview over additive (first table section) and multiplicative (second table section) spectral modeling components used in this work, further details on the models and their parameters can be found in Arnaud et al. (2023); Foster (2023); Locatelli et al. (2022); Wilms et al. (2000)

To model the nH absorption, which the other spectral components experience, a TBabs model is applied to the rest of the components. The approximate average nH values were determined for each region; this process is further described in Section 4.3.2.

The CGM (circumgalactic medium) is modeled with an absorbed apec. Its temperature is left free to vary between 0.15 and 0.25 keV. Its abundance, meanwhile, is frozen to a value of 0.08 in the basic model. This was changed in later steps of the analysis.

The Hot Corona (Cor) is modeled using an absorbed apec as well. This apec possesses a temperature that has been frozen to 0.7 keV and an abundance that has been frozen to 1.0. These parameters, too, were changed in the later analysis process.

Finally extragalactic emission, the cosmic X-ray background (CXB), is modeled with an absorbed powerlaw with a photon index of 1.46.

An example spectrum illustrating the model and its components can be seen in Figure 4.6. The components result in the following basic model of the diffuse X-ray background (Ponti et al., 2022):

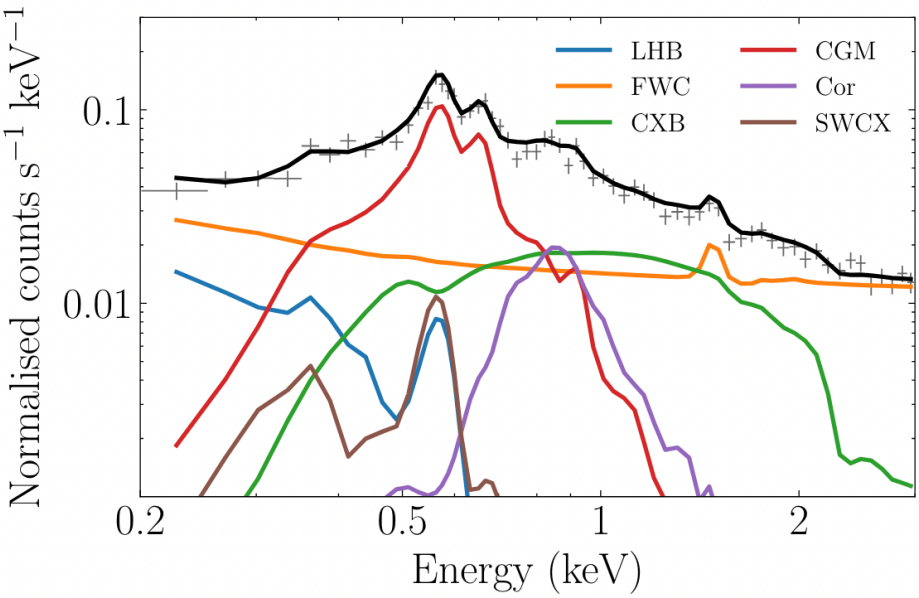

Figure 4.6.: Example spectrum illustrating the spectral components of the model (taken from Yeung et al. (2023))

$$\text{acx2} + \text{apec} + \text{TBabs} * (\text{apec} + \text{apec} + \text{powerlaw}) \tag{4.3.1}$$

A constant was added to each fit containing the area of the region in question in arcmin^2, in order to equalize the norms of the fit components. A second constant governs the normalization of the different TMs against one another, as TM1, 2, 3, 4, and 6 are fit simultaneously. The resulting model is thus:

$$\text{const} * \text{const} * (\text{acx2} + \text{apec} + \text{TBabs} * (\text{apec} + \text{apec} + \text{powerlaw})) \tag{4.3.2}$$

To model the instrumental and particle background of eROSITA the FWC (filter wheel closed) model for each TM is used. It was refitted to the calibration data by Dr. Jonathan Knies but corresponds very closely to the original version[3] modeled by Michael Yeung. The instrumental and particle background can be only modeled, not subtracted, with this model. Thus the FWC models of TM1, 2, 3, 4, and 6 were added as additional models to the fit. All parameters in the model are frozen, except for the normalization constants, which scale the whole FWC models to the rest of the model.

While the energy range of $0.2 - 10\,\text{keV}$ of eROSITA is usually seen as reliable and usable for fitting, it was decided to constrain the energy range to $0.2 - 9.0\,\text{keV}$ for this analysis. The reason for that can be seen in Figure 4.7, which shows the eRASS1 spectrum of the northern region. It can be clearly seen that the tail end of the spectrum between 9 and

[3]Available internally for the eROSITA collaboration under https://wiki.mpe.mpg.de/eRosita/FWC_020.

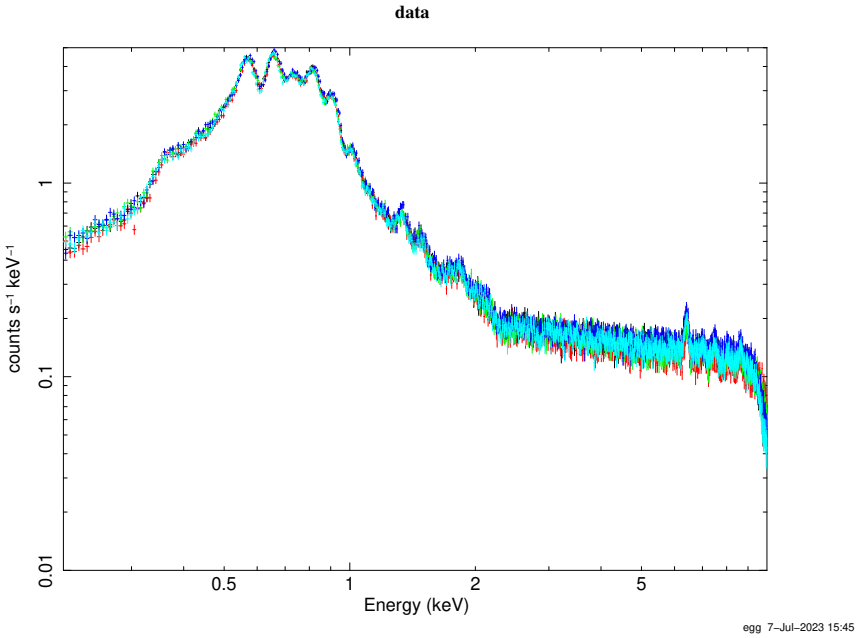

Figure 4.7.: eRASS1 spectrum of the northern region over $0.2 - 10\,\mathrm{keV}$

10 keV experiences a sharp drop, which might be connected to a decline in effective area in these energies. Due to the fact that this drop is not physical and would produce tension with the model used it was decided to exclude this energy range from the analysis.

4.3.2. Determining nH-values for the regions

To correctly model the nH absorption in the CGM, Hot Corona, and CXB, nH values for the analyzed regions had to be found. The nH values for the TBabs component for each region were determined through the HEASoft `nh` command.

Due to the very large sizes of the regions, however, the following approach was taken: One or two circular regions were placed in each region. They can be seen in Figure 4.8. For each circular region the average nH value was then calculated using the HEASoft `nh` command. In the case of two circular regions, the weighted average nH was then calculated through the following equation, where $\mathrm{nH}_{1/2}$ and $A_{1/2}$ refer to the average nH value and area of the respective circular region:

$$\mathrm{nH} = \frac{\mathrm{nH}_1 \cdot A_1 + \mathrm{nH}_2 \cdot A_2}{A_1 + A_2} \tag{4.3.3}$$

The obtained nH values and the circular regions can be found in Table 4.3.

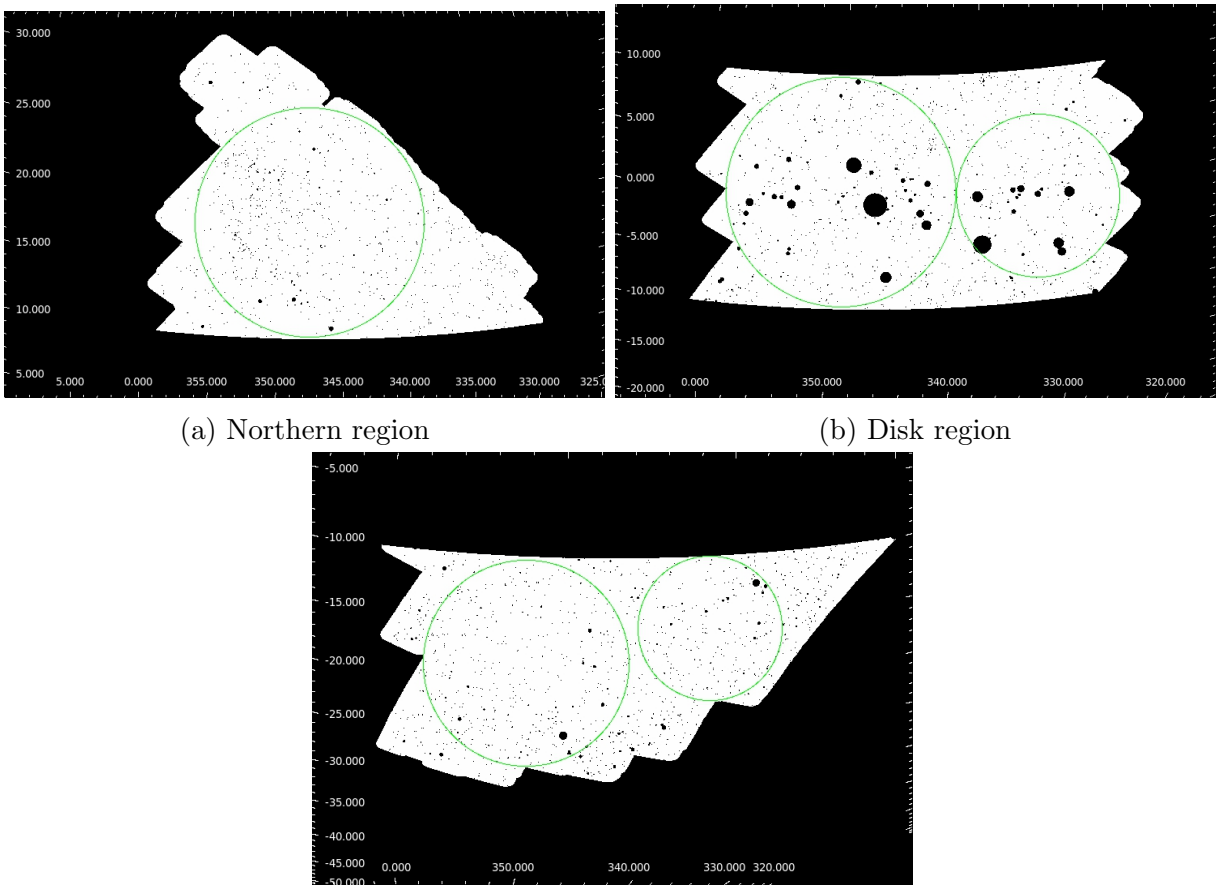

(a) Northern region

(b) Disk region

(c) Southern region

Figure 4.8.: Circular regions for nH value determination (background: masks used for point source exclusion for eRASS1)

region	circular region(s) (RA [deg], DEC [deg], radius [deg])	average nH value $[10^{22}\,\mathrm{cm}^{-2}]$
north	$(241.472, -26.684, 8.950)$	0.113
disk	$(259.350, -37.145, 9.151)$	0.821
	$(247.207, -49.398, 6.481)$	
south	$(282.681, -44.798, 6.489)$	0.0644
	$(272.568, -53.621, 4.548)$	

Table 4.3.: Average nH values for the three regions as well as the circular region(s) used to obtain them

4.3.3. First fits and single tile spectrum

At first it was attempted to fit the basic model (Eq. 4.3.2) to the X-ray spectra. In an attempt to mitigate residuals the absorption model TBabs was "split" between the CGM component and the Hot Corona and CXB component, i.e. both parts received their own TBabs components. Meanwhile, their nH values were freed to vary up to maxima corresponding to the nH values that were found in Section 4.3.2. The idea behind this was the fact that it is entirely possible for light to pass through less than the approximated amount of nH, should it - for example - originate a little closer to our point of observation. The model thus amounted to:

$$\text{const} * \text{const} * (\text{acx2} + \text{apec} + \text{TBabs} * (\text{apec}) + \text{TBabs} * (\text{apec} + \text{powerlaw})) \quad (4.3.4)$$

In many cases the nH-values would barely change during the fit. As the additional degree of freedom was later discovered to occasionally not agree well with more complicated models and seemed physically uncertain, the "split absorption" was reversed for the very final fits from Section 4.3.7 onward.

The basic fit to the eRASS1 data of the northern region can be seen in Figure 4.9 with a reduced χ^2 of 2.46. It can be seen that large residuals remain and the basic model is not a good fit to the data. Due to this many different modifications of the model were explored to find a version which describes the data well and can be used in the next step of the analysis.

The question whether these large residuals are caused by the large region size was explored by extracting the eRASS1 spectrum of a single sky tile (267132, center point at RA= 267.0329670°, DEC= −42.0082895°) and trying to fit it with the basic background model (with the additional TBabs component). The result can be seen in Figure 4.10. It becomes clear that, while residuals are also present in this fit, they are on a much smaller scale, resulting in a reduced χ^2 of 1.22 without any additional components or changes. Thus the conclusion can be drawn that the large size of the region has a significant impact on the quality of the fit.

It is possible that errors and uncertainties in the calibration are added up and thus amplified on these scales and contribute to the residuals. At the same time the higher statistics result in smaller statistical errors for the datapoints, causing quantitative divergences between model and data to result in higher residuals, which makes the fits less forgiving. Another potential factor in the explanation would be the aforementioned effect of parameters, e.g. the temperature, of the different background components changing over the large area. All of these factors, as well as the aforementioned potentially insufficient energy calibration could contribute to the observed level of residuals. It was not possible within the scope of this work to explore the extent of these effects further. To counteract issues in the energy calibration, however, a variable energy offset was added to many fits in the form of a gain offset.

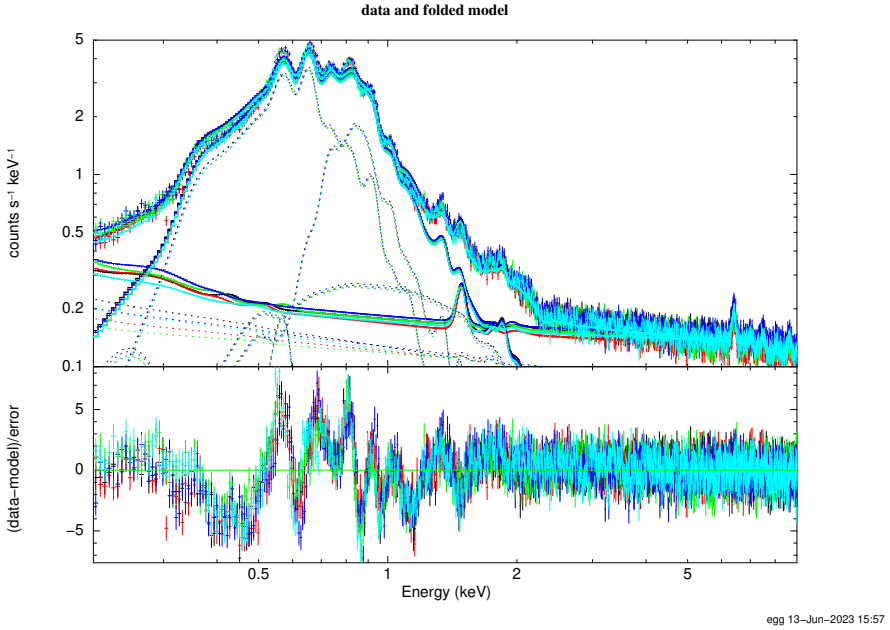

Figure 4.9.: Basic fit to the eRASS1 spectrum of the northern region, reduced χ^2 of 2.46

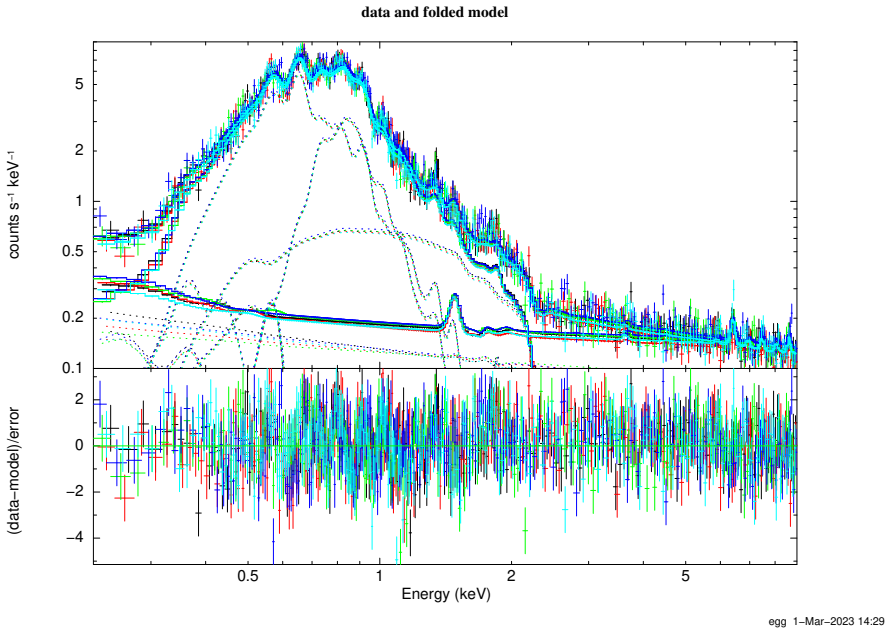

Figure 4.10.: Basic fit on the single sky tile 267132, reduced χ^2 of 1.22

The fitting process then was conducted applying the following strategy: first the eRASS1 data in the northern region was used to test a large variety of models. Afterwards the most promising of these were used to fit the northern region for all eRASS and further perfected to agree with the literature. Then the fits were adapted and used to fit the southern and disk region.

The following sections give an overview over the process and progress in the fitting in the course of the work on this project. Not all fits that were conducted were perfected and some contain assumptions that were later overthrown. For the purpose and scope of this thesis and the project it was not possible to perfect all of the intermediate steps. Then again, the final fits are of course improved as far as was possible to be used in the next step of the analysis.

4.3.4. Tests with northern eRASS1

As the first step in the spectral fitting process, tests with the eRASS1 data of the northern region were conducted to see which modifications to the basic model had good potential. This section gives an overview over this process.

Generally the strategies attempted in these tests can be divided into three successive stages: first, the simple addition of model components to the basic model. Second, the loosening of the parameter bounds present in the model in accordance with Ponti et al. (2022) in combination with additional parameters. Third the description of the CGM component through a vapec model, in addition to loosened parameters and additional model components.

Finally it was discovered that improvements could also be achieved by using F-tests to decide whether the unfreezing of individual abundance parameters in vapec/vnei components was justified and by putting constraints on their absolute values.

Adding components

As a first strategy different additional spectral components were added to the model. In this vein an energy offset was also included in the fit in the form of a gain offset.

As can be seen in Table 4.4 an additional apec component improved the reduced χ^2 of the fit by > 0.9, which is substantial.
The addition of a gain offset also improved the fit significantly, if less so than the apec component. A gain offset parameter allows the energy scale of each individual TM to vary by an offset.
It can be seen in Table 4.4 that the effect of the gain offset is especially large when combined with other additional components. Combining an additional apec component with a

description of fit	#dof	reduced χ^2
no additional components	4197	2.46
added apec	4194	1.54
added gain offset	4192	2.22
added apec and gain offset	4189	1.35
added apec, gain offset, and vnei	4189	1.31

Table 4.4.: Notable steps in modeling with (only) additional components, their reduced χ^2 values, and the numbers of their degrees of freedom (#dof)

gain offset leads to a very significant improvement of ~ 1.11 on the reduced χ^2 as compared to the basic fit. This fit can be seen in Figure 4.11. It can be seen that the additional apec component is located at similaly low energies to the CGM component around $\sim 0.25\,\mathrm{keV}$. The abundance of this additional apec component, however, stayed at 1.0, even when left free to vary. A number of remaining residual peaks can also be seen in Figure 4.11. Here one of the weaknesses of the model can already be very clearly seen: the additional apec component seems to mainly double the CGM component while possessing a higher elemental abundance. This might point to the conclusion that the additional apec model is unnecessary, but that the elemental abundance of the CGM component is actually higher than expected - an assumption that seemed very likely in the further course of fitting.

In an attempt to further improve this fit other components were added to the model. Of these an additional vnei component proved to be the most suitable as can be seen in Table 4.4 and Figure 4.12. Its O, Ne, Mg, Si, S, and Fe abundances were individually fitted. It becomes apparent that especially the peaks in the residuals around $1 - 2\,\mathrm{keV}$ reduce in size with the addition of a vnei component. While this fit was one of the best fits (reduced χ^2-wise) during the fitting process, the doubled apecs at lower energies, as mentioned, do point to other possibilities in terms of the makeup of the fit, which were explored in the next steps.

Loosening the parameter bounds on the CGM and Hot Corona

While the basic model used in this fitting process allowed the temperature of the CGM to vary from $0.15 - 0.25\,\mathrm{keV}$ in good agreement with Ponti et al. (2022), its abundance was initially frozen to 0.08. This value was now loosened, to within a range of $0.04 - 0.3$. While Ponti et al. (2022) report best fit abundances between 0.05 and 0.1, abundances below 0.05 do occur and abundances up to 0.3 are mentioned as a possibility.

At the same time the temperature of the Hot Corona component that had been frozen to

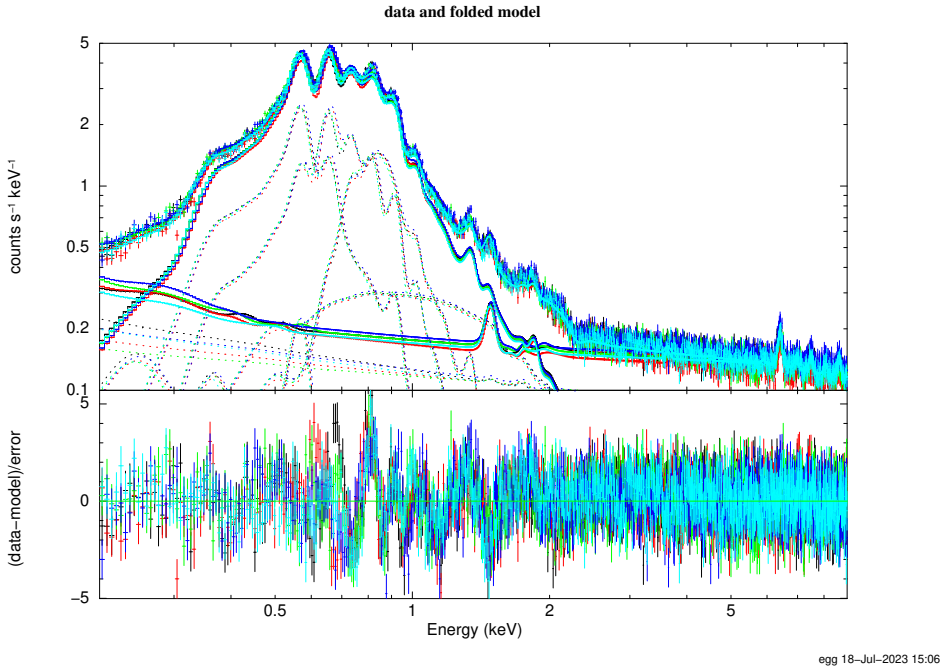

Figure 4.11.: Fit on the northern eRASS1 data with added apec and gain offset

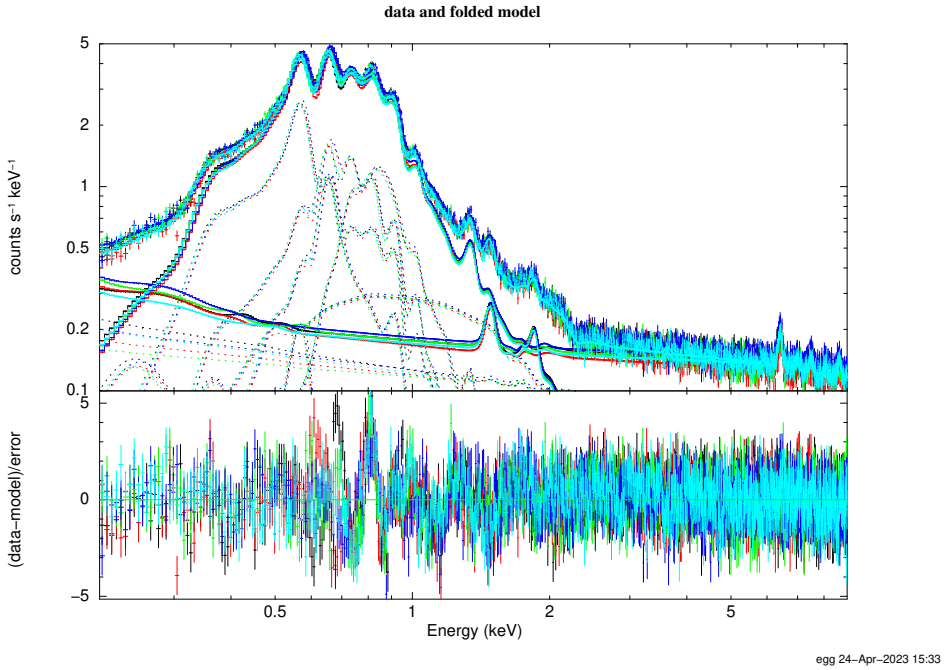

Figure 4.12.: Fit on the northern eRASS1 data with added apec, gain offset, and vnei

description of fit	#dof	reduced χ^2
no additional components	4196	1.66
added gain offset	4191	1.46
added apec	4193	1.59
added apec and gain offset	4188	1.41
added vnei	4186	1.51
added vnei and gain offset	4187	1.31
added vrnei	4185	1.53
added vrnei and gain offset	4186	1.32

Table 4.5.: Notable steps in modeling with loosened CGM and Hot Corona parameters, their reduced χ^2 values, and the numbers of their degrees of freedom (#dof)

0.7 keV was unfrozen within a range of $0.45 - 0.75$ keV, also in accordance with Ponti et al. (2022). It was also tested whether changing/unfreezing the abundance of the Hot Corona component would improve the fit, however, just as was seen by Ponti et al. (2022) the abundance of the Hot Corona component did not appear to have an effect on the quality of the fit.

It can be seen in Table 4.5 that the freeing of these parameters signified an immediate improvement in the fit. Even without additional components it reached a reduced χ^2 value of 1.66. A plot of this fit can be seen in Figure 4.13. When comparing it to Figure 4.9 it becomes immediately apparent that the residuals that were present below ~ 0.5 keV have been strongly reduced - this time without the addition of another apec.

Adding components to the fit further improved this value. It can, however, be seen that an additional apec only leads to a significantly smaller improvement when compared to the improvement seen in the previous section (a $\Delta\chi^2_{\text{red}}$ of 0.07 instead of 0.92). This gives further weight to the theory that the additional soft apec at this energy is only preferred for its higher abundance and does not represent a proper physical component in the emission.

Different components were again added to improve the fit further. As can be seen in Table 4.5 a vnei component once again proves to be a good addition to the model, as does a vrnei component. Both fits appeared to be good options that were further explored in later steps.

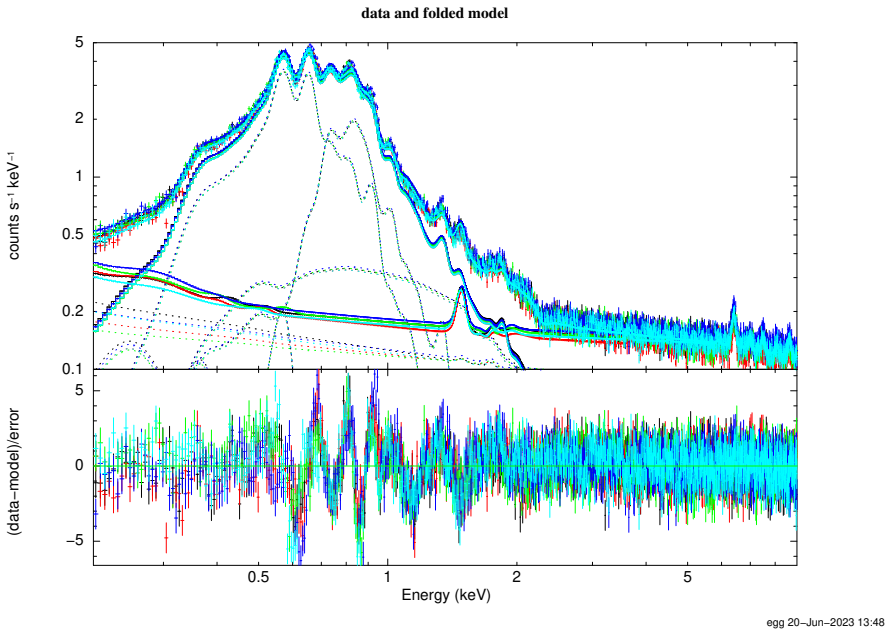

Figure 4.13.: Fit on the northern eRASS1 data with loosened CGM and Hot Corona parameters

Description of the CGM via vapec model

Another option was explored in the following step. While the Suzaku data analysis of Ueda et al. (2022) focused on a much smaller and softer energy range, their approach in modeling the CGM component with a vapec model was an intriguing possibility: could the fit be improved through a finer description of the elemental abundances of the CGM, that had already had such a large impact on the quality of the fit?

To test this the apec describing the CGM was replaced with a vapec component with an identical free temperature range. Its O, Ne, Mg, Si, S, and Fe abundances were fitted individually in the range of $0.04 - 0.3$ established in the previous section; the rest were frozen to 0.08.

As can be seen in Table 4.6 an immediate further improvement followed. Without any additional components the fit reached a reduced χ^2 of 1.57. This fit can be seen in Figure 4.14. With the addition of a gain offset the fit even reached a reduced χ^2 of 1.40. Further adding a vnei component slightly improved the reduced χ^2 of the fit to 1.32.

While this model was explored, however, a different issue reared its head: the abundance values of the vnei and vrnei components, as well as of the newly added vapec, would occasionally either rise to values far beyond a physical explanation, or converge to zero. Both

could massively distort the fit results. To mitigate this problem F-tests were introduced into the fitting process.

description of fit	#dof	reduced χ^2
no additional components	4190	1.57
added gain offset	4191	1.40
added vnei and gain offset	4181	1.32
added vrnei and gain offset	4180	1.34

Table 4.6.: Notable steps in modeling with a vapec CGM component, their reduced χ^2 values, and the numbers of their degrees of freedom (#dof)

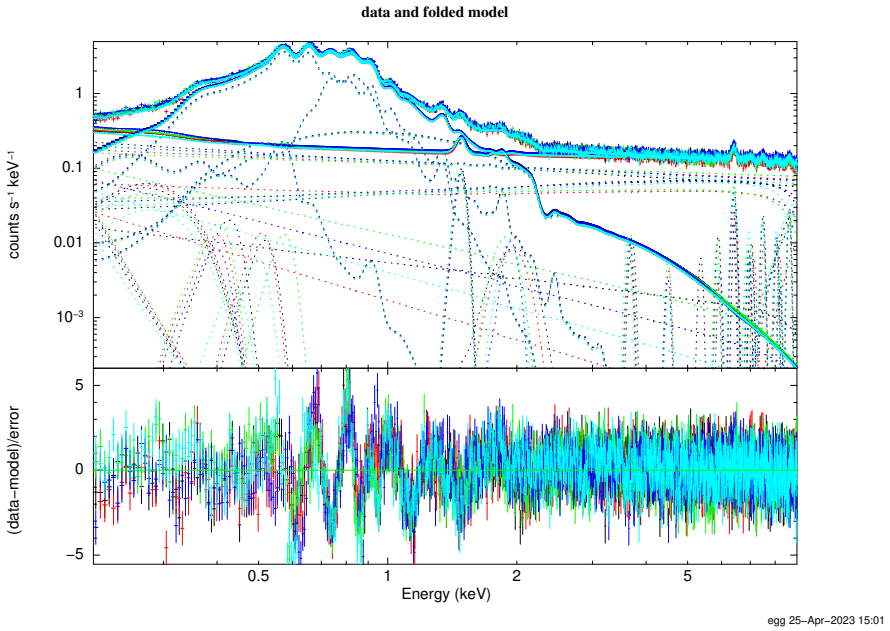

Figure 4.14.: Fit on the northern eRASS1 data with a vapec CGM component

Improvements with F-tests

An F-test is a statistical test that compares the variances of two different data sets (Wall and Jenkins, 2012). When adding new free parameters or components to an established fit, it can be used to determine whether the addition of these parameters is statistically justified.

The F-test is implemented in PyXspec through the `ftest` function. It takes four parameters: the χ^2 and number of degrees of freedom before the addition of the free parameter(s) and both after the addition of the free parameter(s). The output value of the function is then a value for the probability that the additional parameter(s) were unnecessary. It is, however, not valid to use the F-test to test for the presence of an additional Gaussian line in a fit; it can thus not be used for the later line detection in this analysis (Gordon and Arnaud, 2022).

In practice this was implemented for the additional vapec, vnei, and vrnei components as follows: each of the abundance parameters of O, Ne, Mg, Si, S, and Fe was initially frozen to 1.0. One by one each of the parameters was unfrozen and fitted. If the resulting value did not lie between 0.1 and 10, it was reset to 1.0 and refrozen. If it did, an F-test was conducted. Only if the output probability - the probability that the additional parameter was unnecessary - was below 0.27% (corresponding to a significance of 3σ), the new parameter value was accepted (Wall and Jenkins, 2012). The parameter was then refrozen to the new value, otherwise it was reset as described. After all parameters were fitted that way, all that had passed the F-test were once again freed and the model was fitted again to make sure that their values could be coordinated and adjusted against one another. Then they were finally refrozen; in the final steps of the fitting process from Section 4.3.7 onward they were left unfrozen instead.

The process applied to the CGM vapec component was largely identical. Instead of checking whether the fitted value lay in an acceptable margin, the abundances were, however, constrained to the established range of $0.04 - 0.3$. The starting and standard value for all abundances left frozen was once again 0.08.

This measure successfully counteracted the too high and too low abundance values that were impacting the fits. For some fits this lead to an increase in their reduced χ^2 values. This, however, was an acceptable price to pay for better control over the abundance parameters of the models and more physical fits.

4.3.5. Constraining the temperature of the SWCX and the analyzed energy range

As some of the models that had been tested on the northern eRASS1 data were fitted to the northern eRASS2, 3, and 4 data, an issue was discovered: in almost exclusively all of the fits the norm of the acx2 component describing the SWCX influx would quickly approach zero and remain there, effectively removing the component from the fit. While this might be realistic for eRASS1 and 2 data, the influence of SWCX was not expected to be negligible in eRASS3 and 4 (Ponti et al., 2022). While this could be, in part, counteracted by setting a lower limit of $1 \cdot 10^{-8}$ for the acx2 norm, its true temperature still remained unknown.

The temperature of the acx2 component had first been left at 0.1 keV. This now seemed to be, however, not an ideal solution and had to be improved upon. The temperature of the acx2 model can produce large differences in the shape of the model. Leaving it completely free to vary, however, can massively prolong the computation time, while the value of the parameter can easily leave the physical parameter space. The goal was thus now to constrain the temperature of the SWCX independently from the other background components instead of fitting it simultaneously.

For this purpose the same approach as the one utilized by Ponti et al. (2022) was taken: The eRASS1 spectrum was subtracted from the eRASS3 spectrum and the resulting difference was fitted with an acx2 model with cstat statistics. This was done under the assumption that the SWCX component is a lot weaker in eRASS1 than in eRASS3 if it is present at all, as this was observed before, e.g. by Ponti et al. (2022) and Yeung et al. (2023).

As it was observed that the spectra of TM4 deviated from those of the other TMs, as can be seen in Figure 4.15, they were excluded from the fits. The results of a fit without TM4 for the northern region can be seen in Figure 4.16.

Here it became apparent that the SWCX component was not the only thing remaining; a soft excess is visible at energies of $\sim 0.2 - 0.3$ keV. This excess is caused by a rise in the particle background from eRASS1 to eRASS3 and appeared to be the main cause of the SWCX being continuosly suppressed in favor of the LHB in the earlier fits. This effect is known; it can be traced in the FWC data of all TMs, such as TM2 in Figure 4.17. This resulted in lower energy limits being placed on the stability of the FWC model, 0.2 keV for TMs 1, 3, and 6 and 0.25 keV for TMs 2 and 4 (Yeung et al., 2023). While the FWC model is in principle expected to remain reliable above these limits, which are denoted for instance by the dashed line in Figure 4.17 for TM2, the excess in the data of the present analysis was very strong up to energies of 0.3 keV, as is evident in Figure 4.16.

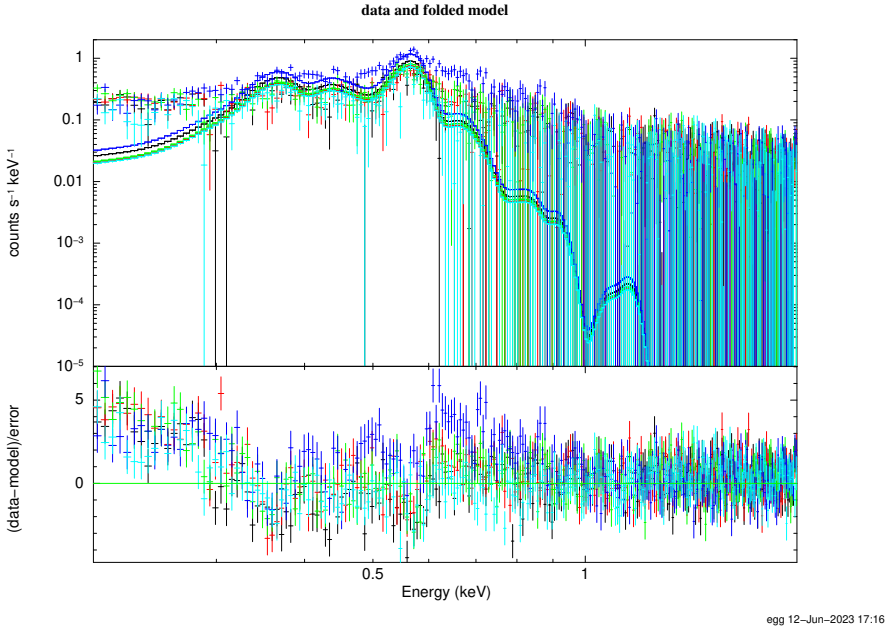

Figure 4.15.: SWCX fit for the northern region with TM4 (dark blue). TM4 was excluded for later SWCX fits.

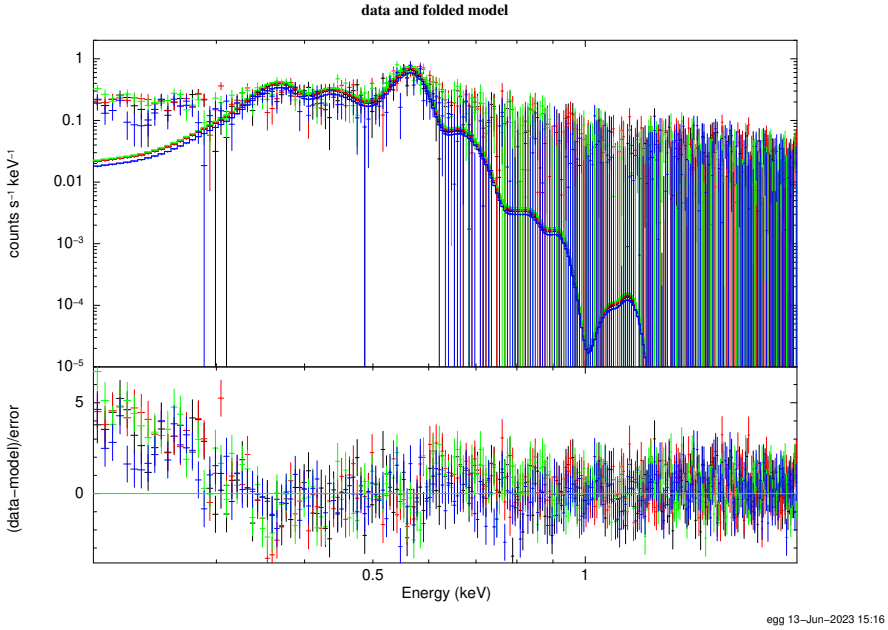

Figure 4.16.: Northern region SWCX fit over the energy range from $0.2 - 2.0\,\mathrm{keV}$, reduced $\chi^2 = 2.01$

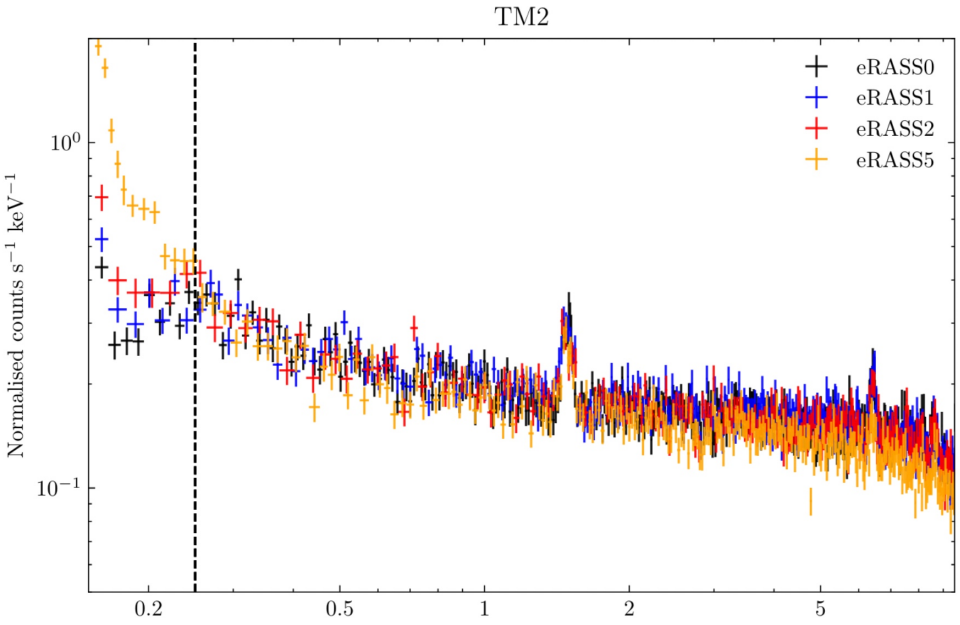

Figure 4.17.: Development of TM2 FWC data from eRASS1 to 5 (taken from Yeung et al. (2023))

In accordance with advice[4] from Michael Yeung, the creator of the FWC model, it was thus decided to exclude the energy range below 0.3 keV from the further analysis in order to avoid influence of this excess on the fit.

Consequently the SWCX fits were repeated in the energy range of $0.3-2.0$ keV. The results can be seen in Figure 4.18. While beginnings of the soft excess and a slight offset from zero can still be seen in Figure 4.18, especially in 4.18a and 4.18b, the fits are massively improved and give well constrained temperature values for the further analysis. Their values can be found in Table 4.7.

[4]Private communication: Michael Yeung.

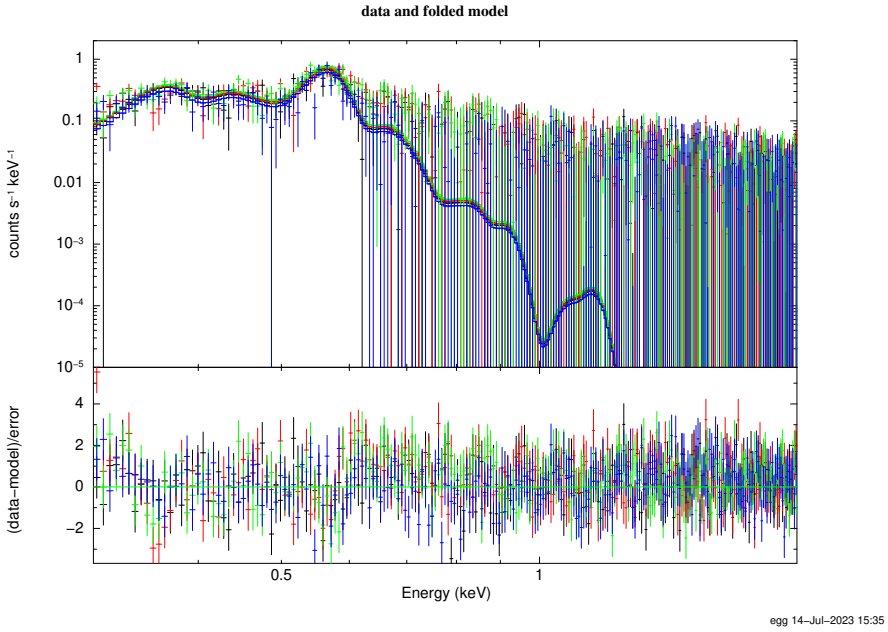

(a) Northern region

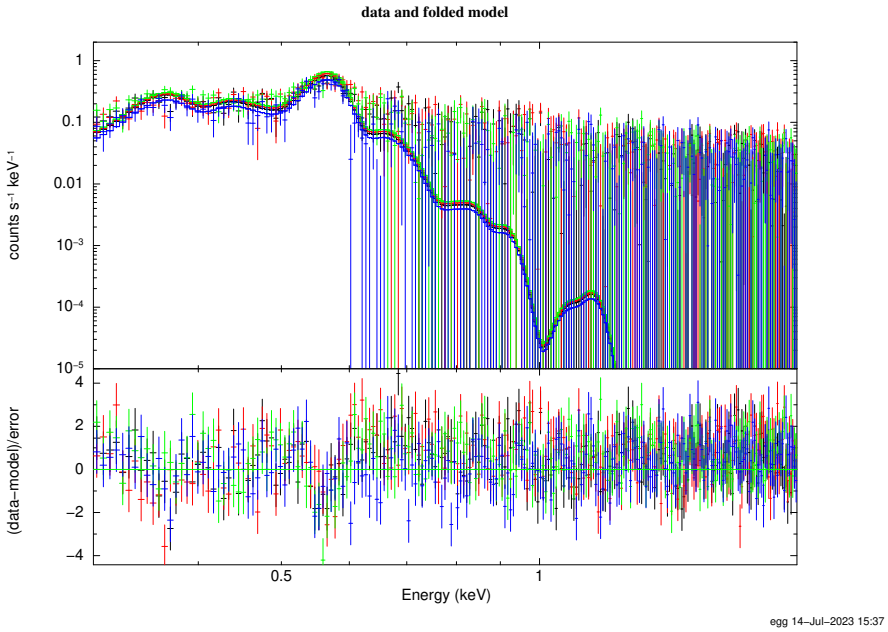

(b) Disk region

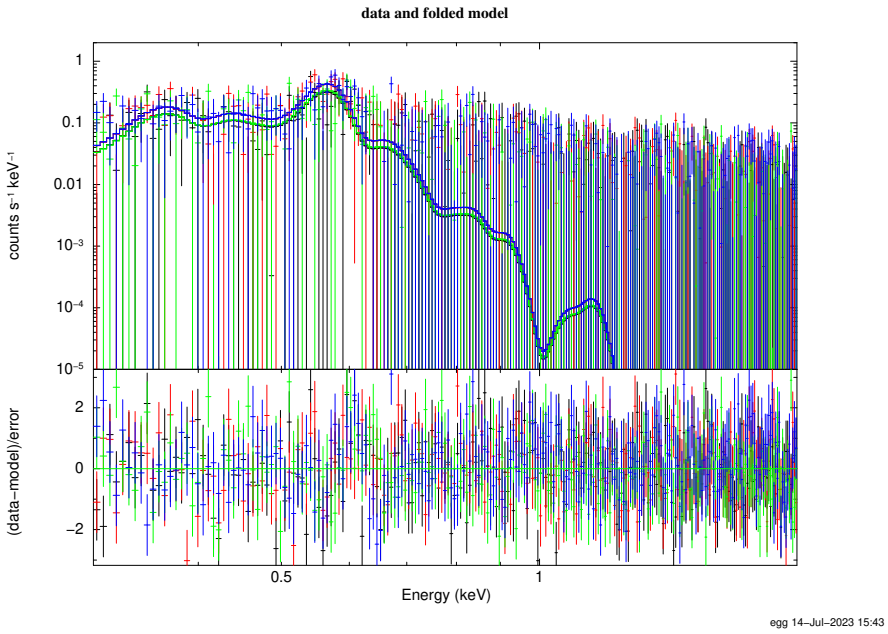

(c) Southern region

Figure 4.18.: SWCX fits for all three regions

region	kT in [keV]	red. χ^2
north	$0.1285^{+0.0014}_{-0.0014}$	1.23
disk	$0.1308^{+0.0012}_{-0.0012}$	1.51
south	$0.135^{+0.005}_{-0.004}$	1.08

Table 4.7.: SWCX kT values obtained through fitting for the three regions

4.3.6. LHB considerations

With improved SWCX fits and a smaller energy range, that should exclude the majority of the soft excess caused by the particle background, one last consideration was now to bring the fits into agreement with literature values of the LHB.

This had been very difficult before the adjustments detailed in the previous section. Due to the soft excess the apec shape of the LHB had been massively preferred to the acx2 shape of the SWCX. The reason for this can be seen in Figure 4.6. The SWCX and LHB components are in competition at lower X-ray energies. The only substantial difference in their shapes lies towards lower energies. While the apec of the LHB increases, the acx2

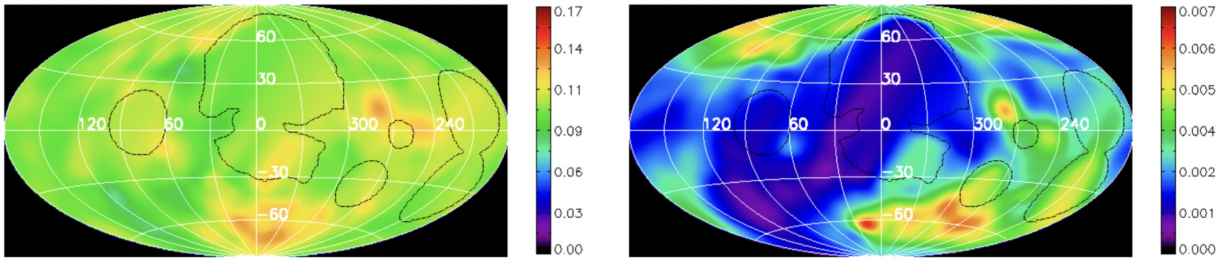

Figure 4.19.: (left) LHB temperature in keV (right) emission measure (EM) (taken from Liu et al. (2017))

component experiences a sharp drop with only a single peak remaining towards lower energies. With the addition of the soft excess this now lead to the spectrum resembling the LHB more strongly and, in turn, to the LHB norm being vastly overestimated. This effect was strongest in eRASS3 and 4 but also occasionally noticeable in eRASS2.

With the energy range of $0.2 - 0.3\,\mathrm{keV}$ excluded from the analysis, distinguishing the components in the fitting process now became difficult. Without the range containing their most discerning spectral characteristics their norms could change arbitrarily and lead to constant tension in the fit. Due to this it was decided to constrain both the temperature and the norm of the LHB to a reasonable literature range taken from Liu et al. (2017).

A map of the LHB emission can be seen in Figure 4.19. It can be seen that the temperature of the LHB emission in the region of interest lies at values of around $\sim 0.1\,\mathrm{keV}$, while its emission measure (EM) is fairly low. In order to translate the EM to an apec norm, the following equation was used, where η is the apec norm[5]:

$$\mathrm{EM} = \frac{\eta}{2.081 \cdot 10^{-4}} [\mathrm{cm}^{-4}\mathrm{pc}^{-1}] \tag{4.3.5}$$

The literature ranges for the kT and the EM of the three analysis regions were then estimated from the map in Figure 4.19. The EM values were converted to apec norm values with Equation 4.3.5. The resulting literature ranges for the LHB temperature, EM, and norm can be found in Table 4.8. The kT and norm parameters of the LHB model components were hereafter constrained to these ranges.

[5]Private communication: Dr. Jonathan Knies.

region	kT range in [keV]	EM range	apec norm range
north	$0.09 - 0.12$	$0.0009 - 0.00175$	$1.873 \cdot 10^{-7} - 3.642 \cdot 10^{-7}$
disk	$0.09 - 0.12$	$0.001 - 0.003$	$2.081 \cdot 10^{-7} - 6.243 \cdot 10^{-7}$
south	$0.1 - 0.13$	$0.0015 - 0.0035$	$3.1215 \cdot 10^{-7} - 7.2835 \cdot 10^{-7}$

Table 4.8.: LHB kT, EM, and norm literature ranges obtained from Figure 4.19 which was taken from Liu et al. (2017)

4.3.7. Northern region fits

To find the best final fit for the data in the northern region several of the best model configurations that were described in Section 4.3.4 were repeated with the improvements on the fit parameter bounds that were detailed in Sections 4.3.5 and 4.3.6.

The split absorption TBabs components with free nH parameters were abandoned at this point and only one TBabs was used in each fit hereafter, the nH values of which were frozen to the values found in Section 4.3.2. The reason for this was the fact that, with increasing complexity of the models, the free nH parameters started regularly taking implausibly small values in an increasing amount of fits, distorting the shapes of the model components and destabilizing the fits.
Additionally all models considered in this section contain vnei and vrnei parameters and, as the starting value of the τ parameter can have an impact on the final fit, fits with both $\tau = 10^{10}$ and $\tau = 10^{11}$ were conducted.

The description and results of these individual fits can be seen in Table 4.9. While many of the fits were of a similar goodness in eRASS1, a clear favorite could be seen to emerge at this point, when expanding the scope to all four eRASS. The model with a vapec component describing the CGM, gain offsets, and an additional vnei component with a starting value of $\tau = 10^{10}$ (upper bolded rows in Table 4.9) provides the best fit for eRASS1, 3, and 4 and nearly matches the best fit for eRASS2. Consequently this model configuration was decided on as the final model to be used in the spectral fits in this thesis. A plot of this model for eRASS1 can be seen in Figure 4.20.

In a final effort to improve the model, the disnht absorption model[6] by Locatelli et al. (2022) was tested in place of the TBabs model for modeling the nH absorption. This model was used in the work of Ponti et al. (2022). It is especially constructed to model greater ranges and differences in absorption over larger regions, which made the question of its possible effects on the final model in this work very interesting and promising. The model is available as a table model for different distributions of nH but can also be calculated for individual lists of nH values from the source code, which was the route taken

[6]Model and code available at http://www.brera.inaf.it/hotmilk/models.html.

description of the model	eRASS1	eRASS2	eRASS3	eRASS4
+ apec, gain, vnei, $\tau = 10^{10}$	1.3378	1.4808	1.6965	1.4899
#dof	4097	4094	4098	4098
+ apec, gain, vnei, $\tau = 10^{11}$	1.3280	1.5048	1.7090	1.4780
#dof	4098	4095	4097	4098
relaxed CGM & Cor pars + gain, vnei $\tau = 10^{10}$	1.3470	1.5520	1.6835	1.4671
#dof	4095	4095	4096	4096
relaxed CGM & Cor pars + gain, vnei $\tau = 10^{11}$	1.3763	1.5577	1.7280	1.4655
#dof	4097	4096	4097	4095
relaxed CGM & Cor pars + gain, vrnei $\tau = 10^{10}$	1.3796	1.6787	1.6375	1.5383
#dof	4096	4094	4093	4094
relaxed CGM & Cor pars + gain, vrnei $\tau = 10^{11}$	1.3246	1.5409	1.6922	1.4747
#dof	4095	4093	4095	4094
CGM vapec + gain, vnei $\tau = 10^{10}$	**1.3077**	**1.4811**	**1.5567**	**1.3647**
#dof	**4094**	**4092**	**4089**	**4090**
CGM vapec + gain, vnei $\tau = 10^{11}$	1.3296	1.5186	1.5703	1.3731
#dof	4094	4094	4091	4090
CGM vapec + gain, vrnei $\tau = 10^{10}$	1.3184	1.5249	1.6083	1.4149
#dof	4092	4092	4089	4089
CGM vapec + gain, vrnei $\tau = 10^{11}$	1.3157	1.4990	1.5990	1.3875
#dof	4092	4092	4089	4090
CGM vapec + gain, vnei $\tau = 10^{10}$, disnht	**1.2737**	**1.4560**	**1.5045**	**1.4004**
#dof	**4092**	**4094**	**4091**	**4091**

Table 4.9.: Final selection of possible fits for the northern region, their reduced χ^2 values, and the numbers of their degrees of freedom (#dof)

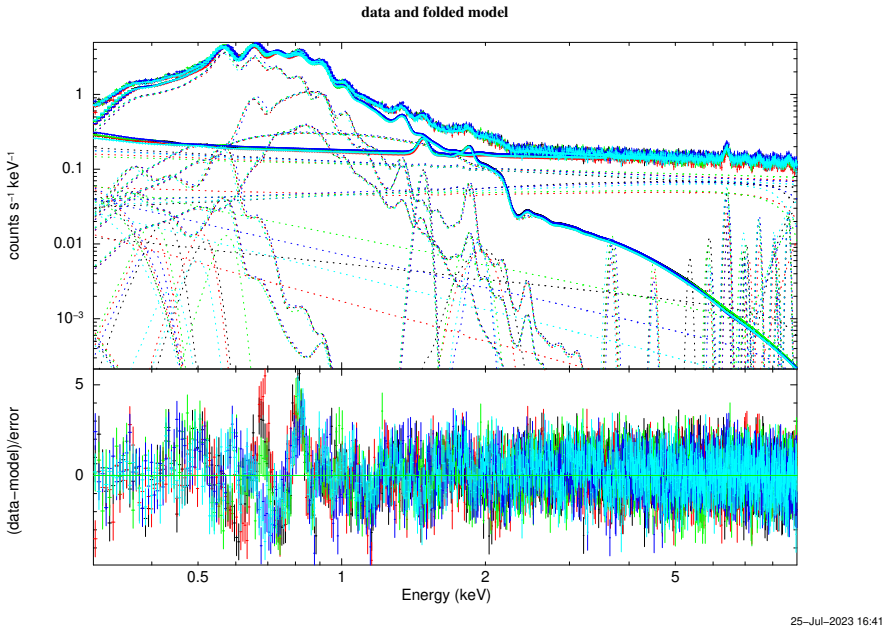

Figure 4.20.: Fit on the northern eRASS1 data with a CGM vapec component, gain offset, and an additional vnei component

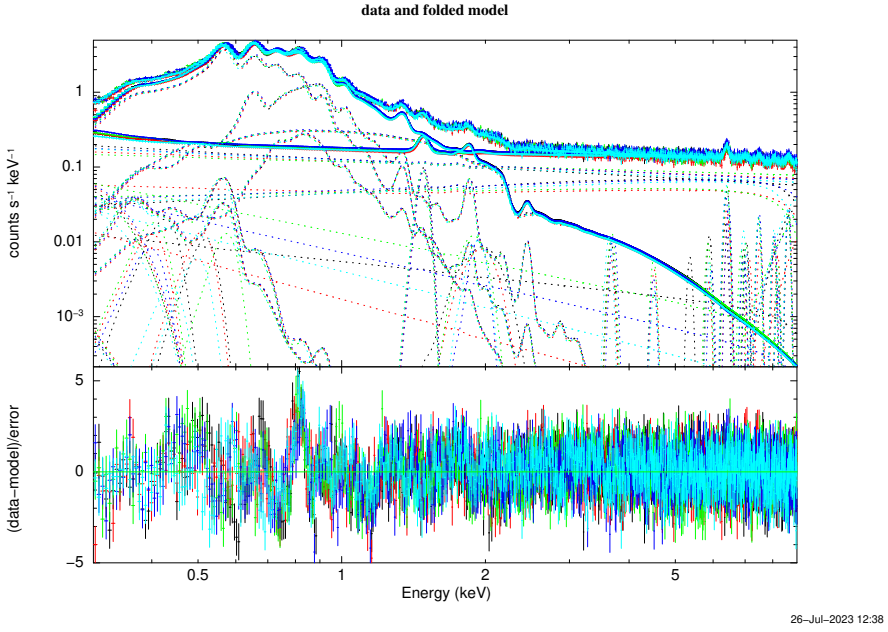

Figure 4.21.: Final fit on the northern eRASS1 data with disnht absorption

here. For the northern, southern, and disk region all nH values within the circular regions defined in Section 4.3.2 were extracted from the catalog of the HI4PI survey[7] by HI4PI Collaboration et al. (2016) through TAP.

The results of the fits with the disnht model can also be seen in Table 4.9 (lower bolded rows). It can be seen that the eRASS1, 2, and 3 fits improved noticeably, while the eRASS4 fit worsened. As this constituted an overall improvement in the quality of the fits, the disnht component was kept in the model, making the fits with disnht absorption the final fits that were used in the further steps of this work.

The final model thus amounted to the following:

$$\text{const} * \text{const} * (\text{acx2} + \text{apec} + \text{disnht} * (\text{apec} + \text{apec} + \text{powerlaw} + \text{vnei})) \tag{4.3.6}$$

A plot of the final model including disnht absorption can be seen in Figure 4.21; the plots for eRASS2, 3, and 4 can be found in the Appendix in Section A.3.1, as can the parameters of the final fits. Errors on the fit parameters were calculated using the `pyxspec_error_calc.py` script by Dr. Jonathan Knies; details on how this script works can be found in Section 5.1. As the Cor and vnei components are in competition at $\sim 0.6 - 0.8\,\text{keV}$, light constraints were applied in the eRASS3 and 4 fits to avoid one of the components being ousted from the fit.

4.3.8. Disk region fits

The final model determined in the previous section was used to fit the disk region data. Both fits using the final model with disnht absorption and fits using the same model with TBabs absorption were attempted. The disk region, as the largest of the three analysis regions, was a definite challenge to fit. Additionally it possesses the highest nH values of the analysis regions, which are also expected to vary the strongest due to the dust and gas present in the disk.

At this point the true strength of the disnht model emerged. It can be seen in Figure 4.22 that the model with TBabs absorption can not be properly fit to the data, leaving extremely large residuals and resulting in a reduced χ^2 of 3.98 (see Table 4.10). Using disnht absorption, however, the fit succeeds, resulting in a reduced χ^2 value of 1.42. Similar improvements can be seen for eRASS2, 3, and 4, as is detailed in Table 4.10. It can thus be seen that the nH variations have a very large impact on the fitting of large regions and should definitely be taken into account the fitting process to ensure correct fits.

Consequently the fits with disnht absorption were used in the further steps of this work. Light constraints on the temperatures of some individual components were again applied

[7]Catalog available via VizieR at https://doi.org/10.26093/cds/vizier.35940116.

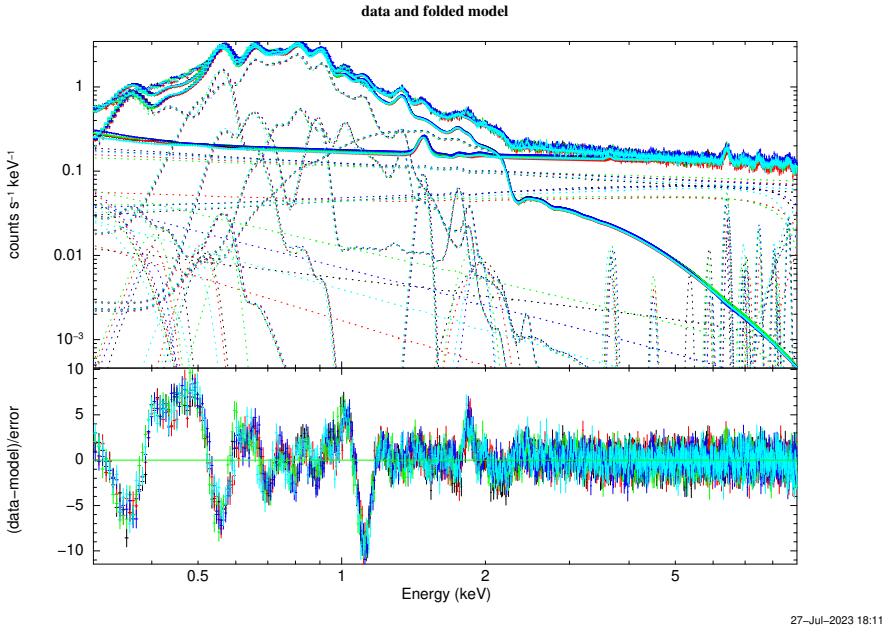

(a) TBabs absorption

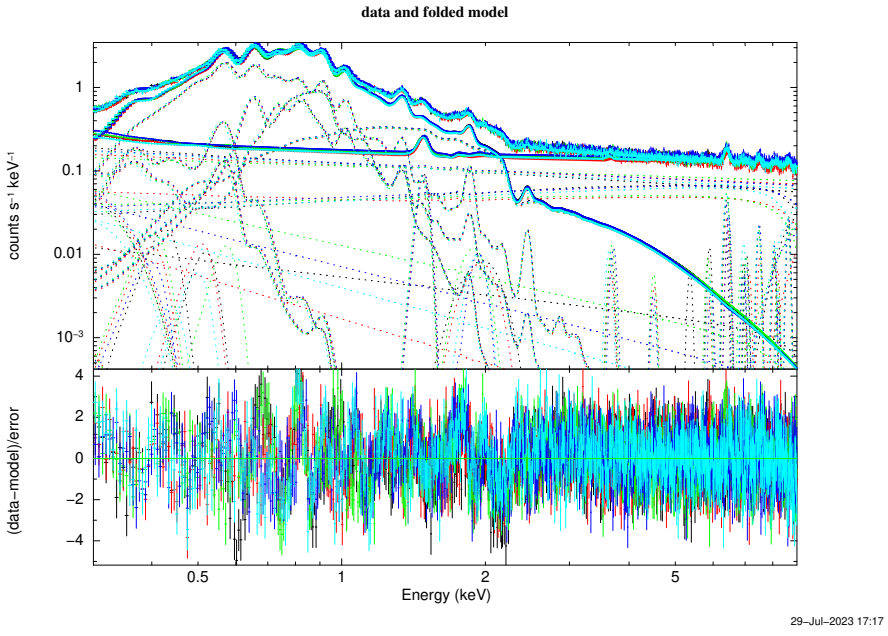

(b) disnht absorption

Figure 4.22.: Fits on disk eRASS1 data using (a) TBabs absorption and (b) the final model with disnht absorption

description of the model	eRASS1	eRASS2	eRASS3	eRASS4
CGM vapec + gain, vnei $\tau = 10^{10}$	3.9831	4.2547	4.2390	4.8192
#dof	4090	4089	4078	4091
CGM vapec + gain, vnei $\tau = 10^{10}$, disnht	**1.4239**	**1.4937**	**1.5910**	**1.6198**
#dof	**4089**	**4089**	**3266**	**4087**

Table 4.10.: Final fits for the disk region with TBabs and disnht, their reduced χ^2 values, and the numbers of their degrees of freedom (#dof)

to ensure no component was ousted from the fit or shifted to the detriment of the quality of the fit. For the final eRASS3 fit TM4 was excluded from the fitting process, as it showed irregular behavior as compared to the other TMs, as was already observed in Section 4.3.5.

The reduced χ^2 values of the final fits can be found in Table 4.10 and a plot of the final eRASS1 fit in Figure 4.22b. The eRASS2, 3, and 4 plots can be found in the Appendix in Section A.3.2, as can the parameters of the final fits.

4.3.9. Southern region fits

As was described in the previous sections for the other regions, the final fit model with disnht absorption was fitted to the data of the southern region. Again light temperature limits were applied in some cases to avoid a shift of components to the detriment of the goodness of the fit.

The reduced χ^2 values of the fits can be found in Table 4.11, while a plot of the eRASS1 fit can be seen in Figure 4.23. The eRASS2, 3, and 4 plots can be found in the Appendix in Section A.3.3, as can the parameters of the final fits.

description of the model	eRASS1	eRASS2	eRASS3	eRASS4
CGM vapec + gain, vnei $\tau = 10^{10}$, disnht	**1.3440**	**1.2376**	**1.3925**	**1.5888**
#dof	**4095**	**4094**	**4093**	**4092**

Table 4.11.: Final fits for the southern region, their reduced χ^2 values, and the numbers of their degrees of freedom (#dof)

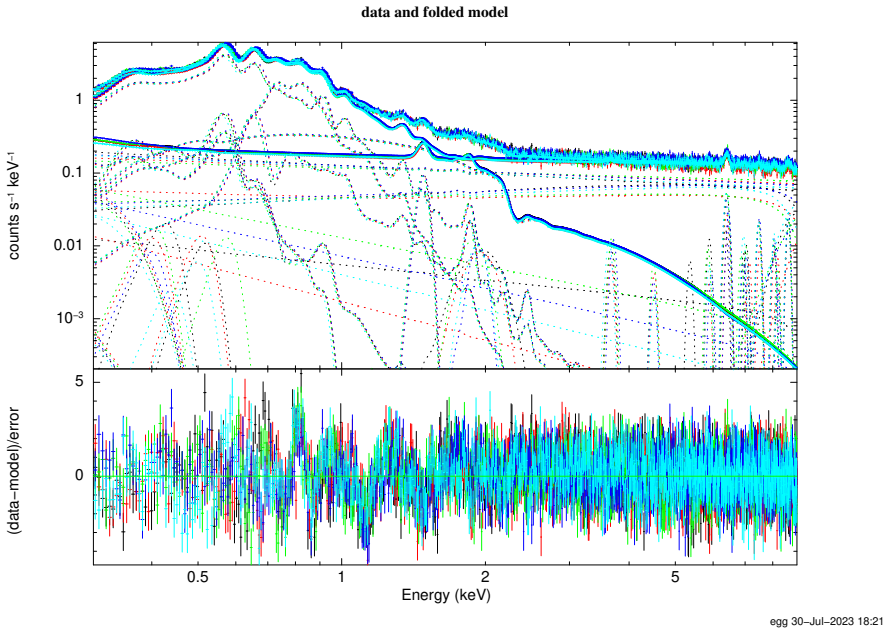

Figure 4.23.: Final fit on southern region eRASS1 data

5. Line detection

The next step in the analysis was the detection of potentially unknown residual spectral line features, which will be described in this part of the thesis. After a description of the script that was used and the process of detection, the results are presented. Afterwards efforts to find correlations between detected line features and known atomic/CX lines are described.

5.1. Line detection script

To automate the search for heretofore unknown spectral lines the Python/PyXspec script `line_finder.py` was created to scan the residuals for line features. The script was based on an earlier Xspec script by Dr. Denys Malyshev from the University of Tübingen, who has conducted dark matter decay line searches in the past (see Malyshev et al. (2014) for an example). Its Python structure was based on a PyXspec template by Dr. Jonathan Knies.

The script follows the approach that is illustrated in Figure 5.1. An additional Gaussian line with fixed energy and width is added to the final fit, in which every other parameter has been frozen. The fit is then refitted, allowing the norm of the Gaussian to vary and to eventually reach its best fit value with a minimum of 10^{-12}. This value was chosen to lie below probable influence on the fit but to ensure that no norms < 0 could occur, as this would cause issues in the error calculation. Afterwards the 1, 2, and 3σ errors of the Gaussian norm are calculated. For this the `pyxspec_error_calc.py` routine by Dr. Jonathan Knies was used. This script first attempts to calculate each error using the PyXspec `error` command. As the `error` command is known to fail or run into issues frequently, any time the output error string does not read 'FFFFFFFF', which denotes an error calculation without issues, the error calculation is repeated using `steppar` (Arnaud et al., 2023). The script automatically runs as many iterations of `steppar` as necessary to determine the errors of the parameters. The energy of the Gaussian, the best fit value of the Gaussian norm, the errors of the Gaussian norm, and the χ^2 values of the fit before and after the addition of the Gaussian are recorded and printed into an output file. Then the original fit is reloaded and the process repeats.

By varying the energies of the Gaussian lines in small increments an energy range can thus be scanned for unknown spectral lines. The resulting changes in the χ^2 values can be used to identify possible line detections, as an improvement of the fit with the addition of

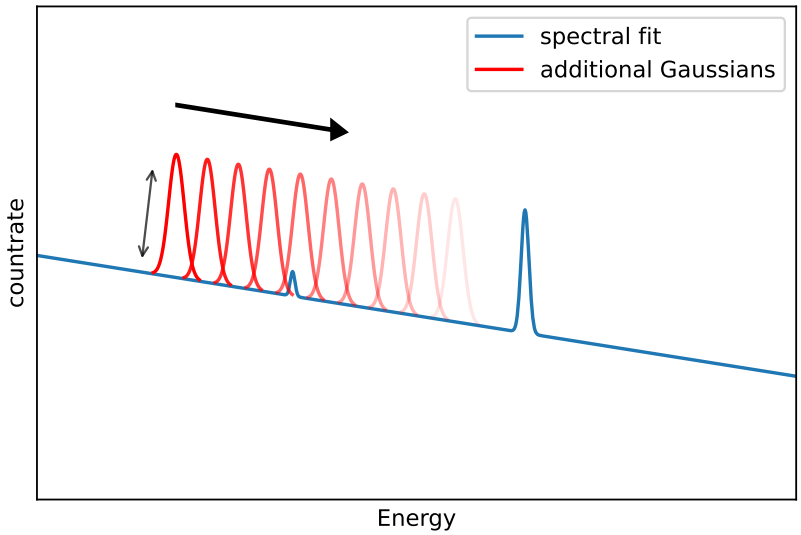

Figure 5.1.: Schematic visualizing the fitting process of the line detection script

the Gaussian line points to positive residuals in the original fit. Meanwhile, the best fit Gaussian norms can give a measure for the flux and brightness of potential lines, as the Gaussian norm is defined to be equivalent to the line flux (Arnaud et al., 2023).

The width of the Gaussian, i.e. its sigma parameter, depends on the velocity dispersion of the dark matter in the Milky way, which takes a value of $v \sim 200\,\frac{\mathrm{km}}{\mathrm{s}}$, resulting in a Doppler-broadening of $\frac{\delta E}{E} \sim \frac{v}{c}$ (see Dessert et al., 2023 and references therein). This broadening was taken into account in the fitting process. As it results in widths of only a few eV, it is, however, not expected to signify against the intrinsic broadening of lines due to the resolution of eROSITA.

The resulting change in χ^2 with the addition of a Gaussian, $\Delta\chi^2$, can be converted into a σ measure for the significance of a detection as follows. This ensures a clear statistical classification of results and is often done to gauge the statistical validity of detection results, e.g. by Boyarsky et al. (2014).

The probability p that the model with the additional line is accurate over the original model is given by the χ^2 cumulative distribution function $F(\Delta\chi^2; k)$ (scipy.stats.chi2.cdf(x;k) in Python (The SciPy community, 2023a)), where k is the number of additional degrees of freedom (in the present case one: the Gaussian norm), so (Wall and Jenkins, 2012):

$$p = F(\Delta\chi^2; 1) \tag{5.1.1}$$

This probability is now rephrased in terms of the σ of a Gaussian distribution. This $n\,\sigma$ value gives a measure for the percentage of the entire area beneath a Gaussian function in the "$n\,\sigma$-interval" $[x_0 - n\sigma, x_0 + n\sigma]$ around its central value x_0. For 3σ this is already a value of 99.73% (Wall and Jenkins, 2012). For this the percent point function $F'(p)$ (scipy.stats.norm.ppf in Python (The SciPy community, 2023b)) is used as follows:

$$\sigma = F'\left(\frac{p}{2} + \frac{1}{2}\right) \tag{5.1.2}$$

As the percent point function takes probability values that encompass the entire left tail of the Gaussian, the "shifting" of the probability in Eq. 5.1.2 is necessary to ensure a correct conversion of values. This was confirmed through testing of this approach in order to ensure the correct calculation of σ values.

It is important to note at this point that a 3σ detection in this case does not necessarily conclusively prove the existence of a line feature at the given energy. It can only show that positive residuals are present and how vastly their correction improves the fit. Whether these residuals are line-like can, however, only be determined by analyzing the results and residuals over the course of a scan, and searching for the presence of line-like features in the results. This process is limited by the resolution of eROSITA.

Using this approach all final fits with disnht absorption described in the previous sections were scanned for lines with the `line_finder.py` script over an energy range from 2 to 9 keV in steps of 25 eV. Energies below 2 keV were omitted, as even the final fits contain a higher amount of residuals at these energies.

5.2. Line detection results

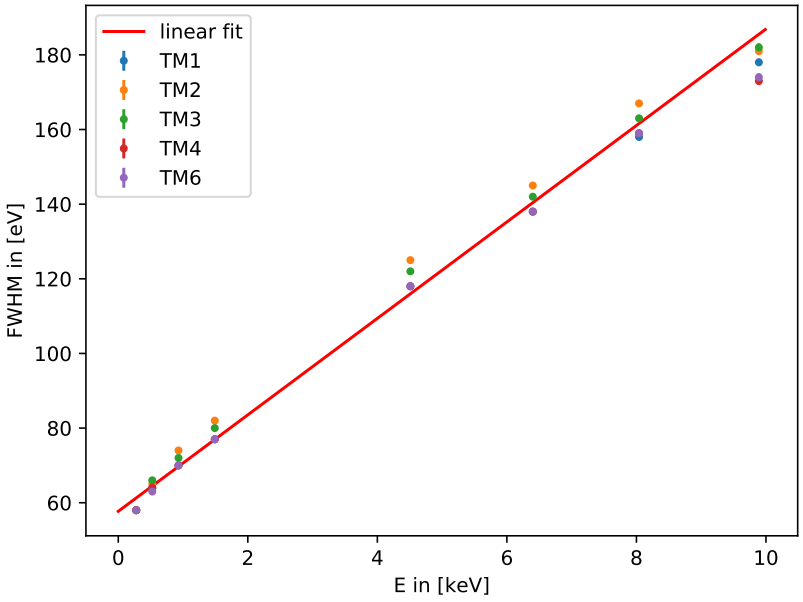

Figure 5.2.: Linear fit approximation for the eROSITA energy resolution (calibration FWHM values taken from Dennerl et al. (2020))

The results of the line detection process were plotted and evaluated. It was discovered that peaks in the σ significances of detection exist which point to possible line features.

The peaks in the σ values were detected using the scipy tool `scipy.signal.find_peaks` using a minimum value of three datapoints between subsequent peaks to filter out very small fluctuations. Then the lines were sorted using the script `sort_lines.py`, that was created for this express purpose. Each peak was assigned a width based on eROSITA's energy resolution at its respective peak energy. Added to that was the energy difference of one step in the line scanning process, i.e. 25 eV, amounting to the following equation, where w_{tot} is the total peak width, while w_{res} is eROSITA's resolution at the specified energy E:

$$w_{\text{tot}} = w_{\text{res}}(E) + 25\,\text{eV} \tag{5.2.1}$$

To approximate values for the energy resolution of eROSITA for all energies a linear fit to the calibration values from the ground calibration (published in Dennerl et al. (2020) among others) was performed. The resulting parameters of this fit with the function $w_{\text{res}}(E) = a \cdot E + b$ can be seen in Figure 5.2. The fit parameters are listed in Table 5.1.

The finite resolution of eROSITA makes it impossible to completely resolve the detected

parameter	value
a	$(12.92 \pm 0.21) \cdot 10^{-3}$
b	$(57.7 \pm 0.6)\,\mathrm{eV}$

Table 5.1.: Best fit parameters for linear approximation of eROSITA's energy resolution

features into lines. As mentioned before, it can thus not always be conclusively decided whether the detected features do posses a line shape. Since the step size of 25 eV that was used in the line scanning process is smaller than the resolution of eROSITA, peaks with distances between their centers that were smaller than either of their assigned widths were merged. The merged peak was then assigned an energy and norm value resulting from a weighted average with respect to the σ values of the original peaks. A weighted σ value was then calculated as a weighted average of the differences of the individual peak energies to the new energy value. As all thus obtained and merged line features are possible lines they are treated as such within the scope of this thesis. Whether that assessment is accurate would need to be the object of further study.

`sort_lines.py` then identified instrumental lines by their overlap with the FWC instrumental lines, as can for instance be seen in Figure 5.3. Due to the fact that the values the Gaussian norm could take in the line scan were limited to $\geq 10^{-12}$, only instrumental lines with norms above this value were considered for this purpose. To also broaden the narrow instrumental lines in accordance with the energy resolution of eROSITA, the following formula was adapted from Kitayama et al. (2014) to combine the width of the line resulting from spectral resolution, W_{inst}, with the intrinsic width $W_{\mathrm{intrinsic}}$ caused by other factors:

$$W^2 = W_{\mathrm{inst}}^2 + W_{\mathrm{intrinsic}}^2 \tag{5.2.2}$$

As most instrumental lines are extremely narrow, this results in $W \approx W_{\mathrm{inst}}$ for most lines.

Lists of all detected lines of all σ for each region and eRASS can be found in Section A.4 in the Appendix. All lines identified with instrumental lines are denoted as "instrumental", while lines resulting from the merging of two close lines are marked "averaged".

In the following analysis only the non-instrumental lines that were detected with a significance over the threshold of 3σ were investigated as significantly detected features.

The total number of photons present in the energy range of each line was finally calculated using the `ignore` command of PyXspec to exclude all but the desired energy range and the `show` command to output the count rate and exposure time for each TM. The total number of photons N_{ph} for each line was calculated by multiplying the count rate with the exposure time and summing over all TMs (Gordon and Arnaud, 2022).

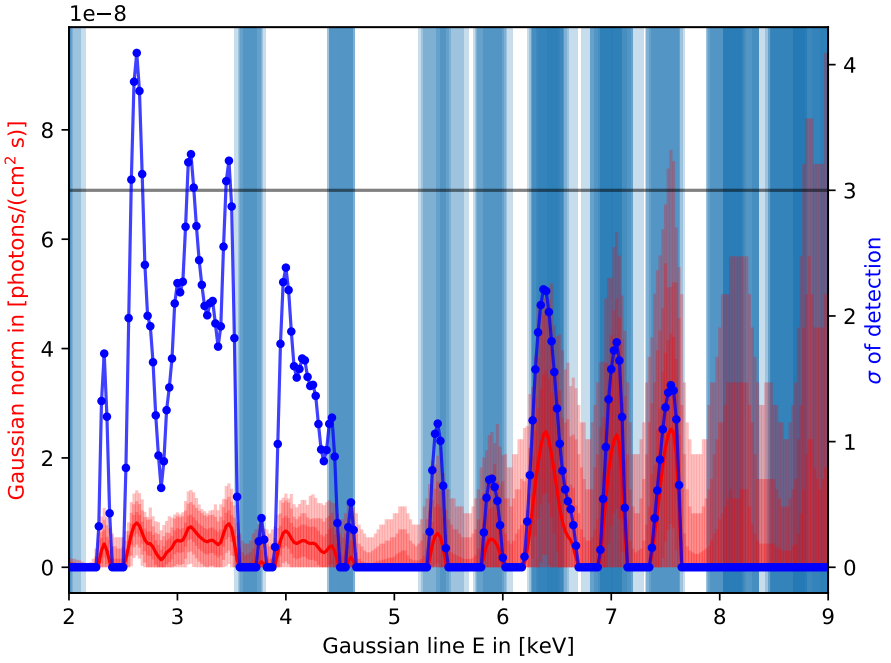

Figure 5.3.: Plot of detected lines in the northern region for eRASS1 with errorbars, red: Gaussian norm with 1, 2, and 3σ errorbars, blue: σ significances of the detection, light blue background: location of instrumental lines for eROSITA

The statistical error σ_{ph} on the number of photons can then be found by following Poisson statistics, which describe the detections of photons in X-rays. The variance of a Poisson distribution is equal to its average value (Wall and Jenkins, 2012). From this it follows that:

$$\sigma_{\mathrm{ph}} = \sqrt{N_{\mathrm{ph}}} \tag{5.2.3}$$

This statistical error σ_{ph} serves as a reality check for the line feature detections in this work by showing the pure statistical uncertainties the detection of X-ray photons is subject to.

A table of the non-instrumental $> 3\sigma$-lines with their properties, including N_{ph} and σ_{ph}, can be found in the final line list in Table 5.2 in the following section.

Detailed plots of the line detections were created to further showcase these results. One such plot can be seen for eRASS1 in the northern region in Figure 5.3. The best fit norm of the Gaussian line for each energy is plotted in red with its respective 1, 2, and 3σ errorbars. Meanwhile, the statistical significance of the detection in σ is shown in blue, with visible individual datapoints to give a better sense of scale to the resolution of the scanning process. Additionally the extent of eROSITA's instrumental lines (as defined in the FWC

model) was drawn into the background of the plot in light transparent blue.

Three detected line features $> 3\sigma$ can be seen very clearly in Figure 5.3. It can also be seen that there is some shift and overlap present in the FWC lines. This is due to the fact that the lines are located at slightly different energies for different TMs.

Figure 5.3 shows very clearly that the Gaussian norms and σ values rise and fall in parallel. It also becomes clear that, especially at higher energies above 5 keV, the detected features trace the locations of the instrumental lines. This points to a certain measure of disparity between the predictions of the FWC model and the strength of the instrumental lines in the actual data. It can also be seen that the errorbars of the Gaussian norms grow with higher energies, while the significances of the line detections decrease. This is likely due to the increasing influence of the instrumental lines on the data, as well as due to the decreasing effective area of eROSITA at these energies. It stands to reason that most of the non-instrumental line detections should occur at energies of below ~ 5 keV.

The line detection plots for the other regions and eRASS can be found in Section A.5.1 in the Appendix. Section A.5.2 in the Appendix, meanwhile, contains plots of the same data where the Gaussian norms have been plotted in logarithmic scale and without their errorbars for better visibility. In these plots the parallel rise and fall of the Gaussian norms with the σ values is more clearly visible, while the plots with errorbars (such as Figure 5.3) emphasize the scale of the Gaussians and their errors much more clearly.

It can be seen in the Plots in Section A.5.1 that the line detections do not always correlate quite as well with the instrumental lines as they do in Figure 5.3. Nevertheless, for the large majority of lines above ~ 5 keV a definite correlation with the instrumental lines can be seen. There are also noticeable recurring features, such as a block of several lines at around ~ 3 keV, a single line below ~ 2.5 keV, and an instrumental line at around 6.5 keV, that confirm the presence of recurring features in the spectral residuals.

It is, however, not possible to resolve the different detections over all regions and eRASS into distinct line features, as they are to widespread over the available energy range. A plot showing the location and overlap of all non-instrumental lines with significances $> 3\sigma$ can be seen in Figure 5.4. Furthermore, plots showing the line overlap of all lines for the different regions and eRASS can be seen in Section A.5.3 in the Appendix.

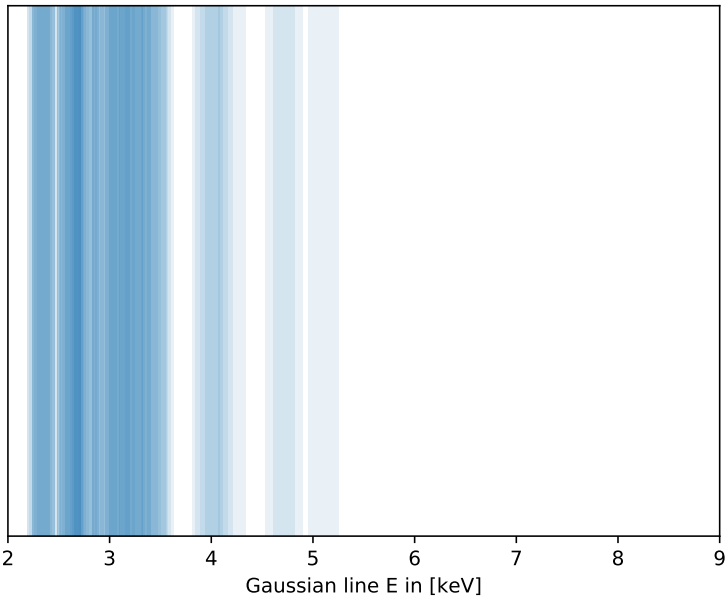

Figure 5.4.: Plot showcasing the location and overlap of all detected lines with $> 3\sigma$ significance

5.3. Line identification

As the final step in this research work the detected line features were correlated with known atomic and CX lines to find possible origins of their emission aside from sterile neutrino decay.

First the lines were compared against atomic data by using the AtomDB Webguide feature[1] (Smith et al., 2018) to search for known atomic lines in their energy range. Through this method matches for each line could be found. This very good correlation could in part, of course, also be caused by the large assigned widths of the lines via the energy resolution of eROSITA and the scanning step size used in the line detection.

The match with the strongest emissivity is listed in the final line list in Table 5.2. While the emissivities of the lines vary from $\sim 10^{-17}$ to $\sim 10^{-19}$ $\frac{\mathrm{ph\,cm^3}}{\mathrm{s}}$, i.e. over two to three orders of magnitude, it can, within the framework of this analysis, not conclusively be decided which line features could quantitatively be caused by their associated emission lines and which could not, as the physical properties of the potentially emitting material are unknown.

[1] Available at http://www.atomdb.org/Webguide/webguide.php.

With CX emission being another potential source of X-ray line emission, as was described in Section 2.2, a comparison of the detected lines with charge exchange lines was also deemed necessary. However, this proved to be a much more challenging task, as, due to the complicated nature of CX emission, comprehensive catalogs, such as the AtomDB catalog for atomic line emission, do not exist in the energy range of 2 to 9 keV. Thus, to be able to gauge possible contributions of CX emission to the detected lines a different route was taken.

As CX emission is very dependent on the physical parameters of the emitting medium, especially its temperature, ten acx2 models with temperatures of 0.1 to 1.0 keV were stacked to form a potential profile of CX lines as they might occur over this temperature range. Solar abundances were chosen, the `recombtype` was set to 2, and the `acxmodel` 8 was specified. Meanwhile, the velocity of the medium was set to 40 $\frac{\text{km}}{\text{s}}$ in accordance with the velocity of intermediate velocity clouds (IVCs), a possible source of CX emission in the Milky Way (see references in Ponti et al., 2022). This, compared to other potential sources of CX emission, very low velocity was chosen, as higher velocities dampen the scale of the line emission. As a norm the best fit geometric norm of the SWCX component of the northern region in eRASS1 was used to gain some quantitative measure of scale. The resulting line profile was compared with the detected lines (Foster, 2023).

It can be seen in Figure 5.5 that a multitude of CX emission lines is present at energies between 2 and 5 keV, where most of the non-instrumental line detections occurred. The emission lines shown in Figure 5.5 that were found in the eRASS1 data of the northern region with $> 3\sigma$ could thus all be impacted by CX emission. As for the atomic lines, the scale of this influence remains unknown in the absence of concrete knowledge of the physical properties of the emitting medium. An influence on the line emission is thus a possibility. Overlap with possible CX lines exists for all detected lines, as can be seen in the other plots in Section A.6 in the Appendix.

To get a sense of scale of the magnitude of the CX emission, the Gaussian line detected at 2.625 keV in the eRASS1 data of the northern region was plotted into the CX model to scale and folded with the data. It can be seen in Figure 5.6 that this results in emission of similar orders of magnitude. As, however, the geometric norm of the SWCX emission was used for the CX modeling, which scales with $\frac{1}{D^2}$, where D is the distance to the source, a CX source outside the LHB would need to have a by $\sim 10^{40}$ larger extent to reach the same scale. An origin in only CX emission thus seems unlikely for the detected lines (Foster, 2023; see references in Ponti et al., 2022).

The final line list containing all detected non-instrumental $> 3\sigma$ lines can be seen in Table 5.2.

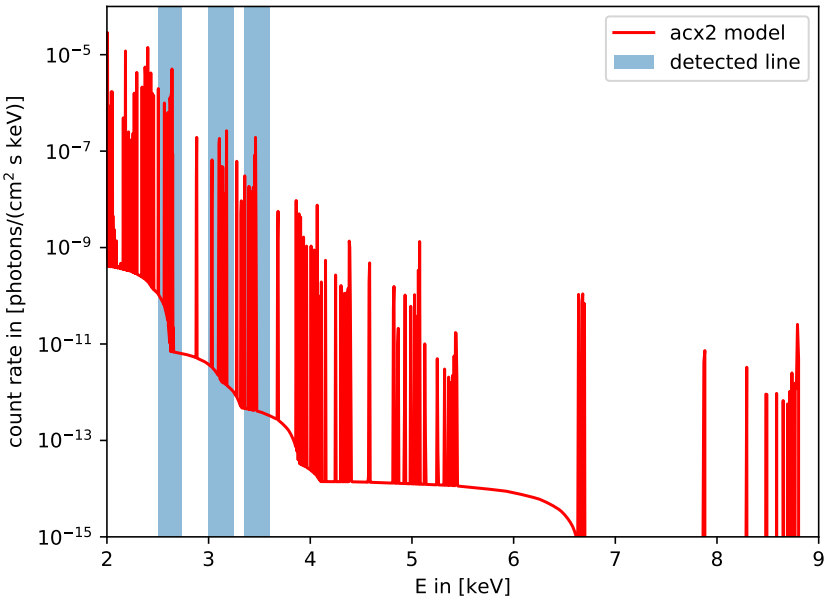

Figure 5.5.: Plot showing the location of detected line features (blue) against line emission in the acx2 model (red) for the northern region in eRASS1

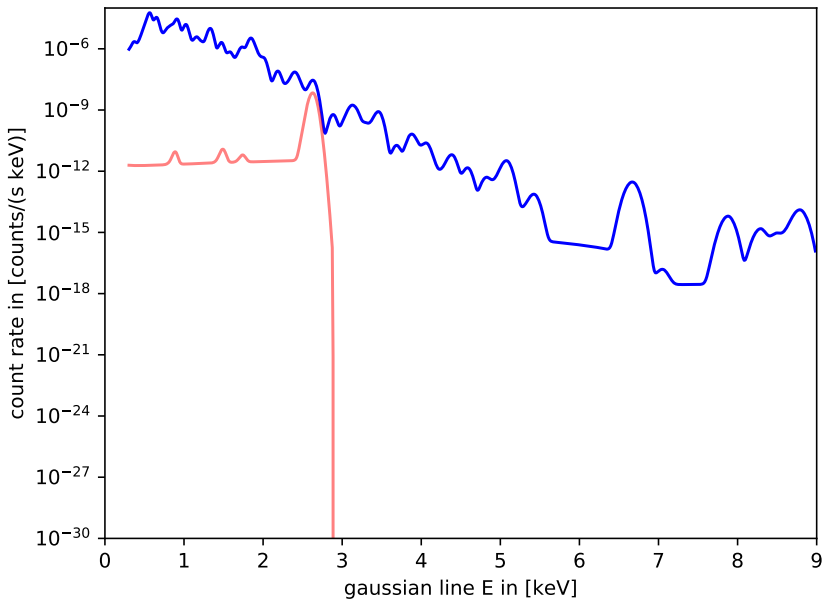

Figure 5.6.: Plot of a detected line (red) compared to the acx2 CX emission model (blue), both models are folded with the data for the northern region in eRASS1

energy [keV]	peak σ	width [keV]	average norm [ph/(cm^2 s)]	region, eRASS	atomic line	N_{ph}	σ_{ph}
2.625	4.09306	0.11662	8.11979e-09	north, 1	SXVI	13159.64	114.71547
3.125	3.28727	0.12307	7.40130e-09	north, 1	ArXVII	16038.854	126.6446
3.475	3.23539	0.1276	7.96029e-09	north, 1	SXVI	15877.742	126.00691
2.325	5.04696	0.11274	1.22034e-08	north, 2	SXV	18814.546	137.16613
2.62528	3.79103	0.11662	7.31994e-09	north, 2	SXVI	18485.064	135.95979
3.225	3.72581	0.12437	8.31039e-09	north, 2	ArXVII	14782.612	121.58377
3.45	3.05158	0.12727	7.08180e-09	north, 2	ArXVIII	14752.188	121.45859
4.025	3.30829	0.1347	8.87259e-09	north, 2	CaXIX	18459.013	135.86395
2.3	5.79061	0.11242	1.26718e-08	north, 3	SiXIV	20789.3362	144.18508
2.65	5.46196	0.11694	1.01466e-08	north, 3	SXVI	20027.1614	141.51735
3.025	6.06273	0.12178	1.24655e-08	north, 3	ArXVII	19971.6295	141.32102
3.2	4.85439	0.12404	1.05149e-08	north, 3	ArXVII	19870.8631	140.96405
2.4	5.45145	0.11371	1.16595e-08	north, 4	SXV	17142.062	130.9277
2.775	4.99145	0.11855	1.08985e-08	north, 4	SXV	13084.202	114.3862
3.275	4.72057	0.12501	1.05627e-08	north, 4	CaXIX	13148.15	114.66538
4.075	3.82465	0.13535	1.04676e-08	north, 4	CaXX	17971.357	134.05729
4.675	3.9273	0.1431	1.38943e-08	north, 4	CaXIX	17565.486	132.53485
2.675	4.04114	0.11726	8.46941e-09	disk, 1	SXVI	28778.228	169.64147
2.925	3.73528	0.12049	8.22076e-09	disk, 1	SXV	28397.367	168.51518
3.075	4.68303	0.12243	1.03729e-08	disk, 1	ArXVII	27978.041	167.26638
3.35	3.62136	0.12598	8.40570e-09	disk, 1	ArXVIII	27512.027	165.8675
2.6	5.30648	0.11629	1.04445e-08	disk, 2	SXVI	32267.668	179.63204
2.75	5.22012	0.11823	1.16669e-08	disk, 2	ClXVI	30684.047	175.16862
2.95	4.29385	0.12081	9.06762e-09	disk, 2	SXV	30429.804	174.44141
3.075	5.14112	0.12243	1.09502e-08	disk, 2	ArXVII	31013.8	176.10735
3.2	3.91415	0.12404	8.67223e-09	disk, 2	ArXVII	30524.899	174.71376
2.35	5.62356	0.11306	1.73032e-08	disk, 3	SXV	25148.57	158.58301
2.625	inf[2]	0.11662	1.99536e-08	disk, 3	SXVI	24571.214	156.75208
2.775	6.40148	0.11855	1.69120e-08	disk, 3	SXV	23197.916	152.30862
3.175	7.99157	0.12372	2.09653e-08	disk, 3	ArXVII	23421.145	153.03968
3.5	3.10746	0.12792	8.38787e-09	disk, 3	KXVIII	22448.962	149.82978
3.95	4.2173	0.13373	1.25024e-08	disk, 3	CaXIX	22321.404	149.40349
4.2	3.59619	0.13696	1.15533e-08	disk, 3	CaXX	21832.416	147.75796
4.75	3.28204	0.14407	1.33360e-08	disk, 3	CaXX	22245.282	149.14852

Continued

[2]This very high and undefined σ value was caused by the large degree of improvement the fit experienced through the addition of the Gaussian. The probability that the fit with the additional Gaussian is preferred is approaching one, leading to the σ value rising toward infinity.

2.35	8.12589	0.11306	2.18242e-08	disk, 4	SXV	35389.53	188.12105
2.6	6.21998	0.11629	1.24156e-08	disk, 4	SXVI	34155.549	184.8122
2.725	6.50702	0.11791	1.42357e-08	disk, 4	SXVI	32860.016	181.27332
2.95	6.48667	0.12081	1.38637e-08	disk, 4	SXV	32146.43	179.29426
3.125	8.0414	0.12307	1.75848e-08	disk, 4	ArXVII	32294.806	179.70756
3.275	5.8014	0.12501	1.28916e-08	disk, 4	ArXVIII	30799.551	175.49801
2.35	4.25964	0.11306	1.75113e-08	south, 1	SXV	11065.8352	105.19427
2.60028	3.25323	0.1163	1.04120e-08	south, 1	SXVI	13435.0817	115.9098
2.95	4.073	0.12081	1.43727e-08	south, 1	SXV	10890.3059	104.35663
2.375	3.23378	0.11338	1.25587e-08	south, 2	SXV	10300.7824	101.49277
2.6	3.55453	0.11629	1.14638e-08	south, 2	SXVI	13385.9869	115.69783
2.825	3.16726	0.1192	1.15322e-08	south, 2	SXV	10117.3409	100.58499
3.425	3.01326	0.12695	1.20525e-08	south, 2	ArXVIII	13260.8306	115.15568
2.35	4.6576	0.11306	1.77263e-08	south, 3	SXV	19355.7432	139.12492
3.375	3.20696	0.1263	1.12372e-08	south, 3	ArXVIII	15325.8005	123.79742
2.3	6.01347	0.11242	2.03413e-08	south, 4	SiXIV	20040.689	141.56514
2.675	8.12589	0.11726	2.40681e-08	south, 4	SXVI	19725.383	140.44708
2.975	7.17595	0.12114	2.27862e-08	south, 4	SXV	19442.596	139.43671
3.225	6.15415	0.12437	2.08977e-08	south, 4	ArXVII	19118.159	138.26843
3.4379	6.46361	0.12712	2.31103e-08	south, 4	ArXVIII	19473.133	139.54617
3.975	6.02943	0.13406	2.42613e-08	south, 4	CaXIX	19149.233	138.38075
5.1	3.13214	0.14859	2.08415e-08	south, 4	CaXX	19672.445	140.25849

Table 5.2.: All non-instrumental lines with significances $\sigma > 3$ with their parameters, including atomic line counterparts, total photon numbers N_{ph}, and their standard deviations σ_{ph}

6. Discussion

The key findings of this work concern both the modeling of the diffuse X-ray background and the line detections in the residuals.

The key result of this work is, of course, the detection of line features in the residuals of the diffuse eROSITA X-ray background. While many line-like features were detected, all of them can be associated with known atomic lines as well as possible influence from CX emission, resulting in a non-detection of otherwise unassociated lines that could be connected to sterile neutrino decay. Lines at, or close to, the 3.5 keV line could also be found. A detection was made at 3.5 keV in the disk region for eRASS3, as well as at 3.475 keV in the northern region for eRASS1. Due to the limited energy resolution of eROSITA, both of these lines could, however, be associated with known atomic lines, KXVIII and SXVI respectively, while CX contribution is also a possibility, as was shown by Gu et al. (2015) and Shah et al. (2016). Thus, at this point in time, no evidence of sterile neutrino decays, at 3.5 keV or elsewhere, could be found.

These insights, of course, depend on the spectral fits of the Galactic diffuse X-ray background they are based on. In this work a spectral model was found that could describe the diffuse X-ray emission detected in the observed regions well by modifying the model by Ponti et al. (2022). The current models of the diffuse X-ray background are phenomenological descriptions of the observed emission and many factors concerning the components of this emission are still uncertain. While it is not the purpose of this work to characterize the diffuse X-ray emission in the Milky Way, the best fit models found in this work can nevertheless yield useful information toward further improvement in spectral modeling. A key part of this reasoning is the large region size of the regions analyzed in this work. It amplifies discrepancies between the model and data and could thus especially point out areas where the two still diverge for current models. One factor to showcase this might, for instance, be the additional components that were necessary to model the spectra, especially the apparent necessity for a vnei/vrnei component, which was present in all of the better model versions, with the final model, too, containing an additional vnei component. This could point to non-equilibrium processes being present in the observed emission. In the process of this analysis it was also confirmed that the more detailed modeling of the nH absorption through the disnht model by Locatelli et al. (2022) massively improves the quality of the fit especially for larger areas with more nH variation, such as the disk region analyzed in this work.

One additional interesting result arising from the line detection are the apparent slight

discrepancies between the data and the FWC model that can be seen very well in the way the detected line features at higher energies align with the instrumental lines (see Figure 5.3 and Section A.5.1). While not all lines align smoothly with the FWC lines, there is a clear strong tendency. At Gaussian norms of around $\sim 10^{-8}$ this effect is not very large quantitatively, but it is made visible here, likely through the large region size used in this study as well as the fine scan employed for the line detection. It is likely caused by the changing of the particle background over time that is difficult to contain in a single model for all eRASS, as was discussed in Section 4.3.5.

The large sizes of the analyzed regions do, however, also come with definite caveats. They allow for non-insignificant variation in the physical properties of the emission components over the region area, that can not be gauged or counteracted. They can also lead to issues with the energy calibration of the 020 processing version, which can introduce further errors into the work through the attempt to counteract these issues by addition of a gain offset. Additionally it is a definite possibility that the final best fit that could be found in the scope of this thesis is not the true best fit and further refinement of the model would be possible in potential further studies. Further studies of the diffuse background emission in these regions would be especially intriguing with the new 030 processing version expected later this year that will include an improved energy calibration.
Caveats in the fitting process, of course, also have an influence on the line detection. While the energy range below 2 keV was deliberately excluded from the line scanning process to avoid the most prominent residuals in the fits, residuals caused by the choice of model and fit will nevertheless have an influence on the results of the line search. This could, theoretically, also be a factor in the large number of detected lines above 3σ. Especially the vapec and vnei model components, that allow a very fine tuning of individual element abundances, could also be a factor in the possible appearance of inaccurate atomic lines in the fit.
Whether the detected features actually resemble lines can also only be investigated within the bounds set by eROSITA's energy resolution. Especially in places with broader emission features, both the existence of several overlapping lines or broader features in the residuals could be possible. As the purpose of this work was to find all line features, all peaks that could be resolved by eROSITA as separate peaks were treated as individual lines. An uncertainty in this does, however, certainly remain.

As all 56 detected line features $> 3\sigma$ were accounted for through atomic lines, it was not possible in the scope of this thesis to look more closely into each individual line, or to preform an individual modeling on their shapes. For a closer look into their properties, doing so could be an intriguing follow-up study, especially considering the expected improvements with processing version 030.

Finally it can be reiterated that the decay line feature search conducted in the course of this thesis project has revealed the presence of many line features in the residuals of the fit, all of which can be associated with atomic lines and CX lines. Thus in this study no

evidence for the presence of sterile neutrino decay lines could be found.
Additionally good spectral fits for the diffuse X-ray background, that could contribute to further work in the characterization of its different components and their properties, were found.

7. Summary and Outlook

The investigation of new physics is a difficult, however, extremely important task in scientific research.
To contribute to the effort of detecting and investigating possible dark matter decay features, a search for sterile neutrino dark matter decay lines toward the Galactic bulge and halo was conducted in this work.

To this purpose eROSITA data from a semi-circular region west of the Galactic center was analyzed. The region was split into three parts, separating the disk area from the northern and southern areas. In the data of all three regions all point sources were excluded and spectra were extracted.
The spectra were modeled using the spectral model by Ponti et al. (2022). Many different model configurations were tested and the basic model was modified to find a final best fit model.
This model was then used in the next steps to scan the residuals for line features through the repeated addition and fitting of Gaussian line components to the final best fit model. Through this scan a large number of line features could be found, many of which trace the FWC model lines, pointing to small discrepancies between the FWC model and the actual instrumental and particle background in the data. The significant line detections $> 3\sigma$ were correlated with known atomic lines as well as possible CX lines.

It was found that all detected lines can be associated with known atomic lines, while also showing overlap with possible CX lines. The conclusion must thus be drawn that no sign of sterile neutrino decay lines could be found in the present survey.

As the 030 processing version for eROSITA data expected later this year includes an improved energy calibration, it is expected that the 030 data could offer further insight into the properties of the spectra and the present emission lines in possible follow-up studies.
Another instrument that is expected to have a large impact on this field of study is XRISM, which was launched recently.

In conclusion it can be said that the question of sterile neutrino dark matter and its possible decay features remains unsolved as of yet. It is, however, a fascinating possibility and we can expect a lot of interesting studies and projects in the future to investigate it further, and to - perhaps - bring us closer to a comprehensive picture of dark matter and its characteristics.

Acknowledgments

Data and Software

This work is based on data from eROSITA, the soft X-ray instrument aboard SRG, a joint Russian-German science mission supported by the Russian Space Agency (Roskosmos), in the interests of the Russian Academy of Sciences represented by its Space Research Institute (IKI), and the Deutsches Zentrum für Luft- und Raumfahrt (DLR). The SRG spacecraft was built by Lavochkin Association (NPOL) and its subcontractors, and is operated by NPOL with support from the Max Planck Institute for Extraterrestrial Physics (MPE).

The development and construction of the eROSITA X-ray instrument was led by MPE, with contributions from the Dr. Karl Remeis Observatory Bamberg & ECAP (FAU Erlangen-Nuernberg), the University of Hamburg Observatory, the Leibniz Institute for Astrophysics Potsdam (AIP), and the Institute for Astronomy and Astrophysics of the University of Tübingen, with the support of DLR and the Max Planck Society. The Argelander Institute for Astronomy of the University of Bonn and the Ludwig Maximilians Universität Munich also participated in the science preparation for eROSITA.

The eROSITA data shown here were processed using the eSASS/NRTA software system developed by the German eROSITA consortium.

This research has made use of data and/or software provided by the High Energy Astrophysics Science Archive Research Center (HEASARC), which is a service of the Astrophysics Science Division at NASA/GSFC.

This research has made use of the VizieR catalogue access tool, CDS, Strasbourg, France (DOI : 10.26093/cds/vizier). The original description of the VizieR service was published in 2000, A&AS 143, 23.

Personal Acknowledgments

I would like to sincerely thank everyone who has supported me in and during the writing of my Master's thesis, especially all the people at the Remeis observatory. My time here could not have been as great without all of you and the lovely, tight-knit community in the observatory!

First I would like to thank my thesis supervisor, Prof. Dr. Manami Sasaki for the interesting project and opportunities. Thank you for the help and support over the years, it has been great being a part of the Multiwavelength group!
I would also like to thank Dr. Jonathan Knies for his patience and for the help with all things Python and PyXspec.

Next I would also like to thank the members of the Hot Milk group of Dr. Gabriele Ponti for their suggestions and ideas concerning the spectral fitting, especially Dr. Konrad Dennerl for his assistance in looking for solutions in the fitting process, Nicola Locatelli for answering questions about the disnht model, and Michael Yeung for his help with the FWC model.

A big thank you also to my office mates Jakob, Federico, Julia, and Clarissa for the great working atmosphere in our office and all the members of the Multiwavelength group for the nice group meetings and the great community in the group.

Another big thank you also goes out to the Remeis observatory coffee machine for keeping me alive and awake over the years!

I would also like to thank my family for their support. My mother for encouraging me and believing in me all these years. My father for the gin tonic and the interesting conversations. My brother for having faith and believing in me.

I would also like to thank my best friend Anna for always standing up for me and encouraging me. We've finally finished our Master's theses, we did it!

Bibliography

Adhikari, R., Agostini, M., Ky, N. A., Araki, T., Archidiacono, M., Bahr, M., Baur, J., Behrens, J., Bezrukov, F., Dev, P. S. B., Borah, D., Boyarsky, A., de Gouvea, A., Pires, C. A. d. S., de Vega, H. J., Dias, A. G., Di Bari, P., Djurcic, Z., Dolde, K., Dorrer, H., Durero, M., Dragoun, O., Drewes, M., Drexlin, G., Düllmann, C. E., Eberhardt, K., Eliseev, S., Enss, C., Evans, N. W., Faessler, A., Filianin, P., Fischer, V., Fleischmann, A., Formaggio, J. A., Franse, J., Fraenkle, F. M., Frenk, C. S., Fuller, G., Gastaldo, L., Garzilli, A., Giunti, C., Glück, F., Goodman, M. C., Gonzalez-Garcia, M. C., Gorbunov, D., Hamann, J., Hannen, V., Hannestad, S., Hansen, S. H., Hassel, C., Heeck, J., Hofmann, F., Houdy, T., Huber, A., Iakubovskyi, D., Ianni, A., Ibarra, A., Jacobsson, R., Jeltema, T., Jochum, J., Kempf, S., Kieck, T., Korzeczek, M., Kornoukhov, V., Lachenmaier, T., Laine, M., Langacker, P., Lasserre, T., Lesgourgues, J., Lhuillier, D., Li, Y. F., Liao, W., Long, A. W., Maltoni, M., Mangano, G., Mavromatos, N. E., Menci, N., Merle, A., Mertens, S., Mirizzi, A., Monreal, B., Nozik, A., Neronov, A., Niro, V., Novikov, Y., Oberauer, L., Otten, E., Palanque-Delabrouille, N., Pallavicini, M., Pantuev, V. S., Papastergis, E., Parke, S., Pascoli, S., Pastor, S., Patwardhan, A., Pilaftsis, A., Radford, D. C., Ranitzsch, P. C.-O., Rest, O., Robinson, D. J., da Silva, P. S. R., Ruchayskiy, O., Sanchez, N. G., Sasaki, M., Saviano, N., Schneider, A., Schneider, F., Schwetz, T., Schönert, S., Scholl, S., Shankar, F., Shrock, R., Steinbrink, N., Strigari, L., Suekane, F., Suerfu, B., Takahashi, R., Van, N. T. H., Tkachev, I., Totzauer, M., Tsai, Y., Tully, C. G., Valerius, K., Valle, J. W. F., Venos, D., Viel, M., Vivier, M., Wang, M. Y., Weinheimer, C., Wendt, K., Winslow, L., Wolf, J., Wurm, M., Xing, Z., Zhou, S., and Zuber, K. (2017). A White Paper on keV Sterile Neutrino Dark Matter. *Journal of Cosmology and Astroparticle Physics*, 2017(01):025–025. editors: Drewes, M., Lasserre, T., Merle, A. and Mertens, S.

Aharonian, F. A., Akamatsu, H., Akimoto, F., Allen, S. W., Angelini, L., Arnaud, K. A., Audard, M., Awaki, H., Axelsson, M., Bamba, A., Bautz, M. W., Blandford, R. D., Bulbul, E., Brenneman, L. W., Brown, G. V., Cackett, E. M., Chernyakova, M., Chiao, M. P., Coppi, P., Costantini, E., Plaa, J. D., Herder, J.-W. D., Done, C., Dotani, T., Ebisawa, K., Eckart, M. E., Enoto, T., Ezoe, Y., Fabian, A. C., Ferrigno, C., Foster, A. R., Fujimoto, R., Fukazawa, Y., Furuzawa, A., Galeazzi, M., Gallo, L. C., Gandhi, P., Giustini, M., Goldwurm, A., Gu, L., Guainazzi, M., Haba, Y., Hagino, K., Hamaguchi, K., Harrus, I., Hatsukade, I., Hayashi, K., Hayashi, T., Hayashida, K., Hiraga, J., Hornschemeier, A. E., Hoshino, A., Hughes, J. P., Ichinohe, Y., Iizuka, R., Inoue, H., Inoue, S., Inoue, Y., Ishibashi, K., Ishida, M., Ishikawa, K., Ishisaki, Y., Itoh, M., Iwai, M., Iyomoto, N., Kaastra, J. S., Kallman, T., Kamae, T., Kara, E., Kataoka, J.,

Katsuda, S., Katsuta, J., Kawaharada, M., Kawai, N., Kelley, R. L., Khangulyan, D., Kilbourne, C. A., King, A. L., Kitaguchi, T., Kitamoto, S., Kitayama, T., Kohmura, T., Kokubun, M., Koyama, S., Koyama, K., Kretschmar, P., Krimm, H. A., Kubota, A., Kunieda, H., Laurent, P., Lebrun, F., Lee, S.-H., Leutenegger, M. A., Limousin, O., Loewenstein, M., Long, K. S., Lumb, D. H., Madejski, G. M., Maeda, Y., Maier, D., Makishima, K., Markevitch, M., Matsumoto, H., Matsushita, K., McCammon, D., McNamara, B. R., Mehdipour, M., Miller, E. D., Miller, J. M., Mineshige, S., Mitsuda, K., Mitsuishi, I., Miyazawa, T., Mizuno, T., Mori, H., Mori, K., Moseley, H., Mukai, K., Murakami, H., Murakami, T., Mushotzky, R. F., Nakagawa, T., Nakajima, H., Nakamori, T., Nakano, T., Nakashima, S., Nakazawa, K., Nobukawa, K., Nobukawa, M., Noda, H., Nomachi, M., Dell, S. L. O., Odaka, H., Ohashi, T., Ohno, M., Okajima, T., Ota, N., Ozaki, M., Paerels, F., Paltani, S., Parmar, A., Petre, R., Pinto, C., Pohl, M., Porter, F. S., Pottschmidt, K., Ramsey, B. D., Reynolds, C. S., Russell, H. R., Safi-Harb, S., Saito, S., Sakai, K., Sameshima, H., Sasaki, T., Sato, G., Sato, K., Sato, R., Sawada, M., Schartel, N., Serlemitsos, P. J., Seta, H., Shidatsu, M., Simionescu, A., Smith, R. K., Soong, Y., Stawarz, L., Sugawara, Y., Sugita, S., Szymkowiak, A. E., Tajima, H., Takahashi, H., Takahashi, T., Takeda, S., Takei, Y., Tamagawa, T., Tamura, K., Tamura, T., Tanaka, T., Tanaka, Y., Tanaka, Y., Tashiro, M., Tawara, Y., Terada, Y., Terashima, Y., Tombesi, F., Tomida, H., Tsuboi, Y., Tsujimoto, M., Tsunemi, H., Tsuru, T., Uchida, H., Uchiyama, H., Uchiyama, Y., Ueda, S., Ueda, Y., Ueno, S., Uno, S., Urry, C. M., Ursino, E., Vries, C. P. D., Watanabe, S., Werner, N., Wik, D. R., Wilkins, D. R., Williams, B. J., Yamada, S., Yamaguchi, H., Yamaoka, K., Yamasaki, N. Y., Yamauchi, M., Yamauchi, S., Yaqoob, T., Yatsu, Y., Yonetoku, D., Yoshida, A., Zhuravleva, I., Zoghbi, A., and Collaboration, H. (2017). Hitomi Constraints on the 3.5 keV Line in the Perseus Galaxy Cluster. *The Astrophysical Journal*, 837(1):L15.

Arnaud, K., Gordon, C., Dorman, B., and Rutkowski, K. (2023). Xspec, An X-Ray Spectral Fitting Package, Users' Guide for version 12.13.1. HEASARC, Astrophysics Science Division, NASA/GSFC, Greenbelt, MD 20771
https://heasarc.gsfc.nasa.gov/xanadu/xspec/XspecManual.pdf,
last accessed on 5 September 2023.

Asaka, T., Blanchet, S., and Shaposhnikov, M. (2005). The νMSM, dark matter and neutrino masses. *Physics Letters B*, 631(4):151–156.

Asaka, T., Shaposhnikov, M., and Laine, M. (2007). Lightest sterile neutrino abundance within the νMSM. *Journal of High Energy Physics*, 2007(01):091.

Astropy Collaboration, Price-Whelan, A. M., Lim, P. L., Earl, N., Starkman, N., Bradley, L., Shupe, D. L., Patil, A. A., Corrales, L., Brasseur, C. E., Nöthe, M., Donath, A., Tollerud, E., Morris, B. M., Ginsburg, A., Vaher, E., Weaver, B. A., Tocknell, J., Jamieson, W., van Kerkwijk, M. H., Robitaille, T. P., Merry, B., Bachetti, M., Günther, H. M., Aldcroft, T. L., Alvarado-Montes, J. A., Archibald, A. M., Bódi, A., Bapat, S., Barentsen, G., Bazán, J., Biswas, M., Boquien, M., Burke, D. J., Cara, D., Cara,

M., Conroy, K. E., Conseil, S., Craig, M. W., Cross, R. M., Cruz, K. L., D'Eugenio, F., Dencheva, N., Devillepoix, H. A. R., Dietrich, J. P., Eigenbrot, A. D., Erben, T., Ferreira, L., Foreman-Mackey, D., Fox, R., Freij, N., Garg, S., Geda, R., Glattly, L., Gondhalekar, Y., Gordon, K. D., Grant, D., Greenfield, P., Groener, A. M., Guest, S., Gurovich, S., Handberg, R., Hart, A., Hatfield-Dodds, Z., Homeier, D., Hosseinzadeh, G., Jenness, T., Jones, C. K., Joseph, P., Kalmbach, J. B., Karamehmetoglu, E., Kałuszyński, M., Kelley, M. S. P., Kern, N., Kerzendorf, W. E., Koch, E. W., Kulumani, S., Lee, A., Ly, C., Ma, Z., MacBride, C., Maljaars, J. M., Muna, D., Murphy, N. A., Norman, H., O'Steen, R., Oman, K. A., Pacifici, C., Pascual, S., Pascual-Granado, J., Patil, R. R., Perren, G. I., Pickering, T. E., Rastogi, T., Roulston, B. R., Ryan, D. F., Rykoff, E. S., Sabater, J., Sakurikar, P., Salgado, J., Sanghi, A., Saunders, N., Savchenko, V., Schwardt, L., Seifert-Eckert, M., Shih, A. Y., Jain, A. S., Shukla, G., Sick, J., Simpson, C., Singanamalla, S., Singer, L. P., Singhal, J., Sinha, M., Sipőcz, B. M., Spitler, L. R., Stansby, D., Streicher, O., Šumak, J., Swinbank, J. D., Taranu, D. S., Tewary, N., Tremblay, G. R., de Val-Borro, M., Van Kooten, S. J., Vasović, Z., Verma, S., de Miranda Cardoso, J. V., Williams, P. K. G., Wilson, T. J., Winkel, B., Wood-Vasey, W. M., Xue, R., Yoachim, P., Zhang, C., Zonca, A., and Astropy Project Contributors (2022). The Astropy Project: Sustaining and Growing a Community-oriented Open-source Project and the Latest Major Release (v5.0) of the Core Package. *The Astrophysical Journal*, 935(2):167.

Borkowski, K. J., Lyerly, W. J., and Reynolds, S. P. (2001). Supernova Remnants in the Sedov Expansion Phase: Thermal X-Ray Emission. *The Astrophysical Journal*, 548(2):820–835.

Boyarsky, A., Drewes, M., Lasserre, T., Mertens, S., and Ruchayskiy, O. (2019). Sterile Neutrino Dark Matter. *Progress in Particle and Nuclear Physics*, 104:1–45. arXiv:1807.07938 [astro-ph, physics:hep-ex, physics:hep-ph].

Boyarsky, A., Franse, J., Iakubovskyi, D., and Ruchayskiy, O. (2015). Checking the Dark Matter Origin of a 3.53 keV Line with the Milky Way Center. *Physical Review Letters*, 115(16):161301.

Boyarsky, A., Ruchayskiy, O., Iakubovskyi, D., and Franse, J. (2014). Unidentified Line in X-Ray Spectra of the Andromeda Galaxy and Perseus Galaxy Cluster. *Physical Review Letters*, 113(25):251301.

Boyarsky, A., Ruchayskiy, O., and Shaposhnikov, M. (2009). The Role of Sterile Neutrinos in Cosmology and Astrophysics. *Annual Review of Nuclear and Particle Science*, 59(1):191–214.

Brunner, H., Boller, T., Coutinho, D., Dauser, T., Dennerl, K., Dwelly, T., Freyberg, M., Fürmetz, M., Georgakakis, A., Grossberger, C., Kreykenbohm, I., Lamer, G., Meidinger, N., Müller, S., Predehl, P., Robrade, J., Sanders, J., and Wilms, J. (2018). eROSITA ground operations. In den Herder, J.-W. A., Nikzad, S., and Nakazawa, K., editors,

Space Telescopes and Instrumentation 2018: Ultraviolet to Gamma Ray, volume 10699, page 106995G. International Society for Optics and Photonics, SPIE.

Bulbul, E., Markevitch, M., Foster, A., Smith, R. K., Loewenstein, M., and Randall, S. W. (2014). DETECTION OF AN UNIDENTIFIED EMISSION LINE IN THE STACKED X-RAY SPECTRUM OF GALAXY CLUSTERS. *The Astrophysical Journal*, 789(1):13.

Davis, M., Huchra, J., Latham, D. W., and Tonry, J. (1982). A survey of galaxy redshifts. II. The large scale space distribution. *The Astrophysical Journal*, 253:423–445.

Demtröder, W. (2017). *Experimentalphysik 4, Kern-, Teilchen- und Astrophysik*. Springer-Verlag GmbH Deutschland, Berlin, Heidelberg, 5th edition.

Dennerl, K., Andritschke, R., Bräuninger, H., Burkert, W., Burwitz, V., Emberger, V., Freyberg, M., Friedrich, P., Gaida, R., Granato, S., Hartner, G., Kienlin, A. v., Meidinger, N., Menz, B., and Predehl, P. (2020). The calibration of eROSITA on SRG. In *Space Telescopes and Instrumentation 2020: Ultraviolet to Gamma Ray*, volume 11444, page 777–796. SPIE.

Dessert, C., Ning, O., Rodd, N. L., and Safdi, B. R. (2023). Limits from the grave: resurrecting Hitomi for decaying dark matter and forecasting leading sensitivity for XRISM. *arXiv e-prints*, arXiv:2305.17160.

Fließbach, T. (2016). *Allgemeine Relativitätstheorie*. Springer Spektrum, Berlin, Heidelberg, 7th edition.

Foster, A. (2023). AtomDB Charge Exchange Model v2.0 (ACX2). https://acx2.readthedocs.io/_/downloads/en/latest/pdf/, last accessed on 29 August 2023.

Foster, A., Cui, X., Dupont, M., Smith, R., and Brickhouse, N. (2020). Modelling Non-Maxwellian Plasmas with AtomDB. In *American Astronomical Society Meeting Abstracts #235*, volume 235 of *American Astronomical Society Meeting Abstracts*, page 180.01.

Foster, J. W., Kongsore, M., Dessert, C., Park, Y., Rodd, N. L., Cranmer, K., and Safdi, B. R. (2021). Deep Search for Decaying Dark Matter with XMM-Newton Blank-Sky Observations. *Physical Review Letters*, 127(5):051101.

Franse, J., Bulbul, E., Foster, A., Boyarsky, A., Markevitch, M., Bautz, M., Iakubovskyi, D., Loewenstein, M., McDonald, M., Miller, E., Randall, S. W., Ruchayskiy, O., and Smith, R. K. (2016). RADIAL PROFILE OF THE 3.5 keV LINE OUT TO R200 IN THE PERSEUS CLUSTER. *The Astrophysical Journal*, 829(2):124.

Frenk, C. S. and White, S. D. M. (2012). Dark matter and cosmic structure. *Annalen der Physik*, 524(9-10):507–534.

Freyberg, M., Perinati, E., Pacaud, F., Eraerds, T., Churazov, E., Dennerl, K., Predehl, P., Merloni, A., Meidinger, N., Bulbul, E., Friedrich, S., Gilfanov, M., Tenzer, C., Pommranz, C., Eckert, D., Schmitt, J., Brusa, M., and Santangelo, A. (2020). SRG/eROSITA in-flight background at L2. In *Space Telescopes and Instrumentation 2020: Ultraviolet to Gamma Ray*, volume 11444, page 114441O. SPIE.

Giacconi, R., Gursky, H., Paolini, F. R., and Rossi, B. B. (1962). Evidence for x Rays From Sources Outside the Solar System. *Physical Review Letters*, 9(11):439–443.

Gordon, C. and Arnaud, K. (2022). PyXspec Documentation, Release 2.1.1. HEASARC Software Development, Astrophysics Science Division,
Code 660.1, NASA/GSFC, Greenbelt MD 20771
https://heasarc.gsfc.nasa.gov/xanadu/xspec/python/PyXspec.pdf,
last accessed on 16 July 2023.

Gu, L., Kaastra, J., Raassen, A. J. J., Mullen, P. D., Cumbee, R. S., Lyons, D., and Stancil, P. C. (2015). A novel scenario for the possible X-ray line feature at ∼3.5 keV: Charge exchange with bare sulfur ions. *Astronomy & Astrophysics*, 584:L11.

Harris, C. R., Millman, K. J., van der Walt, S. J., Gommers, R., Virtanen, P., Cournapeau, D., Wieser, E., Taylor, J., Berg, S., Smith, N. J., Kern, R., Picus, M., Hoyer, S., van Kerkwijk, M. H., Brett, M., Haldane, A., del Río, J. F., Wiebe, M., Peterson, P., Gérard-Marchant, P., Sheppard, K., Reddy, T., Weckesser, W., Abbasi, H., Gohlke, C., and Oliphant, T. E. (2020). Array programming with NumPy. *Nature*, 585(7825):357–362.

HI4PI Collaboration, Ben Bekhti, N., Flöer, L., Keller, R., Kerp, J., Lenz, D., Winkel, B., Bailin, J., Calabretta, M. R., Dedes, L., Ford, H. A., Gibson, B. K., Haud, U., Janowiecki, S., Kalberla, P. M. W., Lockman, F. J., McClure-Griffiths, N. M., Murphy, T., Nakanishi, H., Pisano, D. J., and Staveley-Smith, L. (2016). HI4PI: A full-sky H I survey based on EBHIS and GASS. *Astronomy & Astrophysics*, 594:A116.

Hofmann, F. and Wegg, C. (2019). 7.1 keV sterile neutrino dark matter constraints from a deep Chandra X-ray observation of the Galactic bulge Limiting Window. *Astronomy & Astrophysics*, 625:L7.

Hunter, J. D. (2007). Matplotlib: A 2D Graphics Environment. *Computing in Science and Engineering*, 9(3):90–95.

Joye, W. A. and Mandel, E. (2003). New Features of SAOImage DS9. In Payne, H. E., Jedrzejewski, R. I., and Hook, R. N., editors, *Astronomical Data Analysis Software and Systems XII*, volume 295 of *Astronomical Society of the Pacific Conference Series*, page 489.

Kitayama, T., Bautz, M., Markevitch, M., Matsushita, K., Allen, S., Kawaharada, M., McNamara, B., Ota, N., Akamatsu, H., de Plaa, J., Galeazzi, M., Madejski, G., Main, R., Miller, E., Nakazawa, K., Russell, H., Sato, K., Sekiya, N., Simionescu, A., Tamura,

T., Uchida, Y., Ursino, E., Werner, N., Zhuravleva, I., and ZuHone, J. (2014). ASTRO-H White Paper - Clusters of Galaxies and Related Science. *arXiv e-prints*, arXiv:1412.1176.

Kuntz, K. D. (2019). Solar wind charge exchange: an astrophysical nuisance. *The Astronomy and Astrophysics Review*, 27(1):1.

Liu, W., Chiao, M., Collier, M. R., Cravens, T., Galeazzi, M., Koutroumpa, D., Kuntz, K. D., Lallement, R., Lepri, S. T., McCammon, D., Morgan, K., Porter, F. S., Snowden, S. L., Thomas, N. E., Uprety, Y., Ursino, E., and Walsh, B. M. (2017). THE STRUCTURE OF THE LOCAL HOT BUBBLE. *The Astrophysical Journal*, 834(1):33.

Locatelli, N., Ponti, G., and Bianchi, S. (2022). disnht: Modeling X-ray absorption from distributed column densities. *Astronomy & Astrophysics*, 659:A118.

Loewenstein, M. and Kusenko, A. (2010). DARK MATTER SEARCH USING CHANDRA OBSERVATIONS OF WILLMAN 1 AND A SPECTRAL FEATURE CONSISTENT WITH A DECAY LINE OF A 5 keV STERILE NEUTRINO. *The Astrophysical Journal*, 714(1):652–662.

Malyshev, D., Neronov, A., and Eckert, D. (2014). Constraints on 3.55 keV line emission from stacked observations of dwarf spheroidal galaxies. *Physical Review D*, 90(10):103506.

Max Planck Institute for Extraterrestrial Physics (2019). Pressemappe, Bilder und Filme für den Start des eROSITA-Teleskops.
https://www.mpe.mpg.de/7310250/presskit-launch2019,
last accessed on 14 August 2023.

Max Planck Institute for Extraterrestrial Physics (2020). Our deepest view of the X-ray sky.
https://www.mpe.mpg.de/7461761/news20200619,
last accessed on 18 July 2023.

Max Planck Institute for Extraterrestrial Physics (2021). eROSITA-DE: Early Data Release site, eROSITA light leak: telescope modules TM5 and TM7.
https://erosita.mpe.mpg.de/edr/eROSITAIssues/lightleak.html,
last accessed on 14 August 2023.

Merloni, A., Predehl, P., Becker, W., Böhringer, H., Boller, T., Brunner, H., Brusa, M., Dennerl, K., Freyberg, M., Friedrich, P., Georgakakis, A., Haberl, F., Hasinger, G., Meidinger, N., Mohr, J., Nandra, K., Rau, A., Reiprich, T. H., Robrade, J., Salvato, M., Santangelo, A., Sasaki, M., Schwope, A., Wilms, J., and German eROSITA Consortium, t. (2012). eROSITA Science Book: Mapping the Structure of the Energetic Universe. *arXiv e-prints*, arXiv:1209.3114.

Neronov, A., Malyshev, D., and Eckert, D. (2016). Decaying dark matter search with NuSTAR deep sky observations. *Physical Review D*, 94(12):123504.

Planck Collaboration, Aghanim, N., Akrami, Y., Ashdown, M., Aumont, J., Baccigalupi, C., Ballardini, M., Banday, A. J., Barreiro, R. B., Bartolo, N., Basak, S., Battye, R., Benabed, K., Bernard, J. P., Bersanelli, M., Bielewicz, P., Bock, J. J., Bond, J. R., Borrill, J., Bouchet, F. R., Boulanger, F., Bucher, M., Burigana, C., Butler, R. C., Calabrese, E., Cardoso, J. F., Carron, J., Challinor, A., Chiang, H. C., Chluba, J., Colombo, L. P. L., Combet, C., Contreras, D., Crill, B. P., Cuttaia, F., de Bernardis, P., de Zotti, G., Delabrouille, J., Delouis, J. M., Di Valentino, E., Diego, J. M., Doré, O., Douspis, M., Ducout, A., Dupac, X., Dusini, S., Efstathiou, G., Elsner, F., Enßlin, T. A., Eriksen, H. K., Fantaye, Y., Farhang, M., Fergusson, J., Fernandez-Cobos, R., Finelli, F., Forastieri, F., Frailis, M., Fraisse, A. A., Franceschi, E., Frolov, A., Galeotta, S., Galli, S., Ganga, K., Génova-Santos, R. T., Gerbino, M., Ghosh, T., González-Nuevo, J., Górski, K. M., Gratton, S., Gruppuso, A., Gudmundsson, J. E., Hamann, J., Handley, W., Hansen, F. K., Herranz, D., Hildebrandt, S. R., Hivon, E., Huang, Z., Jaffe, A. H., Jones, W. C., Karakci, A., Keihänen, E., Keskitalo, R., Kiiveri, K., Kim, J., Kisner, T. S., Knox, L., Krachmalnicoff, N., Kunz, M., Kurki-Suonio, H., Lagache, G., Lamarre, J. M., Lasenby, A., Lattanzi, M., Lawrence, C. R., Le Jeune, M., Lemos, P., Lesgourgues, J., Levrier, F., Lewis, A., Liguori, M., Lilje, P. B., Lilley, M., Lindholm, V., López-Caniego, M., Lubin, P. M., Ma, Y. Z., Macías-Pérez, J. F., Maggio, G., Maino, D., Mandolesi, N., Mangilli, A., Marcos-Caballero, A., Maris, M., Martin, P. G., Martinelli, M., Martínez-González, E., Matarrese, S., Mauri, N., McEwen, J. D., Meinhold, P. R., Melchiorri, A., Mennella, A., Migliaccio, M., Millea, M., Mitra, S., Miville-Deschênes, M. A., Molinari, D., Montier, L., Morgante, G., Moss, A., Natoli, P., Nørgaard-Nielsen, H. U., Pagano, L., Paoletti, D., Partridge, B., Patanchon, G., Peiris, H. V., Perrotta, F., Pettorino, V., Piacentini, F., Polastri, L., Polenta, G., Puget, J. L., Rachen, J. P., Reinecke, M., Remazeilles, M., Renzi, A., Rocha, G., Rosset, C., Roudier, G., Rubiño-Martín, J. A., Ruiz-Granados, B., Salvati, L., Sandri, M., Savelainen, M., Scott, D., Shellard, E. P. S., Sirignano, C., Sirri, G., Spencer, L. D., Sunyaev, R., Suur-Uski, A. S., Tauber, J. A., Tavagnacco, D., Tenti, M., Toffolatti, L., Tomasi, M., Trombetti, T., Valenziano, L., Valiviita, J., Van Tent, B., Vibert, L., Vielva, P., Villa, F., Vittorio, N., Wandelt, B. D., Wehus, I. K., White, M., White, S. D. M., Zacchei, A., and Zonca, A. (2020). Planck 2018 results. VI. Cosmological parameters. *Astronomy & Astrophysics*, 641:A6.

Ponti, G., Zheng, X., Locatelli, N., Bianchi, S., Zhang, Y., Anastasopoulou, K., Comparat, J., Dennerl, K., Freyberg, M., Haberl, F., Merloni, A., Reiprich, T. H., Salvato, M., Sanders, J., Sasaki, M., Strong, A., and Yeung, M. C. H. (2022). Abundance and temperature of the outer hot circum-Galactic medium: The SRG/eROSITA view of the soft X-ray background in the eFEDS field. *arXiv e-prints*, arXiv:2210.03133.

Povh, B., Rith, K., Scholz, C., Zetsche, F., and Rodejohann, W. (2014). *Teilchen und Kerne*. Springer Spektrum Berlin, Heidelberg, 9th edition.

Predehl, P., Andritschke, R., Arefiev, V., Babyshkin, V., Batanov, O., Becker, W., Böhringer, H., Bogomolov, A., Boller, T., Borm, K., Bornemann, W., Bräuninger, H., Brüggen, M., Brunner, H., Brusa, M., Bulbul, E., Buntov, M., Burwitz, V., Burkert, W., Clerc, N., Churazov, E., Coutinho, D., Dauser, T., Dennerl, K., Doroshenko, V., Eder, J., Emberger, V., Eraerds, T., Finoguenov, A., Freyberg, M., Friedrich, P., Friedrich, S., Fürmetz, M., Georgakakis, A., Gilfanov, M., Granato, S., Grossberger, C., Gueguen, A., Gureev, P., Haberl, F., Hälker, O., Hartner, G., Hasinger, G., Huber, H., Ji, L., Kienlin, A. v., Kink, W., Korotkov, F., Kreykenbohm, I., Lamer, G., Lomakin, I., Lapshov, I., Liu, T., Maitra, C., Meidinger, N., Menz, B., Merloni, A., Mernik, T., Mican, B., Mohr, J., Müller, S., Nandra, K., Nazarov, V., Pacaud, F., Pavlinsky, M., Perinati, E., Pfeffermann, E., Pietschner, D., Ramos-Ceja, M. E., Rau, A., Reiffers, J., Reiprich, T. H., Robrade, J., Salvato, M., Sanders, J., Santangelo, A., Sasaki, M., Scheuerle, H., Schmid, C., Schmitt, J., Schwope, A., Shirshakov, A., Steinmetz, M., Stewart, I., Strüder, L., Sunyaev, R., Tenzer, C., Tiedemann, L., Trümper, J., Voron, V., Weber, P., Wilms, J., and Yaroshenko, V. (2021). The eROSITA X-ray telescope on SRG. *Astronomy & Astrophysics*, 647:A1.

Sasaki, M., Ponti, G., and Mackey, J. (2022). Diffuse Hot Plasma in the Interstellar Medium and Galactic Outflows. *arXiv e-prints*, arXiv:2207.01263.

Schwartz, D. A. (2011). Optics. In Arnaud, K., Smith, R., and Siemiginowska, A., editors, *Handbook of X-ray Astronomy*, Cambridge Observing Handbooks for Research Astronomers, page 6–22. Cambridge University Press.

SDSS and Blanton, M. (2014). SDSS, Science results. https://www.sdss4.org/wp-content/uploads/2014/06/orangepie.jpg, last accessed on 04th August 2023.

Seward, F. D. and Charles, P. A. (2010). *Exploring the X-ray Universe*. Cambridge University Press, 2nd edition.

Shah, C., Dobrodey, S., Bernitt, S., Steinbrügge, R., López-Urrutia, J. R. C., Gu, L., and Kaastra, J. (2016). LABORATORY MEASUREMENTS COMPELLINGLY SUPPORT A CHARGE-EXCHANGE MECHANISM FOR THE "DARK MATTER" ∼3.5 keV X-Ray LINE. *The Astrophysical Journal*, 833(1):52.

Sicilian, D., Cappelluti, N., Bulbul, E., Civano, F., Moscetti, M., and Reynolds, C. S. (2020). Probing the Milky Way's Dark Matter Halo for the 3.5 keV Line. *The Astrophysical Journal*, 905(2):146.

Sicilian, D., Lopez, D., Moscetti, M., Bulbul, E., and Cappelluti, N. (2022). Constraining Sterile Neutrino Dark Matter in the Milky Way Halo with Swift-XRT. *The Astrophysical Journal*, 941(1):2.

Smith, R., Foster, A., and Brickhouse, N. (2012). Approximating the X-ray spectrum emitted from astrophysical charge exchange. *Astronomische Nachrichten*, 333(4):301–304.

Smith, R. K., Brickhouse, N. S., Liedahl, D. A., and Raymond, J. C. (2001). Collisional Plasma Models with APEC/APED: Emission-Line Diagnostics of Hydrogen-like and Helium-like Ions. *The Astrophysical Journal*, 556(2):L91–L95.

Smith, R. K., Foster, A., Brickhouse, N. S., Stancil, P. C., Cumbee, R., Mullen, P. D., and AtomDB Team (2018). AtomDB Progress Report: Atomic data and new models for X-ray spectroscopy. In *American Astronomical Society Meeting Abstracts #232*, volume 232 of *American Astronomical Society Meeting Abstracts*, page 217.02.

Speckhard, E. G., Ng, K. C., Beacom, J. F., and Laha, R. (2016). Dark Matter Velocity Spectroscopy. *Physical Review Letters*, 116(3):031301.

The SciPy community (2023a). scipy.stats.chi2. https://docs.scipy.org/doc/scipy/reference/generated/scipy.stats.chi2.html, last accessed on 23 August 2023.

The SciPy community (2023b). scipy.stats.norm. https://docs.scipy.org/doc/scipy/reference/generated/scipy.stats.norm.html, last accessed on 23 August 2023.

Thomson, M. (2013). *Modern Particle Physics*. Cambridge University Press.

Tremaine, S. and Gunn, J. E. (1979). Dynamical Role of Light Neutral Leptons in Cosmology. *Physical Review Letters*, 42(6):407–410.

Ueda, M., Sugiyama, H., Kobayashi, S. B., Fukushima, K., Yamasaki, N. Y., Sato, K., and Matsushita, K. (2022). The soft X-ray background with Suzaku: I. Milky Way halo. *Publications of the Astronomical Society of Japan*, 74(6):1396–1414.

Urban, O., Werner, N., Allen, S. W., Simionescu, A., Kaastra, J. S., and Strigari, L. E. (2015). A Suzaku search for dark matter emission lines in the X-ray brightest galaxy clusters. *Monthly Notices of the Royal Astronomical Society*, 451(3):2447–2461.

Virtanen, P., Gommers, R., Oliphant, T. E., Haberland, M., Reddy, T., Cournapeau, D., Burovski, E., Peterson, P., Weckesser, W., Bright, J., van der Walt, S. J., Brett, M., Wilson, J., Millman, K. J., Mayorov, N., Nelson, A. R. J., Jones, E., Kern, R., Larson, E., Carey, C. J., Polat, İ., Feng, Y., Moore, E. W., VanderPlas, J., Laxalde, D., Perktold, J., Cimrman, R., Henriksen, I., Quintero, E. A., Harris, C. R., Archibald, A. M., Ribeiro, A. H., Pedregosa, F., van Mulbregt, P., and SciPy 1. 0 Contributors (2020). SciPy 1.0: fundamental algorithms for scientific computing in Python. *Nature Methods*, 17:261–272.

Wall, J. V. and Jenkins, C. R. (2012). *Practical Statistics for Astronomers*. Cambridge Observing Handbooks for Research Astronomers. Cambridge University Press, 2nd edition.

Wilms, J., Allen, A., and McCray, R. (2000). On the Absorption of X-Rays in the Interstellar Medium. *The Astrophysical Journal*, 542(2):914–924.

XRISM Science Team (2020). Science with the X-ray Imaging and Spectroscopy Mission (XRISM). *arXiv e-prints*, arXiv:2003.04962.

Yeung, M. C. H., Freyberg, M. J., Ponti, G., Dennerl, K., Sasaki, M., and Strong, A. (2023). SRG/eROSITA X-ray shadowing study of giant molecular clouds. *arXiv e-prints*, arXiv:2306.05858.

Zwicky, F. (1933). Die Rotverschiebung von extragalaktischen Nebeln. *Helvetica Physica Acta*, 6:110–127.

A. Appendix

A.1. List of sky tiles used in the analysis

238105 236108 239108 237111 241111 244111 247111 235114 238114 242114 245114 248114
251114 235117 238117 242117 245117 248117 252117 255117 235120 238120 242120 245120
249120 252120 255120 259120 262120 235123 238123 242123 245123 249123 252123 256123
259123 263123 266123 235126 238126 242126 245126 249126 253126 256126 260126 264126
267126 271126 275126 233129 237129 241129 244129 248129 252129 256129 260129 263129
267129 271129 275129 279129 282129 235132 239132 243132 247132 251132 255132 259132
263132 267132 271132 275132 279132 283132 287132 291132 295132 238135 242135 246135
250135 254135 259135 263135 267135 271135 275135 279135 283135 288135 292135 296135
236138 241138 245138 249138 254138 258138 262138 267138 271138 275138 280138 284138
288138 293138 242141 247141 252141 256141 261141 265141 270141 275141 279141 284141
288141 293141 244144 249144 254144 259144 264144 269144 274144 279144 284144 288144
251147 257147 262147 267147 273147 278147

A.2. Table of exact area results for each region and eRASS

	north	disk	south
eRASS1	388.6726	506.3670	282.8585
eRASS2	389.5917	504.4983	283.0662
eRASS3	389.8535	506.6979	283.0808
eRASS4	387.5580	505.1626	283.3424

Table A.1.: Exact areas of all regions for each eRASS in deg×deg

A.3. Final fit parameters and plots

For more information on the parameters of the model components and their properties, see Arnaud et al. (2023).
The first constant factor (const1/factor1) in the final spectral model was fit individually for each TM. In the following tables its value for TM1 is listed, for which the factor was frozen to a value of 1.0.

A.3.1. Northern region

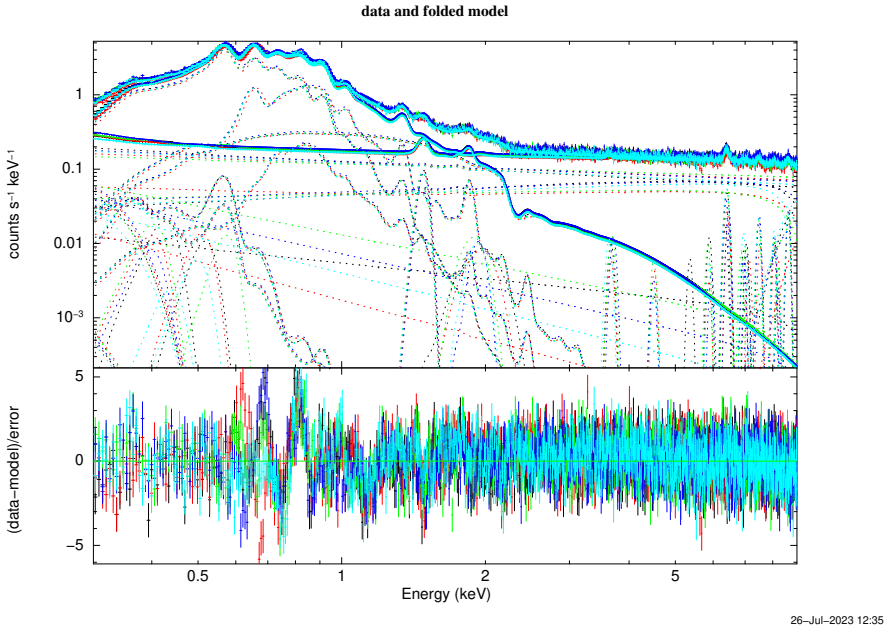

Figure A.1.: Final fit on the northern eRASS2 data

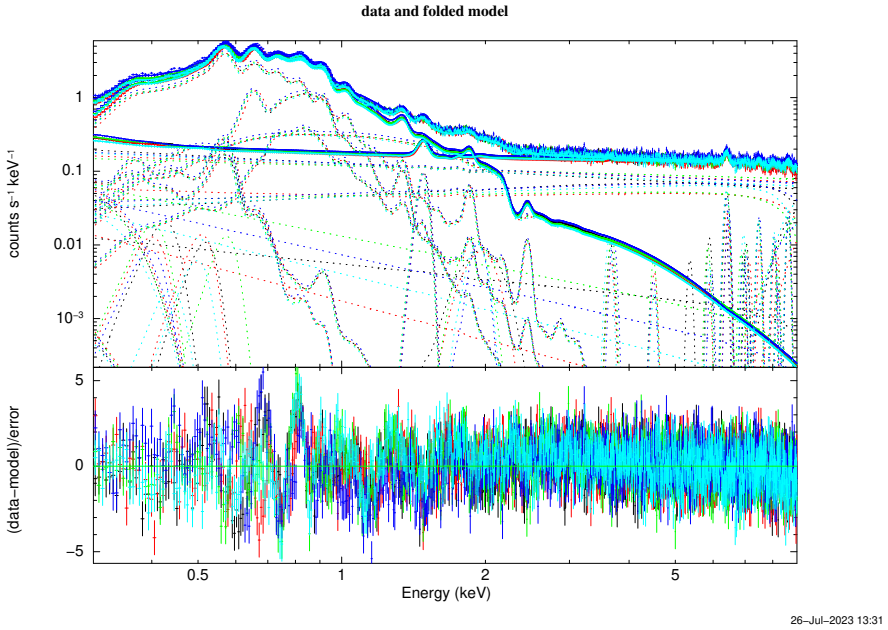

Figure A.2.: Final fit on the northern eRASS3 data

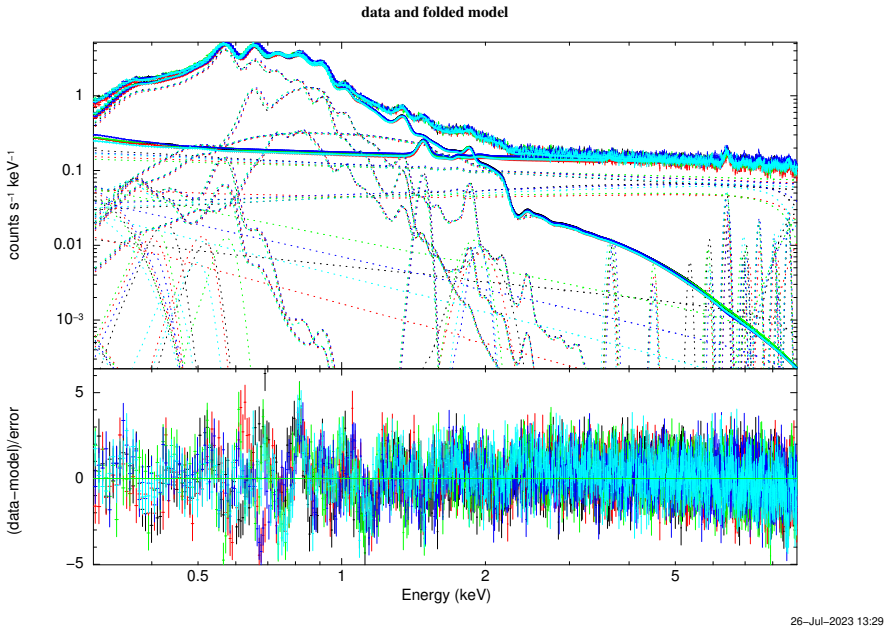

Figure A.3.: Final fit on the northern eRASS4 data

Model component	parameter	best fit value
const1	factor1	1.00
const2	factor2	1.40e+06
SWCX: acx2	temperature	1.28e-01
	collnpar	4.50e+02
	collntype	2
	acxmodel	8
	recombtype	1
	Hefrac	9.00e-02
	abund	1.00
	redshift	0.00
	norm	$4.19\text{e-}05^{+5.65\text{e}-06}_{-3.24\text{e}-06}$
LHB: apec	kT	$9.00\text{e-}02^{+5.40\text{e}-03}_{-9.00\text{e}-02}$
	Abundanc	1.00
	Redshift	0.00
	norm	$1.87\text{e-}07^{+2.01\text{e}-08}_{-1.87\text{e}-07}$
CGM: vapec	kT	$1.88\text{e-}01^{+1.18\text{e}-03}_{-1.18\text{e}-03}$
	He	8.00e-02
	C	8.00e-02
	N	8.00e-02
	O	8.00e-02
	Ne	$1.06\text{e-}01^{+5.28\text{e}-03}_{-7.39\text{e}-03}$
	Mg	$3.00\text{e-}01^{+0.00}_{-3.77\text{e}-02}$
	Al	8.00e-02
	Si	8.00e-02
	S	8.00e-02
	Ar	8.00e-02
	Ca	8.00e-02
	Fe	$3.00\text{e-}01^{+0.00}_{-1.88\text{e}-03}$
	Ni	8.00e-02
	Redshift	0.00
	norm	$7.12\text{e-}05^{+8.38\text{e}-07}_{-2.11\text{e}-06}$
Cor: apec	kT	$6.83\text{e-}01^{+8.45\text{e}-03}_{-2.22\text{e}-02}$
	Abundanc	1.00
	Redshift	0.00
	norm	$3.81\text{e-}07^{+4.25\text{e}-08}_{-1.19\text{e}-07}$
CXB: powerlaw	PhoIndex	1.46
	norm	$7.89\text{e-}07^{+8.69\text{e}-09}_{-9.02\text{e}-09}$
vnei	kT	$8.12\text{e-}01^{+4.06\text{e}-02}_{-2.44\text{e}-02}$
	H	1.00
	He	1.00
	C	1.00

Continued

	N	1.00
	O	$7.72\text{e-}01^{+7.01\text{e}-09}_{-7.72\text{e}-03}$
	Ne	1.00
	Mg	$6.76\text{e-}01^{+8.38\text{e}-02}_{-6.09\text{e}-02}$
	Si	$1.55^{+1.55\text{e}-01}_{-1.53\text{e}-01}$
	S	$3.97^{+1.12}_{-1.09}$
	Ar	1.00
	Ca	1.00
	Fe	1.00
	Ni	1.00
	Tau	$7.57\text{e+}10^{+4.99\text{e}+13}_{-7.56\text{e}+10}$
	Redshift	0.00
	norm	$7.12\text{e-}07^{+1.66\text{e}-08}_{-3.53\text{e}-08}$
gain offsets	TM1	-1.42e-03
	TM2	1.42e-03
	TM3	-4.14e-03
	TM4	1.43e-03
	TM6	-5.19e-03

Table A.2.: Final fit parameters for the eRASS1 fit for the northern region with 90% confidence interval errors

Model component	parameter	best fit value
const1	factor1	1.00
const2	factor2	1.40e+06
SWCX: acx2	temperature	1.28e-01
	collnpar	4.50e+02
	collntype	2
	acxmodel	8
	recombtype	1
	Hefrac	9.00e-02
	abund	1.00
	redshift	0.00
	norm	$3.04\text{e-}05^{+5.80\text{e}-06}_{-9.53\text{e}-06}$
LHB: apec	kT	$9.82\text{e-}02^{+4.91\text{e}-03}_{-9.82\text{e}-02}$
	Abundanc	1.00
	Redshift	0.00
	norm	$1.87\text{e-}07^{+2.01\text{e}-08}_{-1.87\text{e}-07}$
CGM: vapec	kT	$1.84\text{e-}01^{+1.84\text{e}-03}_{-1.84\text{e}-03}$

Continued

	He	8.00e-02
	C	8.00e-02
	N	8.00e-02
	O	$6.83\text{e-}02^{+6.83\text{e}-04}_{-6.83\text{e}-04}$
	Ne	$1.06\text{e-}01^{+3.56\text{e}-03}_{-3.32\text{e}-03}$
	Mg	$1.79\text{e-}01^{+3.70\text{e}-02}_{-3.04\text{e}-02}$
	Al	8.00e-02
	Si	8.00e-02
	S	8.00e-02
	Ar	8.00e-02
	Ca	8.00e-02
	Fe	$3.00\text{e-}01^{+0.00}_{-4.69\text{e}-03}$
	Ni	8.00e-02
	Redshift	0.00
	norm	$8.50\text{e-}05^{+2.16\text{e}-06}_{-2.11\text{e}-06}$
Cor: apec	kT	$6.89\text{e-}01^{+2.07\text{e}-02}_{-3.45\text{e}-02}$
	Abundanc	1.00
	Redshift	0.00
	norm	$2.66\text{e-}07^{+1.00\text{e}+20}_{-2.66\text{e}-07}$
CXB: powerlaw	PhoIndex	1.46
	norm	$7.91\text{e-}07^{+9.61\text{e}-09}_{-7.60\text{e}-09}$
vnei	kT	$7.69\text{e-}01^{+3.84\text{e}-02}_{-1.54\text{e}-02}$
	H	1.00
	He	1.00
	C	1.00
	N	1.00
	O	1.00
	Ne	1.00
	Mg	1.00
	Si	$1.51^{+1.42\text{e}-01}_{-1.40\text{e}-01}$
	S	1.00
	Ar	1.00
	Ca	1.00
	Fe	1.00
	Ni	1.00
	Tau	$9.00\text{e}{+10}^{+1.23\text{e}+04}_{-6.02\text{e}+09}$
	Redshift	0.00
	norm	$7.51\text{e-}07^{+5.29\text{e}-09}_{-7.95\text{e}-09}$
gain offsets	TM1	-3.56e-03
	TM2	2.11e-03
	TM3	-4.25e-03

Continued

	TM4	1.95e-04
	TM6	-4.34e-03

Table A.3.: Final fit parameters for the eRASS2 fit for the northern region with 90% confidence interval errors

Model component	parameter	best fit value
const1	factor1	1.00
const2	factor2	1.40e+06
SWCX: acx2	temperature	1.28e-01
	collnpar	4.50e+02
	collntype	2
	acxmodel	8
	recombtype	1
	Hefrac	9.00e-02
	abund	1.00
	redshift	0.00
	norm	$1.12\text{e-}04^{+7.54\text{e}-06}_{-1.67\text{e}-06}$
LHB: apec	kT	$1.20\text{e-}01^{+0.00}_{-3.00\text{e}-02}$
	Abundanc	1.00
	Redshift	0.00
	norm	$2.96\text{e-}07^{+6.77\text{e}-08}_{-1.09\text{e}-07}$
CGM: vapec	kT	$1.83\text{e-}01^{+7.42\text{e}-04}_{-9.62\text{e}-04}$
	He	8.00e-02
	C	8.00e-02
	N	8.00e-02
	O	$6.43\text{e-}02^{+9.10\text{e}-04}_{-4.83\text{e}-04}$
	Ne	$1.20\text{e-}01^{+2.70\text{e}-03}_{-1.50\text{e}-03}$
	Mg	$3.00\text{e-}01^{+0.00}_{-1.31\text{e}-02}$
	Al	8.00e-02
	Si	8.00e-02
	S	8.00e-02
	Ar	8.00e-02
	Ca	8.00e-02
	Fe	$3.00\text{e-}01^{+0.00}_{-2.60\text{e}-01}$
	Ni	8.00e-02
	Redshift	0.00
	norm	$8.97\text{e-}05^{+1.25\text{e}-06}_{-1.56\text{e}-06}$
Cor: apec	kT	$6.42\text{e-}01^{+4.50\text{e}-02}_{-3.21\text{e}-02}$

Continued

	Abundanc	1.00
	Redshift	0.00
	norm	$3.11\text{e-}07^{+4.71\text{e}-09}_{-1.96\text{e}-08}$
CXB: powerlaw	PhoIndex	1.46
	norm	$8.26\text{e-}07^{+2.76\text{e}-09}_{-1.10\text{e}-08}$
vnei	kT	$7.02\text{e-}01^{+4.21\text{e}-02}_{-1.40\text{e}-02}$
	H	1.00
	He	1.00
	C	1.00
	N	1.00
	O	$1.96^{+6.04\text{e}-01}_{-1.39\text{e}-01}$
	Ne	1.00
	Mg	$6.79\text{e-}01^{+5.37\text{e}-02}_{-6.31\text{e}-02}$
	Si	$1.59^{+1.40\text{e}-01}_{-1.49\text{e}-01}$
	S	$4.18^{+1.18}_{-1.31}$
	Ar	1.00
	Ca	1.00
	Fe	1.00
	Ni	1.00
	Tau	$1.41\text{e}+11^{+2.40\text{e}+10}_{-1.14\text{e}+10}$
	Redshift	0.00
	norm	$8.74\text{e-}07^{+3.12\text{e}-08}_{-4.38\text{e}-09}$
gain offsets	TM1	4.66e-04
	TM2	4.40e-03
	TM3	-3.48e-03
	TM4	-7.03e-04
	TM6	-3.25e-03

Table A.4.: Final fit parameters for the eRASS3 fit for the northern region with 90% confidence interval errors

Model component	parameter	best fit value
const1	factor1	1.00
const2	factor2	1.40e+06
SWCX: acx2	temperature	1.28e-01
	collnpar	4.50e+02
	collntype	2
	acxmodel	8
	recombtype	1

Continued

	Hefrac	9.00e-02
	abund	1.00
	redshift	0.00
	norm	$7.18\text{e-}05^{+4.44\text{e}-06}_{-1.12\text{e}-05}$
LHB: apec	kT	$9.27\text{e-}02^{+2.78\text{e}-03}_{-9.27\text{e}-02}$
	Abundanc	1.00
	Redshift	0.00
	norm	$3.60\text{e-}07^{+3.73\text{e}-09}_{-4.39\text{e}-08}$
CGM: vapec	kT	$1.80\text{e-}01^{+1.80\text{e}-03}_{-1.80\text{e}-03}$
	He	8.00e-02
	C	8.00e-02
	N	8.00e-02
	O	$6.54\text{e-}02^{+1.96\text{e}-03}_{-1.96\text{e}-03}$
	Ne	$1.05\text{e-}01^{+6.55\text{e}-04}_{-6.48\text{e}-02}$
	Mg	$3.00\text{e-}01^{+0.00}_{-2.72\text{e}-02}$
	Al	8.00e-02
	Si	$4.00\text{e-}02^{+1.81\text{e}-02}_{-4.00\text{e}-02}$
	S	8.00e-02
	Ar	8.00e-02
	Ca	8.00e-02
	Fe	$3.00\text{e-}01^{+0.00}_{-2.81\text{e}-03}$
	Ni	8.00e-02
	Redshift	0.00
	norm	$9.04\text{e-}05^{+4.97\text{e}-08}_{-3.90\text{e}-06}$
Cor: apec	kT	$5.00\text{e-}01^{+2.50\text{e}-01}_{-0.00}$
	Abundanc	1.00
	Redshift	0.00
	norm	$3.93\text{e-}09^{+6.16\text{e}-09}_{-3.93\text{e}-09}$
CXB: powerlaw	PhoIndex	1.46
	norm	$8.32\text{e-}07^{+6.68\text{e}-09}_{-8.99\text{e}-09}$
vnei	kT	$7.33\text{e-}01^{+7.33\text{e}-03}_{-1.47\text{e}-02}$
	H	1.00
	He	1.00
	C	1.00
	N	1.00
	O	1.00
	Ne	$7.25\text{e-}01^{+1.86\text{e}-02}_{-3.19\text{e}-02}$
	Mg	$6.34\text{e-}01^{+4.52\text{e}-02}_{-3.75\text{e}-02}$
	Si	$1.35^{+1.02\text{e}-01}_{-1.12\text{e}-01}$
	S	1.00
	Ar	1.00

Continued

	Ca	1.00
	Fe	1.00
	Ni	1.00
	Tau	$1.12\text{e+}11^{+6.05\text{e+}03}_{-7.48\text{e+}09}$
	Redshift	0.00
	norm	$1.15\text{e-}06^{+1.75\text{e}-08}_{-5.78\text{e}-09}$
gain offsets	TM1	7.54e-04
	TM2	3.61e-03
	TM3	-4.01e-03
	TM4	3.16e-03
	TM6	-4.35e-03

Table A.5.: Final fit parameters for the eRASS4 fit for the northern region with 90% confidence interval errors

A.3.2. Disk region

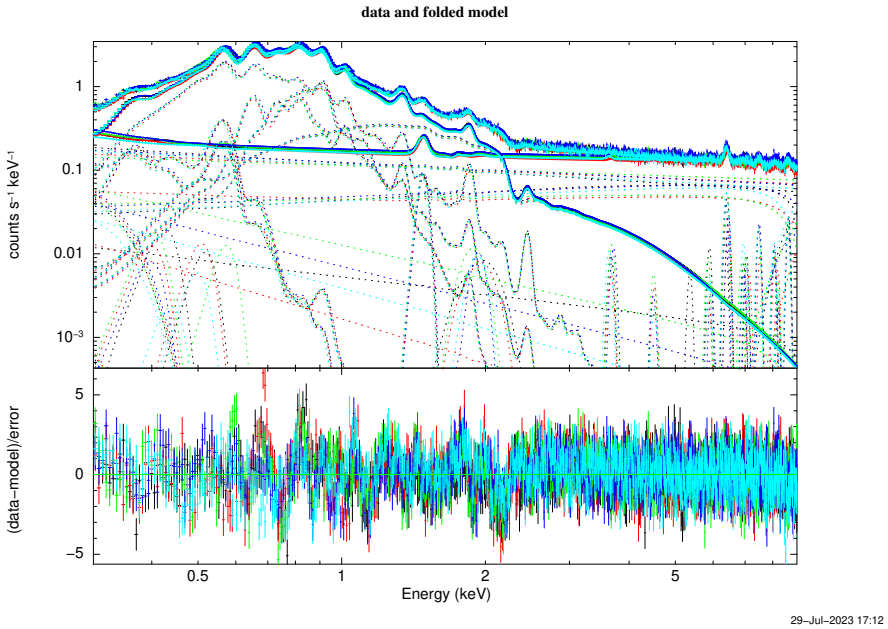

Figure A.4.: Final fit on the disk eRASS2 data

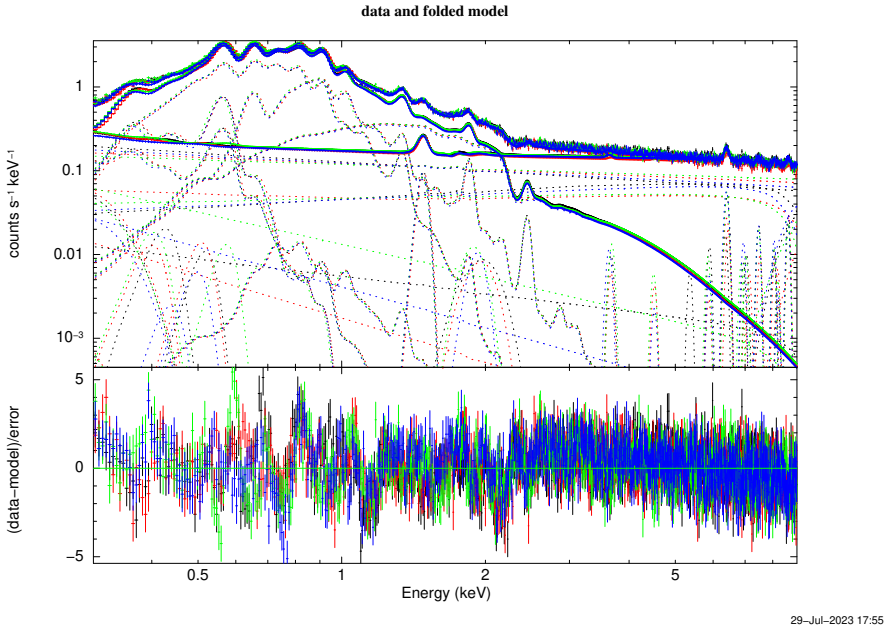

Figure A.5.: Final fit on the disk eRASS3 data

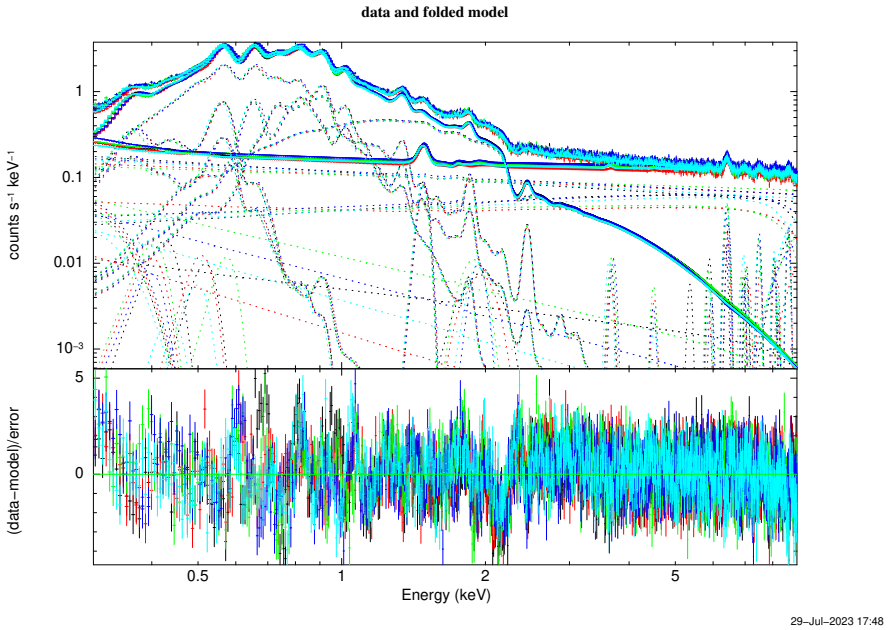

Figure A.6.: Final fit on the disk eRASS4 data

Model component	parameter	best fit value
const1	factor1	1.00
const2	factor2	1.82e+06
SWCX: acx2	temperature	1.31e-01
	collnpar	4.50e+02
	collntype	2
	acxmodel	8
	recombtype	1
	Hefrac	9.00e-02
	abund	1.00
	redshift	0.00
	norm	$1.29\text{e-}04^{+1.15\text{e}-05}_{-1.93\text{e}-06}$
LHB: apec	kT	$1.20\text{e-}01^{+4.60\text{e}-13}_{-3.00\text{e}-02}$
	Abundanc	1.00
	Redshift	0.00
	norm	$6.24\text{e-}07^{+0.00}_{-8.95\text{e}-09}$
CGM: vapec	kT	$1.68\text{e-}01^{+8.42\text{e}-03}_{-3.37\text{e}-03}$
	He	8.00e-02
	C	8.00e-02
	N	8.00e-02
	O	$4.00\text{e-}02^{+4.00\text{e}-04}_{-4.00\text{e}-02}$
	Ne	$1.13\text{e-}01^{+3.39\text{e}-03}_{-1.13\text{e}-03}$
	Mg	$1.46\text{e-}01^{+1.54\text{e}-01}_{-1.19\text{e}-03}$
	Al	8.00e-02
	Si	$3.00\text{e-}01^{+0.00}_{-4.30\text{e}-02}$
	S	$3.00\text{e-}01^{+0.00}_{-1.12\text{e}-02}$
	Ar	8.00e-02
	Ca	8.00e-02
	Fe	$3.00\text{e-}01^{+0.00}_{-1.31\text{e}-02}$
	Ni	8.00e-02
	Redshift	0.00
	norm	$4.15\text{e-}04^{+2.08\text{e}-06}_{-6.20\text{e}-06}$
Cor: apec	kT	$6.10\text{e-}01^{+6.10\text{e}-03}_{-6.10\text{e}-03}$
	Abundanc	1.00
	Redshift	0.00
	norm	$8.47\text{e-}07^{+5.70\text{e}-08}_{-2.92\text{e}-08}$
CXB: powerlaw	PhoIndex	1.46
	norm	$1.80\text{e-}06^{+9.05\text{e}-09}_{-7.96\text{e}-08}$
vnei	kT	$6.74\text{e-}01^{+2.02\text{e}-02}_{-6.06\text{e}-02}$
	H	1.00
	He	1.00
	C	1.00

Continued

	N	1.00
	O	$5.66^{+1.02}_{-1.70e-01}$
	Ne	$2.00^{+1.00e-02}_{-1.30e-01}$
	Mg	1.00
	Si	$2.23^{+1.12e-01}_{-1.56e-01}$
	S	$5.35^{+9.38e-01}_{-1.01}$
	Ar	1.00
	Ca	1.00
	Fe	1.00
	Ni	1.00
	Tau	$2.04e+11^{+4.98e+13}_{-2.04e+11}$
	Redshift	0.00
	norm	$1.68e-06^{+8.45e-09}_{-4.17e-08}$
gain offsets	TM1	-1.77e-03
	TM2	1.24e-03
	TM3	-2.41e-03
	TM4	1.25e-03
	TM6	-5.71e-03

Table A.6.: Final fit parameters for the eRASS1 fit for the disk region with 90% confidence interval errors

Model component	parameter	best fit value
const1	factor1	1.00
const2	factor2	1.82e+06
SWCX: acx2	temperature	1.31e-01
	collnpar	4.50e+02
	collntype	2
	acxmodel	8
	recombtype	1
	Hefrac	9.00e-02
	abund	1.00
	redshift	0.00
	norm	$1.49e-04^{+2.16e-06}_{-1.49e-04}$
LHB: apec	kT	$1.20e-01^{+0.00}_{-3.00e-02}$
	Abundanc	1.00
	Redshift	0.00
	norm	$6.24e-07^{+0.00}_{-1.38e-07}$
CGM: vapec	kT	$1.67e-01^{+5.23e-03}_{-1.73e-02}$

Continued

	He	8.00e-02
	C	8.00e-02
	N	8.00e-02
	O	$4.01\text{e-}02^{+4.60\text{e}-10}_{-4.01\text{e}-02}$
	Ne	$1.07\text{e-}01^{+7.06\text{e}-09}_{-2.15\text{e}-03}$
	Mg	$1.86\text{e-}01^{+1.44\text{e}-02}_{-1.55\text{e}-02}$
	Al	8.00e-02
	Si	$3.00\text{e-}01^{+0.00}_{-3.59\text{e}-02}$
	S	$3.00\text{e-}01^{+0.00}_{-9.37\text{e}-03}$
	Ar	8.00e-02
	Ca	8.00e-02
	Fe	$3.00\text{e-}01^{+1.50\text{e}-03}_{-2.57\text{e}-03}$
	Ni	8.00e-02
	Redshift	0.00
	norm	$4.02\text{e-}04^{+4.73\text{e}-06}_{-5.35\text{e}-06}$
Cor: apec	kT	$7.40\text{e-}01^{+9.60\text{e}-03}_{-3.40\text{e}-01}$
	Abundanc	1.00
	Redshift	0.00
	norm	$1.31\text{e-}06^{+3.31\text{e}-08}_{-6.54\text{e}-09}$
CXB: powerlaw	PhoIndex	1.46
	norm	$1.87\text{e-}06^{+4.00\text{e}-09}_{-3.58\text{e}-08}$
vnei	kT	$6.75\text{e-}01^{+3.37\text{e}-02}_{-4.05\text{e}-02}$
	H	1.00
	He	1.00
	C	1.00
	N	1.00
	O	$4.82^{+8.67\text{e}-01}_{-2.29\text{e}-01}$
	Ne	$2.05^{+5.52\text{e}-01}_{-1.64\text{e}-01}$
	Mg	1.00
	Si	$2.33^{+1.40\text{e}-01}_{-1.63\text{e}-01}$
	S	$5.33^{+1.14}_{-1.17}$
	Ar	1.00
	Ca	1.00
	Fe	1.00
	Ni	1.00
	Tau	$1.75\text{e+}11^{+4.98\text{e}+13}_{-1.75\text{e}+11}$
	Redshift	0.00
	norm	$1.33\text{e-}06^{+6.67\text{e}-09}_{-6.66\text{e}-09}$
gain offsets	TM1	-3.88e-03
	TM2	6.35e-04
	TM3	-4.72e-03

Continued

	TM4	1.25e-03
	TM6	-5.39e-03

Table A.7.: Final fit parameters for the eRASS2 fit for the disk region with 90% confidence interval errors

Model component	parameter	best fit value
const1	factor1	1.00
const2	factor2	1.82e+06
SWCX: acx2	temperature	1.31e-01
	collnpar	4.50e+02
	collntype	2
	acxmodel	8
	recombtype	1
	Hefrac	9.00e-02
	abund	1.00
	redshift	0.00
	norm	$3.61\text{e-}04^{+8.61\text{e}-05}_{-9.12\text{e}-06}$
LHB: apec	kT	$1.20\text{e-}01^{+0.00}_{-3.00\text{e}-02}$
	Abundanc	1.00
	Redshift	0.00
	norm	$6.24\text{e-}07^{+0.00}_{-6.24\text{e}-08}$
CGM: vapec	kT	$1.75\text{e-}01^{+3.14\text{e}-08}_{-1.75\text{e}-03}$
	He	8.00e-02
	C	8.00e-02
	N	8.00e-02
	O	$4.00\text{e-}02^{+4.00\text{e}-04}_{-4.00\text{e}-02}$
	Ne	$9.44\text{e-}02^{+2.06\text{e}-01}_{-1.39\text{e}-03}$
	Mg	$3.00\text{e-}01^{+0.00}_{-1.97\text{e}-02}$
	Al	8.00e-02
	Si	$3.00\text{e-}01^{+0.00}_{-2.72\text{e}-02}$
	S	$3.00\text{e-}01^{+0.00}_{-6.56\text{e}-03}$
	Ar	8.00e-02
	Ca	8.00e-02
	Fe	$3.00\text{e-}01^{+0.00}_{-2.60\text{e}-01}$
	Ni	8.00e-02
	Redshift	0.00
	norm	$4.22\text{e-}04^{+1.00\text{e}+20}_{-4.22\text{e}-04}$
Cor: apec	kT	$5.44\text{e-}01^{+4.64\text{e}-10}_{-5.44\text{e}-01}$

Continued

	Abundanc	1.00
	Redshift	0.00
	norm	$2.40\text{e-}07^{+3.07\text{e}-09}_{-4.36\text{e}-09}$
CXB: powerlaw	PhoIndex	1.46
	norm	$1.99\text{e-}06^{+1.16\text{e}-08}_{-1.89\text{e}-08}$
vnei	kT	$7.61\text{e-}01^{+3.04\text{e}-02}_{-2.28\text{e}-02}$
	H	1.00
	He	1.00
	C	1.00
	N	1.00
	O	$2.46^{+1.72\text{e}-01}_{-3.19\text{e}-01}$
	Ne	$1.32^{+2.81\text{e}-02}_{-4.56\text{e}-02}$
	Mg	$5.39\text{e-}01^{+4.59\text{e}-02}_{-3.97\text{e}-02}$
	Si	$1.51^{+8.30\text{e}-02}_{-8.20\text{e}-02}$
	S	$4.39^{+6.28\text{e}-01}_{-5.91\text{e}-01}$
	Ar	1.00
	Ca	1.00
	Fe	1.00
	Ni	1.00
	Tau	$1.30\text{e+}11^{+1.45\text{e}+09}_{-4.08\text{e}+09}$
	Redshift	0.00
	norm	$2.27\text{e-}06^{+3.44\text{e}-08}_{-1.64\text{e}-07}$
gain offsets	TM1	-3.70e-03
	TM2	1.36e-03
	TM3	-5.45e-03
	TM4	-4.35e-03

Table A.8.: Final fit parameters for the eRASS3 fit for the disk region with 90% confidence interval errors

Model component	parameter	best fit value
const1	factor1	1.00
const2	factor2	1.82e+06
SWCX: acx2	temperature	1.31e-01
	collnpar	4.50e+02
	collntype	2
	acxmodel	8
	recombtype	1
	Hefrac	9.00e-02

Continued

	abund	1.00
	redshift	0.00
	norm	$3.81\text{e-}04^{+5.68\text{e}-06}_{-4.01\text{e}-06}$
LHB: apec	kT	$1.20\text{e-}01^{+0.00}_{-1.13\text{e}-03}$
	Abundanc	1.00
	Redshift	0.00
	norm	$6.24\text{e-}07^{+0.00}_{-3.17\text{e}-08}$
CGM: vapec	kT	$1.74\text{e-}01^{+1.74\text{e}-03}_{-1.74\text{e}-03}$
	He	8.00e-02
	C	8.00e-02
	N	8.00e-02
	O	$4.00\text{e-}02^{+2.22\text{e}-04}_{-4.00\text{e}-02}$
	Ne	$8.20\text{e-}02^{+2.18\text{e}-01}_{-3.33\text{e}-03}$
	Mg	$1.56\text{e-}01^{+1.06\text{e}-01}_{-4.06\text{e}-02}$
	Al	8.00e-02
	Si	$3.00\text{e-}01^{+0.00}_{-1.78\text{e}-02}$
	S	$3.00\text{e-}01^{+0.00}_{-1.88\text{e}-03}$
	Ar	8.00e-02
	Ca	8.00e-02
	Fe	$2.42\text{e-}01^{+5.20\text{e}-02}_{-1.15\text{e}-02}$
	Ni	8.00e-02
	Redshift	0.00
	norm	$4.42\text{e-}04^{+6.70\text{e}-06}_{-6.61\text{e}-06}$
Cor: apec	kT	$7.40\text{e-}01^{+3.70\text{e}-03}_{-1.04\text{e}-02}$
	Abundanc	1.00
	Redshift	0.00
	norm	$1.62\text{e-}06^{+8.16\text{e}-09}_{-5.61\text{e}-08}$
CXB: powerlaw	PhoIndex	1.46
	norm	$2.58\text{e-}06^{+8.62\text{e}-09}_{-2.99\text{e}-08}$
vnei	kT	$7.00\text{e-}01^{+2.80\text{e}-02}_{-7.00\text{e}-02}$
	H	1.00
	He	1.00
	C	1.00
	N	1.00
	O	$2.83^{+8.50\text{e}-02}_{-2.27\text{e}-01}$
	Ne	$1.60^{+2.23\text{e}-07}_{-1.60\text{e}-02}$
	Mg	$6.15\text{e-}01^{+8.65\text{e}-02}_{-1.08\text{e}-01}$
	Si	$1.77^{+1.37\text{e}-01}_{-1.47\text{e}-01}$
	S	$6.79^{+9.04\text{e}-01}_{-1.05}$
	Ar	1.00
	Ca	1.00

Continued

	Fe	$8.23\text{e-}01^{+3.29\text{e}-02}_{-5.76\text{e}-02}$
	Ni	1.00
	Tau	$1.60\text{e}+11^{+1.15\text{e}+10}_{-3.88\text{e}+10}$
	Redshift	0.00
	norm	$2.05\text{e-}06^{+1.00\text{e}+20}_{-2.65\text{e}-07}$
gain offsets	TM1	-2.94e-03
	TM2	1.24e-03
	TM3	-4.35e-03
	TM4	2.28e-03
	TM6	-6.45e-03

Table A.9.: Final fit parameters for the eRASS4 fit for the disk region with 90% confidence interval errors

A.3.3. Southern region

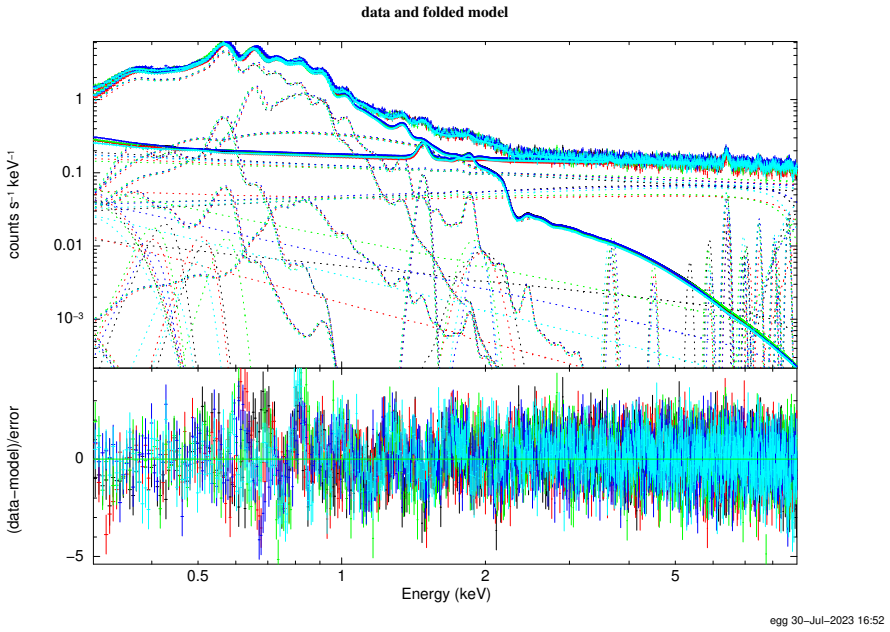

Figure A.7.: Final fit on the southern eRASS2 data

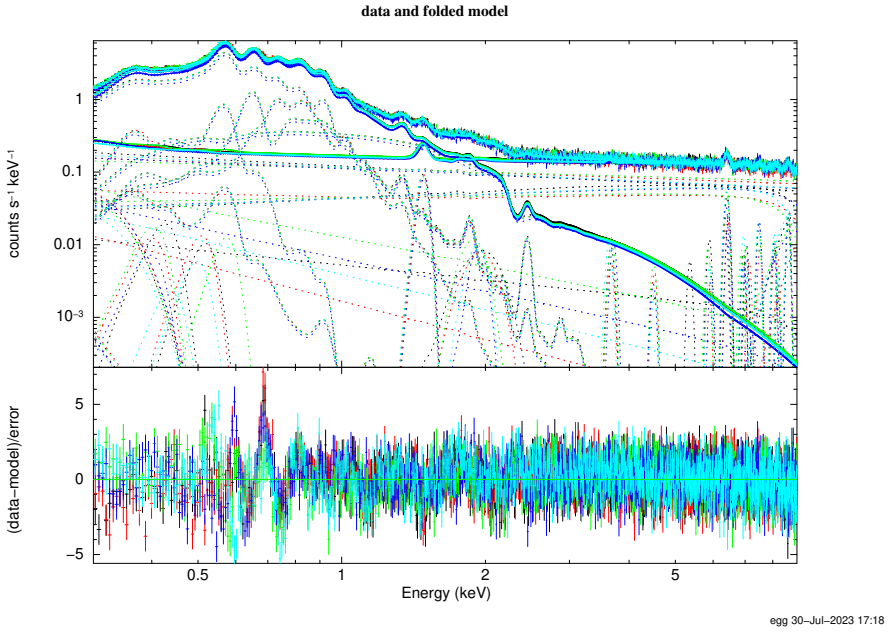

Figure A.8.: Final fit on the southern eRASS3 data

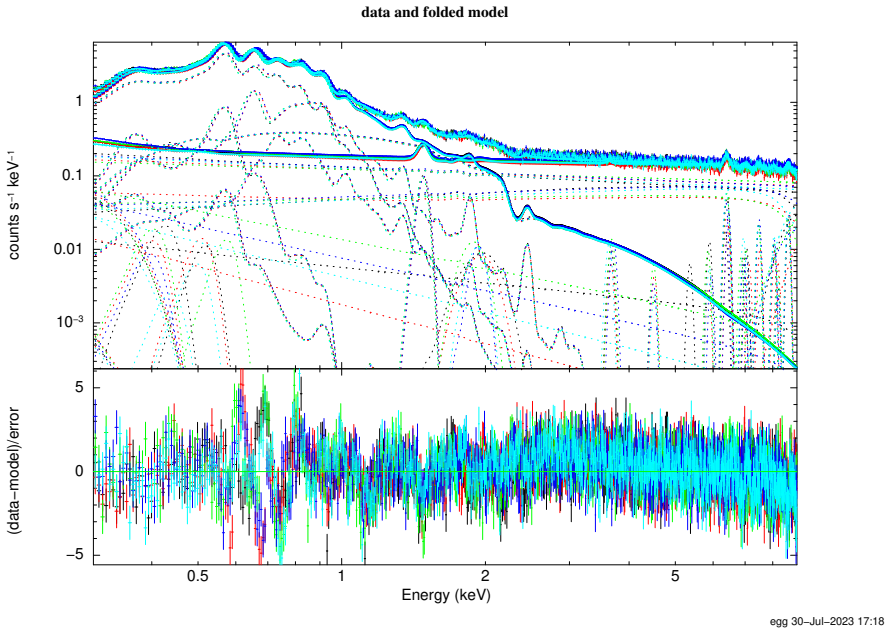

Figure A.9.: Final fit on the southern eRASS4 data

Model component	parameter	best fit value
const1	factor1	1.00
const2	factor2	1.02e+06
SWCX: acx2	temperature	1.35e-01
	collnpar	4.50e+02
	collntype	2
	acxmodel	8
	recombtype	1
	Hefrac	9.00e-02
	abund	1.00
	redshift	0.00
	norm	$3.57\text{e-}04^{+6.80\text{e}-05}_{-1.12\text{e}-04}$
LHB: apec	kT	$1.27\text{e-}01^{+2.60\text{e}-03}_{-2.74\text{e}-02}$
	Abundanc	1.00
	Redshift	0.00
	norm	$6.01\text{e-}07^{+9.82\text{e}-08}_{-6.01\text{e}-07}$
CGM: vapec	kT	$1.92\text{e-}01^{+1.92\text{e}-03}_{-3.84\text{e}-03}$
	He	8.00e-02
	C	8.00e-02
	N	8.00e-02
	O	$6.30\text{e-}02^{+2.52\text{e}-03}_{-1.89\text{e}-03}$
	Ne	$1.26\text{e-}01^{+5.05\text{e}-03}_{-6.32\text{e}-03}$
	Mg	8.00e-02
	Al	8.00e-02
	Si	8.00e-02
	S	8.00e-02
	Ar	8.00e-02
	Ca	8.00e-02
	Fe	8.00e-02
	Ni	8.00e-02
	Redshift	0.00
	norm	$1.05\text{e-}04^{+5.96\text{e}-06}_{-4.64\text{e}-06}$
Cor: apec	kT	$5.50\text{e-}01^{+2.00\text{e}-01}_{-0.00}$
	Abundanc	1.00
	Redshift	0.00
	norm	$1.93\text{e-}06^{+4.90\text{e}-08}_{-6.66\text{e}-08}$
CXB: powerlaw	PhoIndex	1.46
	norm	$1.13\text{e-}06^{+1.41\text{e}-08}_{-1.47\text{e}-08}$
vnei	kT	$1.41^{+5.88\text{e}-01}_{-2.85\text{e}-01}$
	H	1.00
	He	1.00
	C	1.00

Continued

	N	1.00
	O	$8.23^{+5.18}_{-3.01}$
	Ne	1.00
	Mg	1.00
	Si	$3.77^{+1.29}_{-1.17}$
	S	1.00
	Ar	1.00
	Ca	1.00
	Fe	1.00
	Ni	1.00
	Tau	$5.83\text{e+}10^{+2.41\text{e+}10}_{-1.98\text{e+}10}$
	Redshift	0.00
	norm	$8.40\text{e-}08^{+2.41\text{e}-08}_{-2.04\text{e}-08}$
gain offsets	TM1	-7.19e-04
	TM2	3.31e-03
	TM3	-3.90e-03
	TM4	3.85e-03
	TM6	-5.32e-03

Table A.10.: Final fit parameters for the eRASS1 fit for the southern region with 90% confidence interval errors

Model component	parameter	best fit value
const1	factor1	1.00
const2	factor2	1.02e+06
SWCX: acx2	temperature	1.35e-01
	collnpar	4.50e+02
	collntype	2
	acxmodel	8
	recombtype	1
	Hefrac	9.00e-02
	abund	1.00
	redshift	0.00
	norm	$2.65\text{e-}04^{+2.07\text{e}-05}_{-9.16\text{e}-06}$
LHB: apec	kT	$1.00\text{e-}01^{+7.00\text{e}-03}_{-1.00\text{e}-01}$
	Abundanc	1.00
	Redshift	0.00
	norm	$3.12\text{e-}07^{+3.36\text{e}-08}_{-3.12\text{e}-07}$
CGM: vapec	kT	$1.82\text{e-}01^{+6.81\text{e}-02}_{-3.19\text{e}-02}$

Continued

	He	8.00e-02
	C	8.00e-02
	N	8.00e-02
	O	$5.99\text{e-}02^{+9.10\text{e}-04}_{-4.93\text{e}-04}$
	Ne	$1.11\text{e-}01^{+2.21\text{e}-03}_{-4.43\text{e}-03}$
	Mg	8.00e-02
	Al	8.00e-02
	Si	8.00e-02
	S	8.00e-02
	Ar	8.00e-02
	Ca	8.00e-02
	Fe	$3.00\text{e-}01^{+0.00}_{-1.22\text{e}-02}$
	Ni	8.00e-02
	Redshift	0.00
	norm	$1.22\text{e-}04^{+4.37\text{e}-06}_{-1.83\text{e}-06}$
Cor: apec	kT	$6.82\text{e-}01^{+6.82\text{e}-02}_{-3.75\text{e}-02}$
	Abundanc	1.00
	Redshift	0.00
	norm	$9.14\text{e-}08^{+1.49\text{e}-08}_{-6.68\text{e}-09}$
CXB: powerlaw	PhoIndex	1.46
	norm	$1.20\text{e-}06^{+1.12\text{e}-08}_{-6.02\text{e}-09}$
vnei	kT	$7.13\text{e-}01^{+4.99\text{e}-02}_{-3.57\text{e}-02}$
	H	1.00
	He	1.00
	C	1.00
	N	1.00
	O	$2.33^{+7.85\text{e}-01}_{-1.65\text{e}-01}$
	Ne	1.00
	Mg	1.00
	Si	$1.54^{+1.98\text{e}-01}_{-2.10\text{e}-01}$
	S	1.00
	Ar	1.00
	Ca	1.00
	Fe	1.00
	Ni	1.00
	Tau	$1.56\text{e+}11^{+4.98\text{e}+13}_{-1.56\text{e}+11}$
	Redshift	0.00
	norm	$1.09\text{e-}06^{+2.45\text{e}-08}_{-1.04\text{e}-08}$
gain offsets	TM1	1.15e-03
	TM2	4.48e-03
	TM3	-4.20e-03

Continued

	TM4	3.15e-03
	TM6	-3.32e-03

Table A.11.: Final fit parameters for the eRASS2 fit for the southern region with 90% confidence interval errors

Model component	parameter	best fit value
const1	factor1	1.00
const2	factor2	1.02e+06
SWCX: acx2	temperature	1.35e-01
	collnpar	4.50e+02
	collntype	2
	acxmodel	8
	recombtype	1
	Hefrac	9.00e-02
	abund	1.00
	redshift	0.00
	norm	$4.66\text{e-}04^{+7.06\text{e}-06}_{-1.61\text{e}-05}$
LHB: apec	kT	$1.00\text{e-}01^{+3.00\text{e}-02}_{-1.03\text{e}-06}$
	Abundanc	1.00
	Redshift	0.00
	norm	$3.12\text{e-}07^{+1.54\text{e}-07}_{-3.12\text{e}-07}$
CGM: vapec	kT	$1.79\text{e-}01^{+4.48\text{e}-03}_{-2.93\text{e}-02}$
	He	8.00e-02
	C	8.00e-02
	N	8.00e-02
	O	$5.97\text{e-}02^{+5.97\text{e}-04}_{-2.98\text{e}-03}$
	Ne	$1.20\text{e-}01^{+4.82\text{e}-03}_{-8.43\text{e}-03}$
	Mg	8.00e-02
	Al	8.00e-02
	Si	$1.25\text{e-}01^{+2.73\text{e}-02}_{-2.47\text{e}-02}$
	S	8.00e-02
	Ar	8.00e-02
	Ca	8.00e-02
	Fe	$3.00\text{e-}01^{+0.00}_{-1.03\text{e}-02}$
	Ni	8.00e-02
	Redshift	0.00
	norm	$1.18\text{e-}04^{+6.71\text{e}-06}_{-6.35\text{e}-06}$
Cor: apec	kT	$5.41\text{e-}01^{+2.16\text{e}-02}_{-1.42\text{e}-08}$

Continued

	Abundanc	1.00
	Redshift	0.00
	norm	$2.85\text{e-}07^{+5.14\text{e}-08}_{-2.72\text{e}-09}$
CXB: powerlaw	PhoIndex	1.46
	norm	$1.22\text{e-}06^{+9.95\text{e}-09}_{-1.78\text{e}-08}$
vnei	kT	$7.13\text{e-}01^{+6.59\text{e}-02}_{-2.14\text{e}-02}$
	H	1.00
	He	1.00
	C	1.00
	N	1.00
	O	$2.24^{+4.03\text{e}-01}_{-6.72\text{e}-02}$
	Ne	1.00
	Mg	1.00
	Si	1.00
	S	$5.49^{+1.72}_{-1.63}$
	Ar	1.00
	Ca	1.00
	Fe	1.00
	Ni	1.00
	Tau	$1.46\text{e}+11^{+1.40\text{e}+09}_{-3.54\text{e}+10}$
	Redshift	0.00
	norm	$1.09\text{e-}06^{+5.49\text{e}-09}_{-5.48\text{e}-09}$
gain offsets	TM1	2.99e-04
	TM2	6.87e-04
	TM3	-4.16e-04
	TM4	3.65e-04
	TM6	-3.99e-04

Table A.12.: Final fit parameters for the eRASS3 fit for the southern region with 90% confidence interval errors

Model component	parameter	best fit value
const1	factor1	1.00
const2	factor2	1.02e+06
SWCX: acx2	temperature	1.35e-01
	collnpar	4.50e+02
	collntype	2
	acxmodel	8
	recombtype	1

Continued

	Hefrac	9.00e-02
	abund	1.00
	redshift	0.00
	norm	$2.95\text{e-}04^{+2.08\text{e}-06}_{-5.04\text{e}-05}$
LHB: apec	kT	$1.00\text{e-}01^{+2.00\text{e}-03}_{-1.00\text{e}-01}$
	Abundanc	1.00
	Redshift	0.00
	norm	$3.12\text{e-}07^{+1.12\text{e}-08}_{-3.12\text{e}-07}$
CGM: vapec	kT	$1.80\text{e-}01^{+7.04\text{e}-02}_{-2.96\text{e}-02}$
	He	8.00e-02
	C	8.00e-02
	N	8.00e-02
	O	$6.01\text{e-}02^{+2.31\text{e}-04}_{-4.63\text{e}-04}$
	Ne	$9.60\text{e-}02^{+9.60\text{e}-04}_{-1.92\text{e}-03}$
	Mg	8.00e-02
	Al	8.00e-02
	Si	8.00e-02
	S	8.00e-02
	Ar	8.00e-02
	Ca	8.00e-02
	Fe	$3.00\text{e-}01^{+0.00}_{-3.75\text{e}-03}$
	Ni	8.00e-02
	Redshift	0.00
	norm	$1.29\text{e-}04^{+6.50\text{e}-07}_{-3.21\text{e}-06}$
Cor: apec	kT	$6.84\text{e-}01^{+6.84\text{e}-03}_{-2.74\text{e}-02}$
	Abundanc	1.00
	Redshift	0.00
	norm	$1.40\text{e-}07^{+9.85\text{e}-10}_{-1.97\text{e}-08}$
CXB: powerlaw	PhoIndex	1.46
	norm	$1.30\text{e-}06^{+9.36\text{e}-09}_{-1.33\text{e}-08}$
vnei	kT	$7.33\text{e-}01^{+1.27}_{-5.33\text{e}-01}$
	H	1.00
	He	1.00
	C	1.00
	N	1.00
	O	$1.67^{+2.43\text{e}-01}_{-1.38\text{e}-01}$
	Ne	1.00
	Mg	$8.74\text{e-}01^{+6.38\text{e}-02}_{-7.09\text{e}-02}$
	Si	$1.63^{+1.76\text{e}-01}_{-1.82\text{e}-01}$
	S	$7.08^{+1.20}_{-1.64}$
	Ar	1.00

Continued

	Ca	1.00
	Fe	1.00
	Ni	1.00
	Tau	$1.17\text{e+}11^{+1.43\text{e+}10}_{-5.59\text{e+}03}$
	Redshift	0.00
	norm	$1.00\text{e-}06^{+2.55\text{e}-08}_{-5.03\text{e}-09}$
gain offsets	TM1	6.18e-04
	TM2	3.00e-03
	TM3	-2.42e-03
	TM4	3.11e-03
	TM6	-2.96e-03

Table A.13.: Final fit parameters for the eRASS4 fit for the southern region with 90% confidence interval errors

A.4. Line lists

Energy [keV]	σ	width [keV]	norm [ph/(cm^2 s)]	origin
2.325	1.70068	0.11274	4.28753e-09	
2.625	4.09306	0.11661	8.11979e-09	
3.0	2.26161	0.12146	4.94696e-09	
3.125	3.28727	0.12307	7.40130e-09	
3.325	2.11927	0.12566	4.95065e-09	
3.475	3.23539	0.1276	7.96029e-09	
3.775	0.39132	0.13147	1.01323e-09	instrumental
4.0	2.38449	0.13438	6.64926e-09	
4.20024	1.45292	0.13697	4.41970e-09	averaged
4.425	1.19073	0.13987	3.93207e-09	instrumental
4.6	0.51603	0.14213	1.83821e-09	instrumental
5.4	1.14348	0.15247	6.18739e-09	instrumental
5.9	0.70476	0.15893	5.16857e-09	instrumental
6.375	2.2119	0.16507	2.42489e-08	instrumental
7.05	1.79011	0.17379	2.42318e-08	instrumental
7.55	1.44935	0.18025	2.52780e-08	instrumental

Table A.14.: Line list for the northern region in eRASS1

Energy [keV]	σ	width [keV]	norm [ph/(cm^2 s)]	origin
2.325	5.04696	0.11274	1.22034e-08	
2.62528	3.79103	0.11662	7.31994e-09	averaged
2.925	2.88634	0.12049	5.95432e-09	
3.225	3.72581	0.12437	8.31039e-09	
3.45	3.05158	0.12727	7.08180e-09	
3.75	2.21769	0.13115	5.46222e-09	instrumental
4.025	3.30829	0.1347	8.87259e-09	
4.375	1.69464	0.13922	5.20026e-09	
4.575	0.8748	0.14181	2.93561e-09	instrumental
4.975	0.81088	0.14698	3.30341e-09	
5.15	0.96602	0.14924	4.32945e-09	
5.4	2.39972	0.15247	1.24034e-08	instrumental
6.1	1.0442	0.16151	8.03280e-09	
6.325	2.18721	0.16442	2.10077e-08	instrumental
7.075	2.1482	0.17411	2.79419e-08	instrumental
7.475	1.35156	0.17928	2.18653e-08	instrumental

Table A.15.: Line list for the northern region in eRASS2

Energy [keV]	σ	width [keV]	norm [ph/(cm^2 s)]	origin
2.075	0.14213	0.10951	1.02441e-10	instrumental
2.3	5.79061	0.11242	1.26718e-08	
2.65	5.46196	0.11694	1.01466e-08	
3.025	6.06273	0.12178	1.24655e-08	
3.2	4.85439	0.12404	1.05149e-08	
3.425	2.94449	0.12695	6.57839e-09	
3.575	2.92533	0.12889	6.71365e-09	instrumental
4.025	2.64627	0.1347	6.88412e-09	
4.3	1.08879	0.13826	3.13425e-09	
4.825	2.29661	0.14504	8.46597e-09	
5.25	0.47515	0.15053	2.18384e-09	instrumental
5.5	0.81394	0.15376	4.28112e-09	
5.925	0.45087	0.15925	3.07783e-09	instrumental
6.225	2.18163	0.16313	1.78525e-08	

Table A.16.: Line list for the northern region in eRASS3

Energy [keV]	σ	width [keV]	norm [ph/(cm^2 s)]	origin
2.4	5.45145	0.11371	1.16595e-08	
2.775	4.99145	0.11855	1.08985e-08	
3.05026	2.62925	0.12211	5.53375e-09	averaged
3.275	4.72057	0.12501	1.05627e-08	
3.725	2.5525	0.13083	6.29367e-09	instrumental
4.075	3.82465	0.13535	1.04676e-08	
4.275	1.95481	0.13793	5.71535e-09	
4.675	3.9273	0.1431	1.38943e-08	
4.975	0.62889	0.14698	2.55259e-09	
5.2	1.44282	0.14988	6.64790e-09	
5.51283	2.30483	0.15393	1.30469e-08	averaged
5.975	1.34641	0.1599	9.72807e-09	instrumental
6.525	3.8741	0.167	4.05577e-08	instrumental

Table A.17.: Line list for the northern region in eRASS4

Energy [keV]	σ	width [keV]	norm [ph/(cm^2 s)]	origin
2.375	2.95889	0.11338	7.48028e-09	
2.675	4.04114	0.11726	8.46941e-09	
2.925	3.73528	0.12049	8.22076e-09	
3.075	4.68303	0.12243	1.03729e-08	
3.35	3.62136	0.12598	8.40570e-09	
3.775	1.42231	0.13147	3.56558e-09	instrumental
4.025	0.48037	0.1347	1.28389e-09	
4.55	2.05207	0.14149	6.79442e-09	instrumental
4.725	0.64206	0.14375	2.27759e-09	
5.125	0.67751	0.14891	2.94052e-09	
5.525	0.25832	0.15408	1.38619e-09	
5.75	1.2403	0.15699	7.59779e-09	instrumental
6.475	3.60978	0.16636	3.75550e-08	instrumental
7.1	2.10338	0.17443	2.65815e-08	instrumental
7.525	5.4934	0.17992	8.91505e-08	instrumental

Table A.18.: Line list for the disk region in eRASS1

Energy [keV]	σ	width [keV]	norm [ph/(cm^2 s)]	origin
2.325	2.6302	0.11274	6.77982e-09	
2.6	5.30648	0.11629	1.04445e-08	
2.75	5.22012	0.11823	1.16669e-08	
2.95	4.29385	0.12081	9.06762e-09	
3.075	5.14112	0.12243	1.09502e-08	
3.2	3.91415	0.12404	8.67223e-09	
3.425	2.61331	0.12695	5.91653e-09	
3.75	0.13311	0.13115	3.17501e-10	instrumental
4.0	1.90696	0.13438	4.86411e-09	
4.375	1.40655	0.13922	4.11986e-09	
4.575	0.81904	0.14181	2.61706e-09	instrumental
4.875	1.44466	0.14568	5.29270e-09	
5.075	1.5765	0.14827	6.39210e-09	
5.375	1.93546	0.15214	9.24333e-09	instrumental
6.01281	0.46819	0.16039	3.29751e-09	averaged instrumental
6.375	4.27724	0.16507	4.14675e-08	instrumental
6.7	0.3112	0.16926	3.05171e-09	
7.075	0.24894	0.17411	2.97065e-09	instrumental
7.55	2.73383	0.18025	4.21609e-08	instrumental
8.15	1.04479	0.188	2.11927e-08	instrumental

Table A.19.: Line list for the disk region in eRASS2

Energy [keV]	σ	width [keV]	norm [ph/(cm^2 s)]	origin
2.35	5.62356	0.11306	1.73032e-08	
2.625	inf	0.11661	1.99536e-08	
2.775	6.40148	0.11855	1.69120e-08	
3.175	7.99157	0.12372	2.09653e-08	
3.5	3.10746	0.12792	8.38787e-09	
3.775	4.49613	0.13147	1.27840e-08	instrumental
3.95	4.2173	0.13373	1.25024e-08	
4.2	3.59619	0.13696	1.15533e-08	
4.4	2.53378	0.13955	8.81765e-09	instrumental
4.75	3.28204	0.14407	1.33360e-08	
5.025	1.12137	0.14762	5.17395e-09	
5.225	1.97774	0.15021	1.01255e-08	

Table A.20.: Line list for the disk region in eRASS3

Energy [keV]	σ	width [keV]	norm [ph/(cm^2 s)]	origin
2.35	8.12589	0.11306	2.18242e-08	
2.6	6.21998	0.11629	1.24156e-08	
2.725	6.50702	0.11791	1.42357e-08	
2.95	6.48667	0.12081	1.38637e-08	
3.125	8.0414	0.12307	1.75848e-08	
3.275	5.8014	0.12501	1.28916e-08	
3.525	2.1964	0.12824	5.01306e-09	instrumental
3.975	2.32943	0.13406	5.83634e-09	
4.45	1.9746	0.14019	5.89026e-09	instrumental
4.825	2.45179	0.14504	8.60969e-09	
5.1	1.07917	0.14859	4.32126e-09	
5.5	1.55101	0.15376	7.66808e-09	
5.95	1.27381	0.15957	8.21390e-09	instrumental
6.525	4.87006	0.167	4.59083e-08	instrumental
7.075	2.24778	0.17411	2.60960e-08	instrumental

Table A.21.: Line list for the disk region in eRASS4

Energy [keV]	σ	width [keV]	norm [ph/(cm^2 s)]	origin
2.05	0.33656	0.10919	4.09097e-10	instrumental
2.35	4.25964	0.11306	1.75113e-08	
2.60028	3.25323	0.1163	1.04120e-08	averaged
2.95	4.073	0.12081	1.43727e-08	
3.375	0.19305	0.1263	7.27601e-10	
3.75	2.18375	0.13115	9.16302e-09	instrumental
3.96288	1.39035	0.1339	6.28001e-09	averaged
4.5	2.04757	0.14084	1.14166e-08	instrumental
4.675	0.65775	0.1431	3.91128e-09	
4.925	0.73908	0.14633	5.00098e-09	
5.2	0.09189	0.14988	7.18489e-10	
6.05	0.17129	0.16087	2.17919e-09	instrumental
6.425	0.17399	0.16571	3.19204e-09	instrumental
6.75	0.41716	0.16991	7.72824e-09	instrumental
7.2	0.83758	0.17572	1.92663e-08	instrumental
7.5	1.24822	0.1796	3.49955e-08	instrumental

Table A.22.: Line list for the southern region in eRASS1

Energy [keV]	σ	width [keV]	norm [ph/(cm^2 s)]	origin
2.375	3.23378	0.11338	1.25587e-08	
2.6	3.55453	0.11629	1.14638e-08	
2.825	3.16726	0.1192	1.15322e-08	
3.175	2.94087	0.12372	1.12220e-08	
3.425	3.01326	0.12695	1.20525e-08	
3.675	0.38653	0.13018	1.62777e-09	instrumental
4.175	2.01361	0.13664	9.85431e-09	
4.4	1.90932	0.13955	1.03053e-08	instrumental
4.8	2.60202	0.14472	1.69697e-08	
5.225	0.08255	0.15021	6.66280e-10	
5.425	1.38112	0.15279	1.25201e-08	instrumental
5.625	1.37056	0.15538	1.38726e-08	
6.0	0.59177	0.16022	7.50215e-09	instrumental
6.375	2.31844	0.16507	4.21243e-08	instrumental
7.1	0.92492	0.17443	2.10118e-08	instrumental
7.475	0.90005	0.17928	2.53432e-08	instrumental

Table A.23.: Line list for the southern region in eRASS2

Energy [keV]	σ	width [keV]	norm [ph/(cm^2 s)]	origin
2.35	4.6576	0.11306	1.77263e-08	
2.65028	2.54824	0.11694	7.84437e-09	averaged
2.8	2.86764	0.11888	9.53176e-09	
3.17526	2.80505	0.12372	9.72442e-09	averaged
3.375	3.20696	0.1263	1.12372e-08	
3.725	3.50003	0.13083	1.34476e-08	instrumental
3.9	2.96007	0.13309	1.18382e-08	
4.2	0.60793	0.13696	2.65991e-09	
4.4	2.77215	0.13955	1.34897e-08	instrumental
4.8	1.82604	0.14472	1.05912e-08	
5.05	1.13125	0.14795	7.45006e-09	
5.35	2.10754	0.15182	1.64856e-08	instrumental
5.625	0.11218	0.15538	1.00831e-09	
6.05	0.64221	0.16087	7.43318e-09	instrumental
6.3	1.42662	0.1641	2.03580e-08	instrumental
6.525	1.98246	0.167	3.18810e-08	instrumental
7.075	0.5054	0.17411	1.01106e-08	instrumental

Table A.24.: Line list for the southern region in eRASS3

Energy [keV]	σ	width [keV]	norm [ph/(cm^2 s)]	origin
2.05	0.38753	0.10919	4.23245e-10	instrumental
2.3	6.01347	0.11242	2.03413e-08	
2.675	8.12589	0.11726	2.40681e-08	
2.975	7.17595	0.12114	2.27862e-08	
3.225	6.15415	0.12437	2.08977e-08	
3.4379	6.46361	0.12712	2.31103e-08	averaged
3.7	4.15535	0.1305	1.55371e-08	instrumental
3.975	6.02943	0.13406	2.42613e-08	
4.225	1.17173	0.13729	5.04976e-09	
4.5	1.91736	0.14084	9.44448e-09	instrumental
5.1	3.13214	0.14859	2.08415e-08	
5.55047	0.97875	0.15441	8.58749e-09	averaged
6.0	0.29319	0.16022	3.23004e-09	instrumental
6.55	1.25262	0.16733	1.95058e-08	instrumental
7.125	0.20161	0.17476	3.99362e-09	instrumental

Table A.25.: Line list for the southern region in eRASS4

A.5. Line detection plots

A.5.1. With errorbars

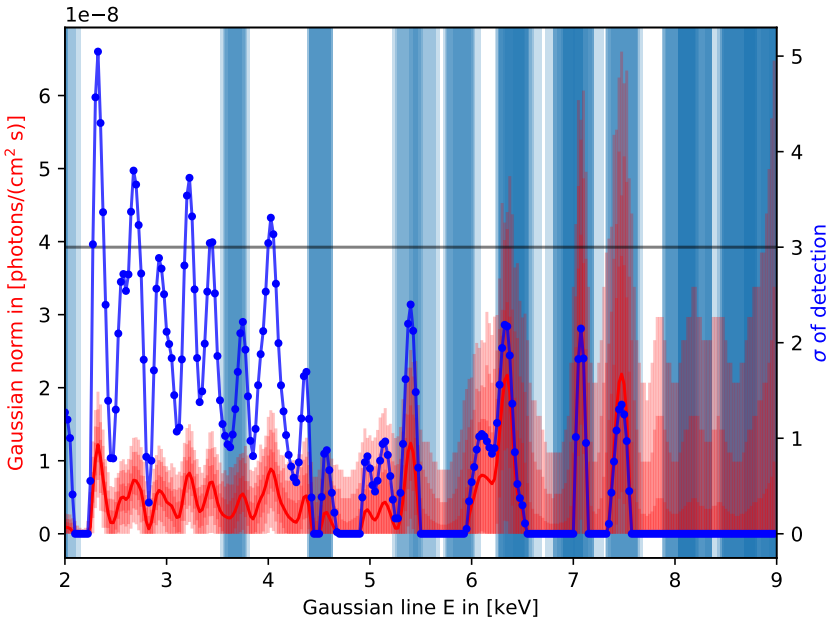

Figure A.10.: Plot of detected lines in the northern region for eRASS2 with errorbars

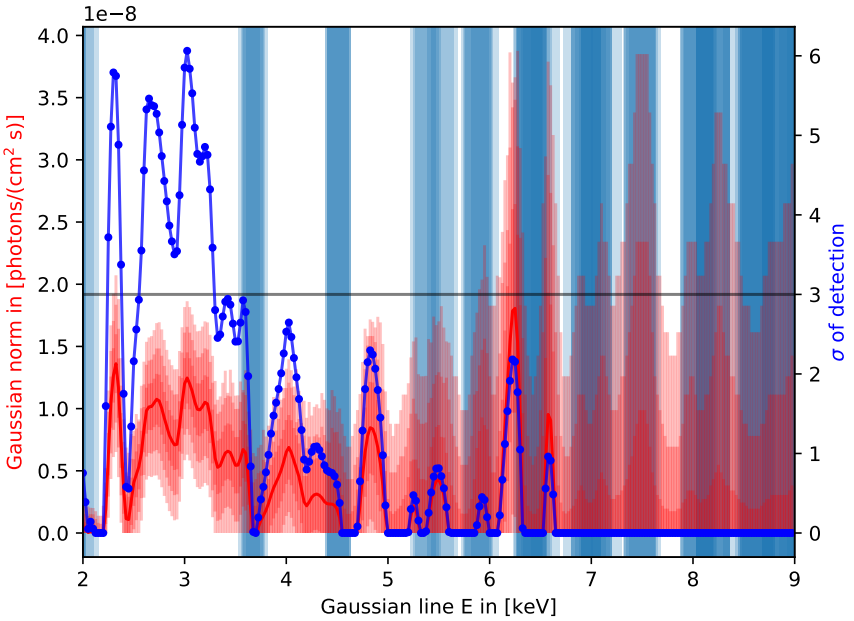

Figure A.11.: Plot of detected lines in the northern region for eRASS3 with errorbars

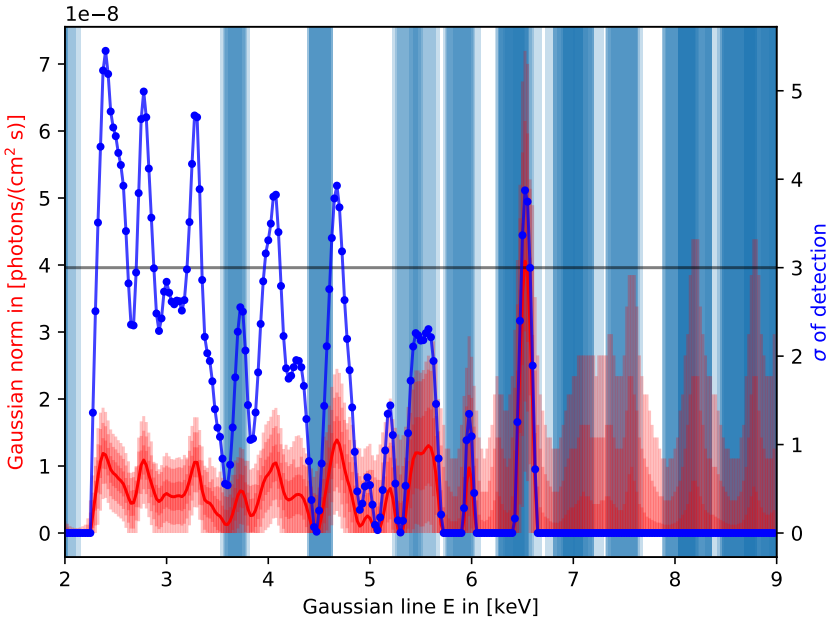

Figure A.12.: Plot of detected lines in the northern region for eRASS4 with errorbars

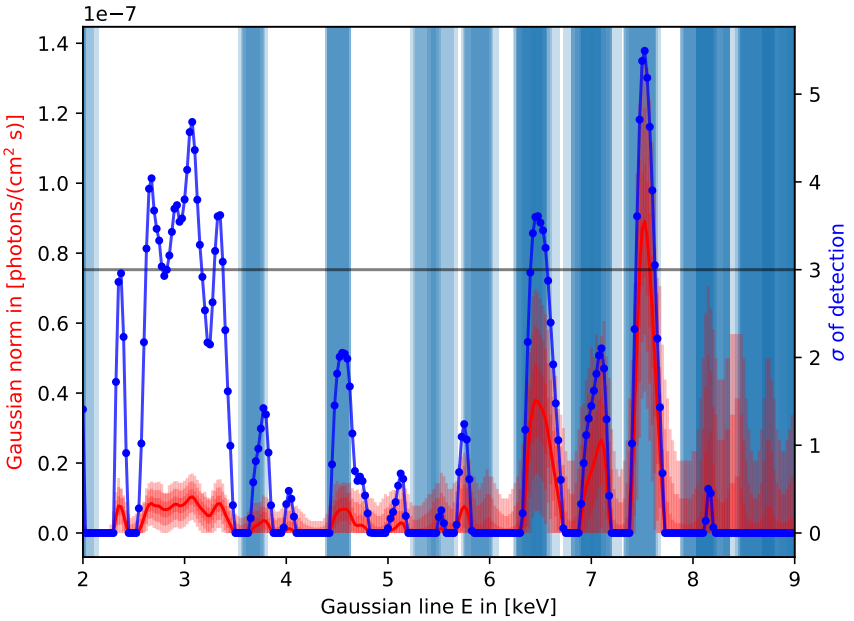

Figure A.13.: Plot of detected lines in the disk region for eRASS1 with errorbars

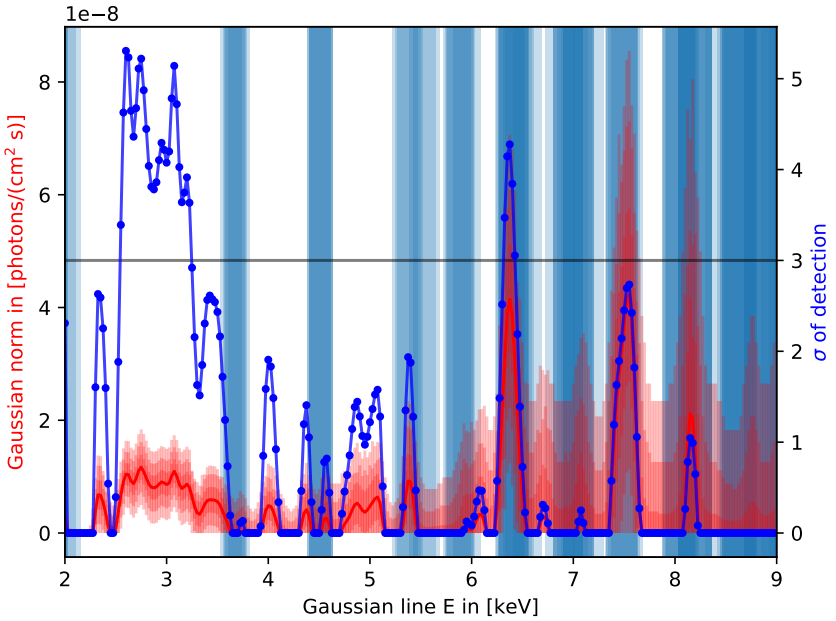

Figure A.14.: Plot of detected lines in the disk region for eRASS2 with errorbars

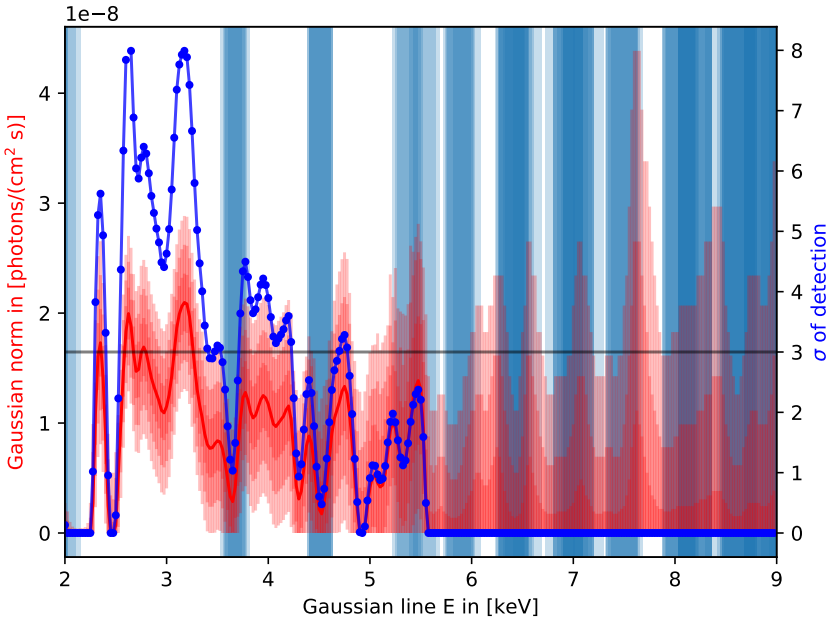

Figure A.15.: Plot of detected lines in the disk region for eRASS3 with errorbars

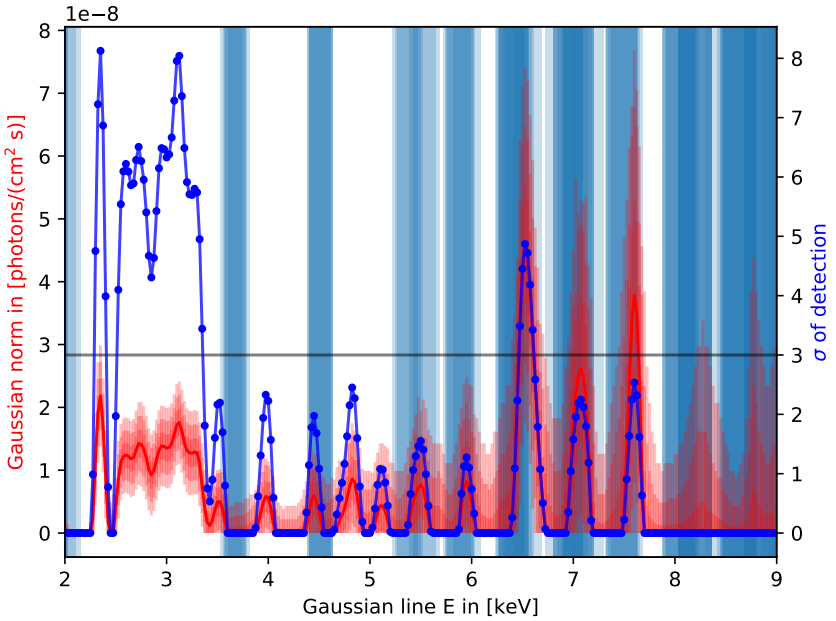

Figure A.16.: Plot of detected lines in the disk region for eRASS4 with errorbars

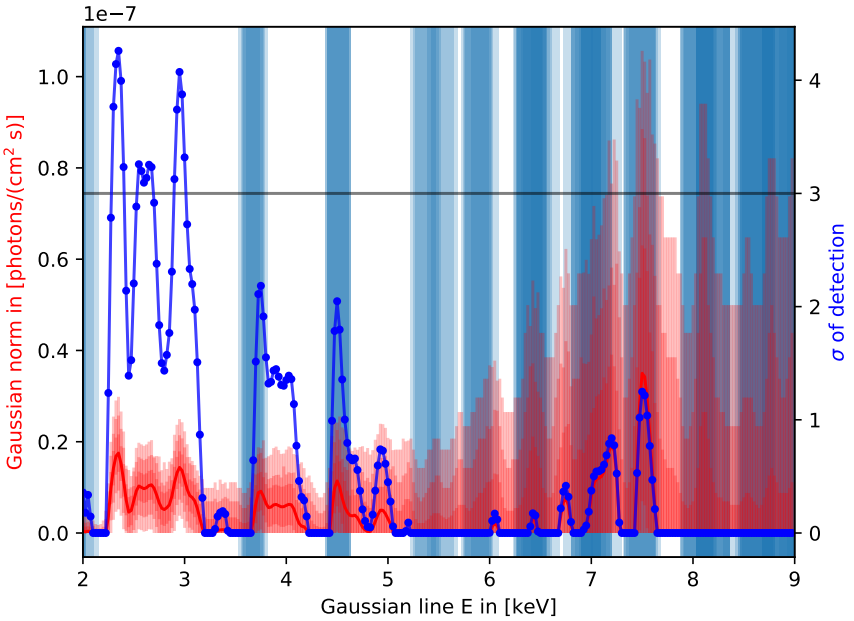

Figure A.17.: Plot of detected lines in the southern region for eRASS1 with errorbars

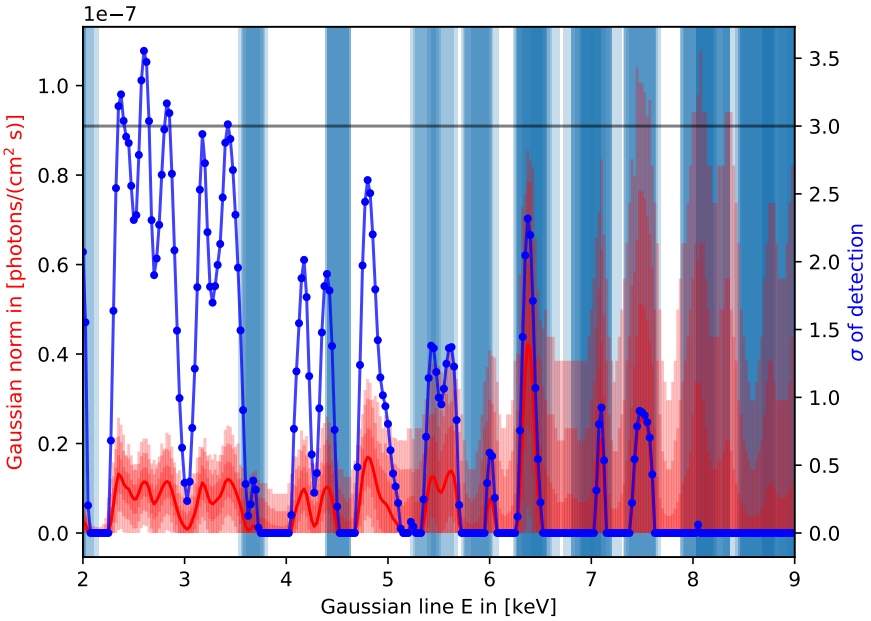

Figure A.18.: Plot of detected lines in the southern region for eRASS2 with errorbars

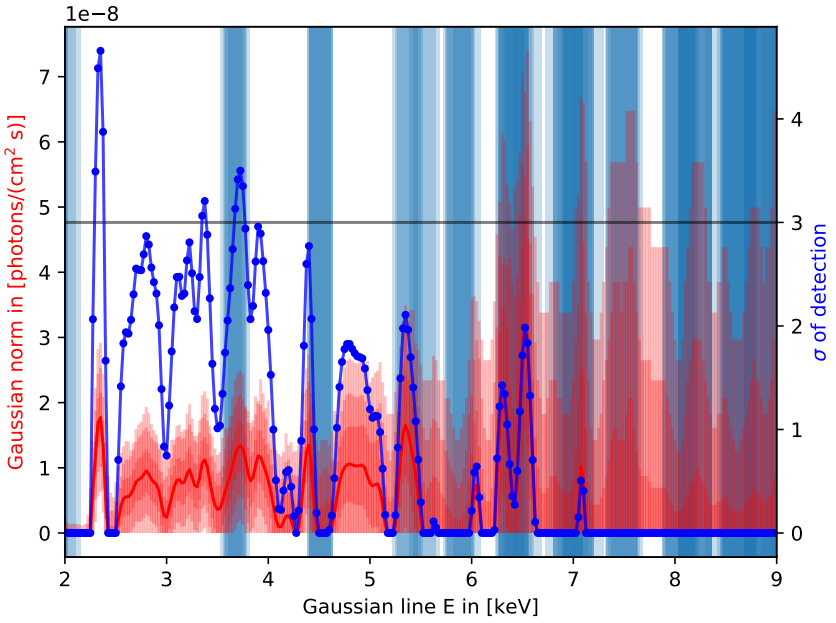

Figure A.19.: Plot of detected lines in the southern region for eRASS3 with errorbars

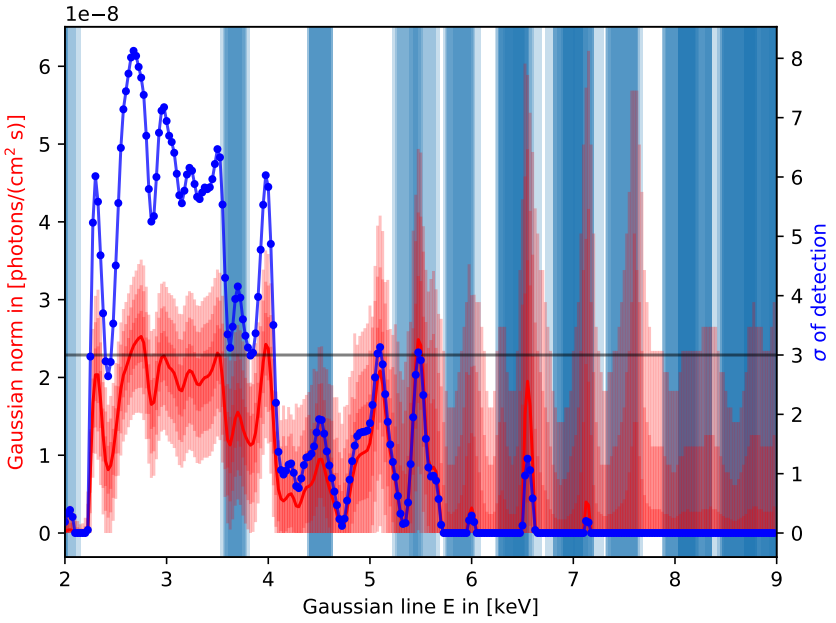

Figure A.20.: Plot of detected lines in the southern region for eRASS4 with errorbars

A.5.2. Logarithmic scale norms

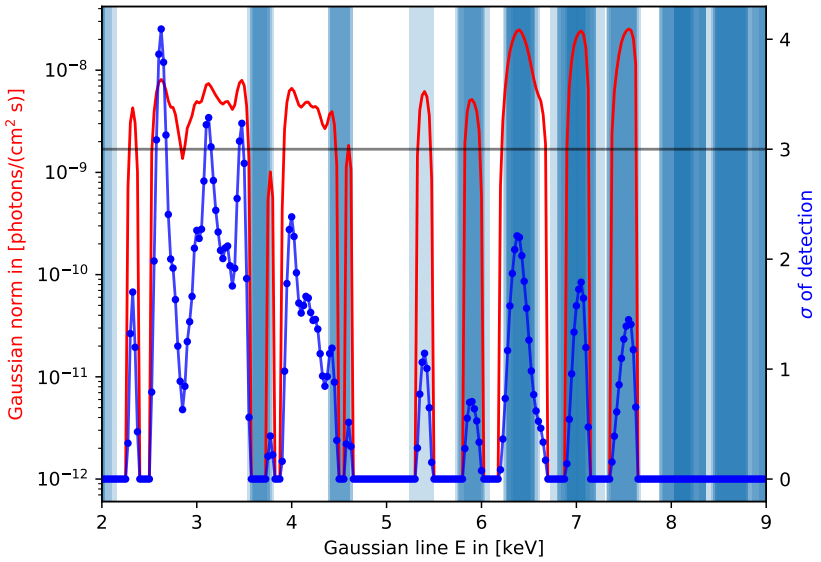

Figure A.21.: Plot of detected lines in the northern region for eRASS1 with norms in logarithmic scale

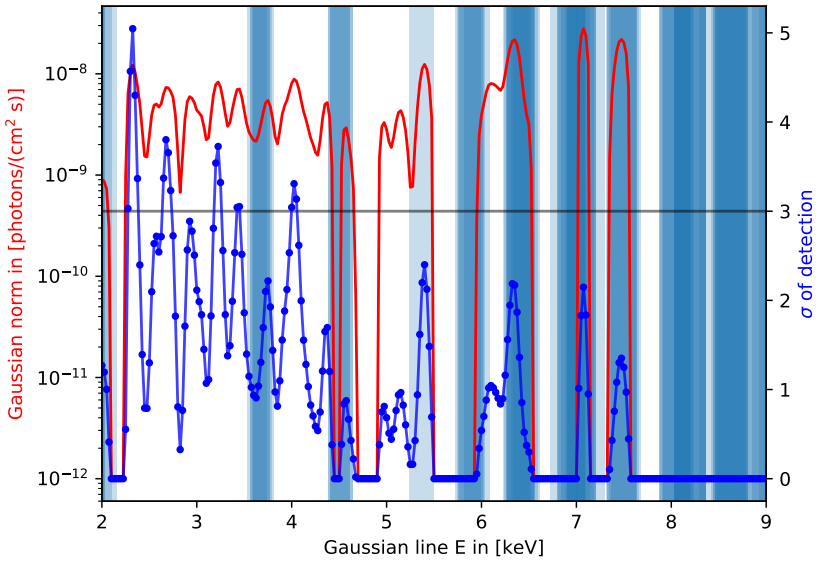

Figure A.22.: Plot of detected lines in the northern region for eRASS2 with norms in logarithmic scale

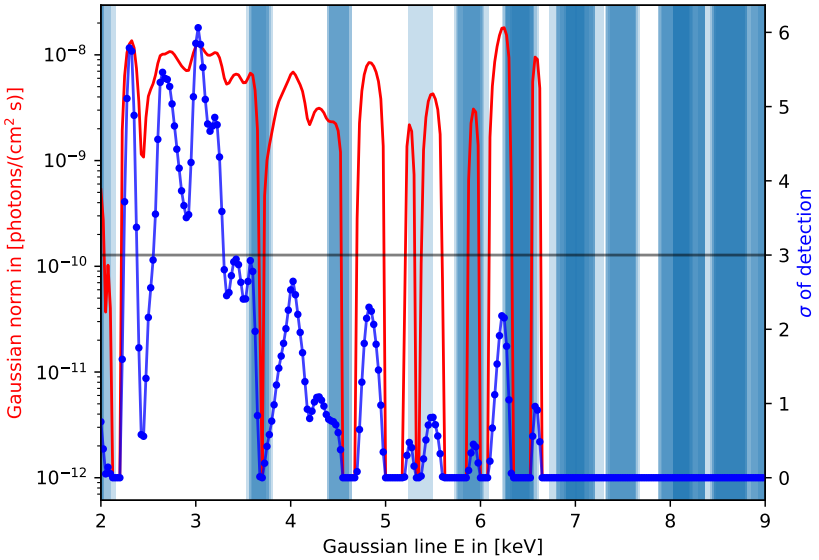

Figure A.23.: Plot of detected lines in the northern region for eRASS3 with norms in logarithmic scale

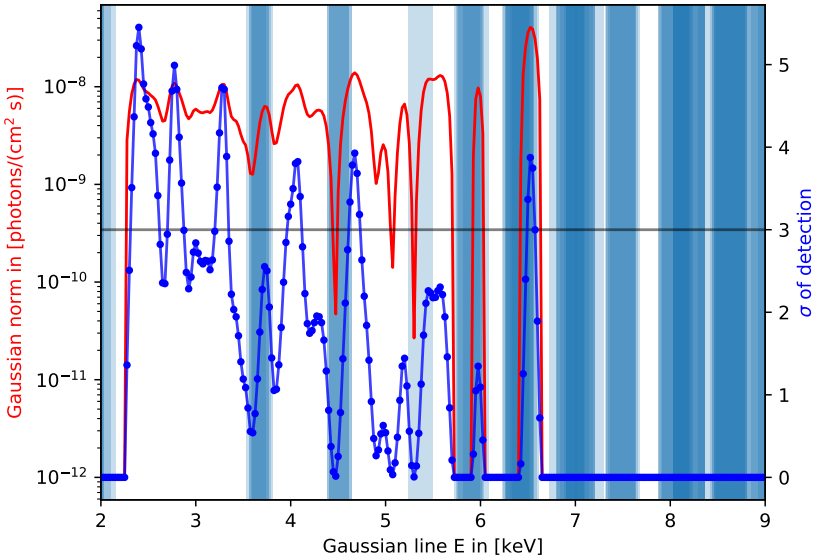

Figure A.24.: Plot of detected lines in the northern region for eRASS4 with norms in logarithmic scale

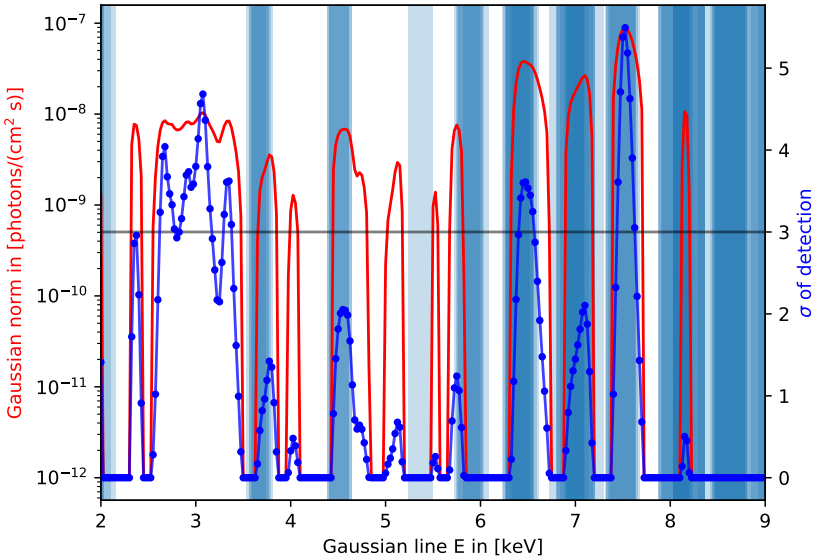

Figure A.25.: Plot of detected lines in the disk region for eRASS1 with norms in logarithmic scale

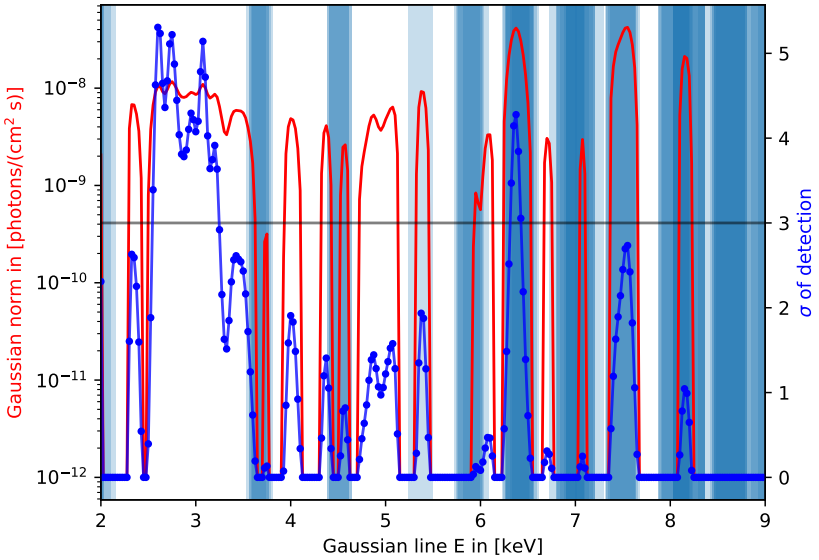

Figure A.26.: Plot of detected lines in the disk region for eRASS2 with norms in logarithmic scale

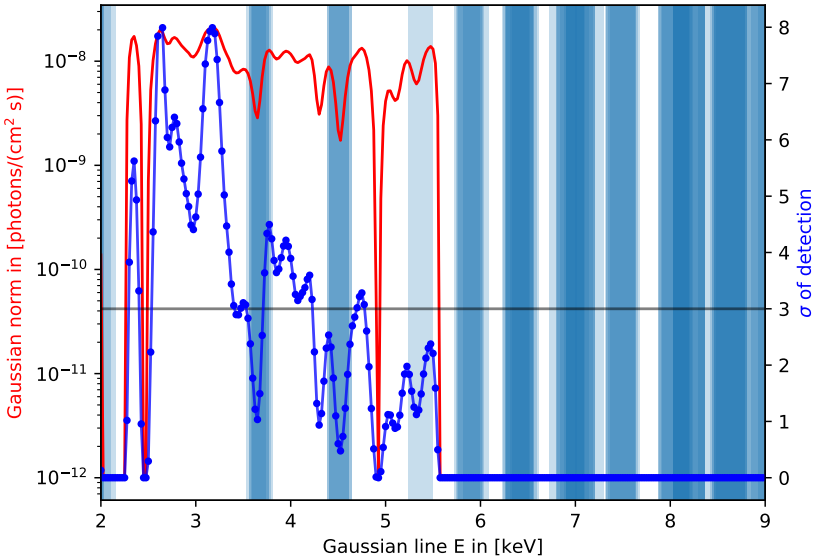

Figure A.27.: Plot of detected lines in the disk region for eRASS3 with norms in logarithmic scale

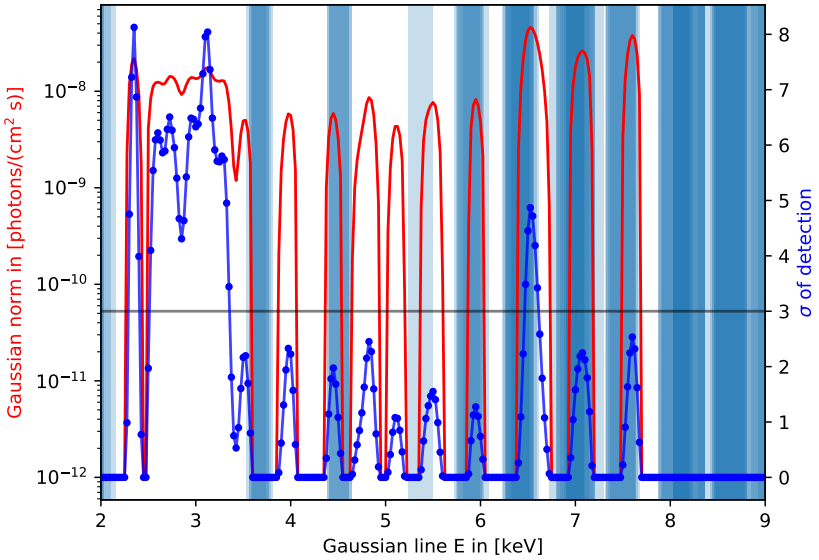

Figure A.28.: Plot of detected lines in the disk region for eRASS4 with norms in logarithmic scale

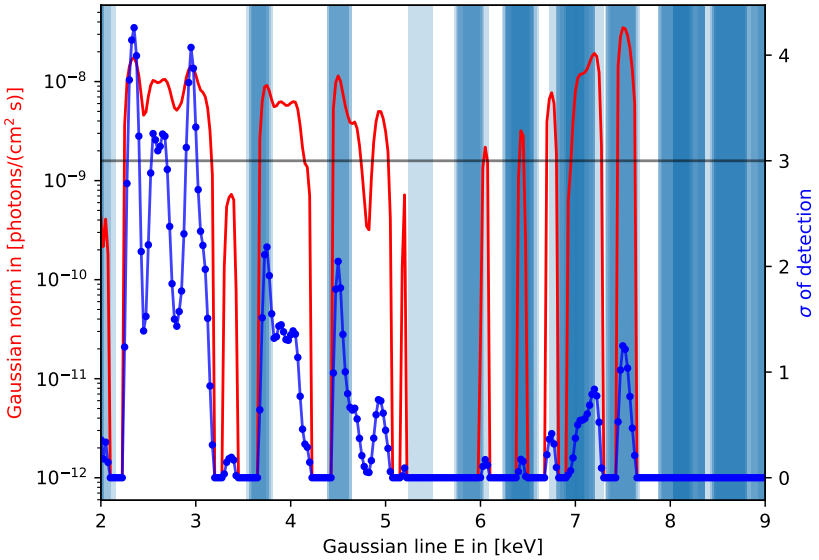

Figure A.29.: Plot of detected lines in the southern region for eRASS1 with norms in logarithmic scale

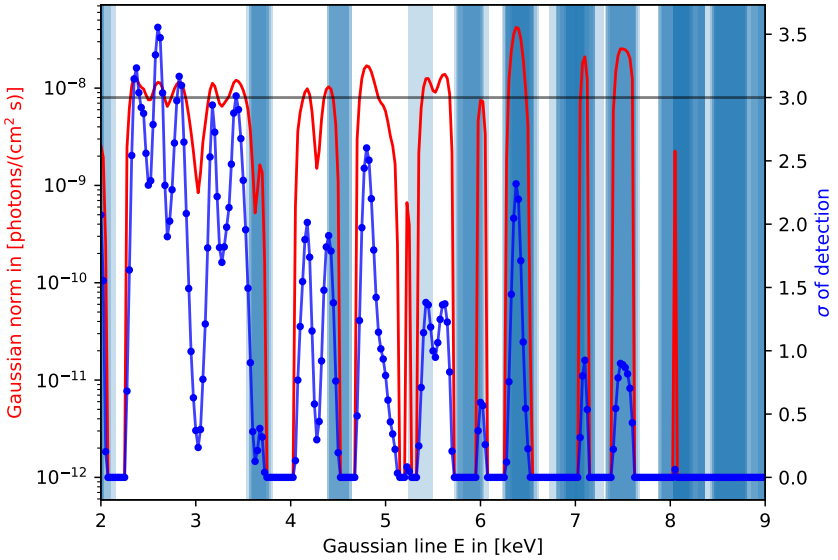

Figure A.30.: Plot of detected lines in the southern region for eRASS2 with norms in logarithmic scale

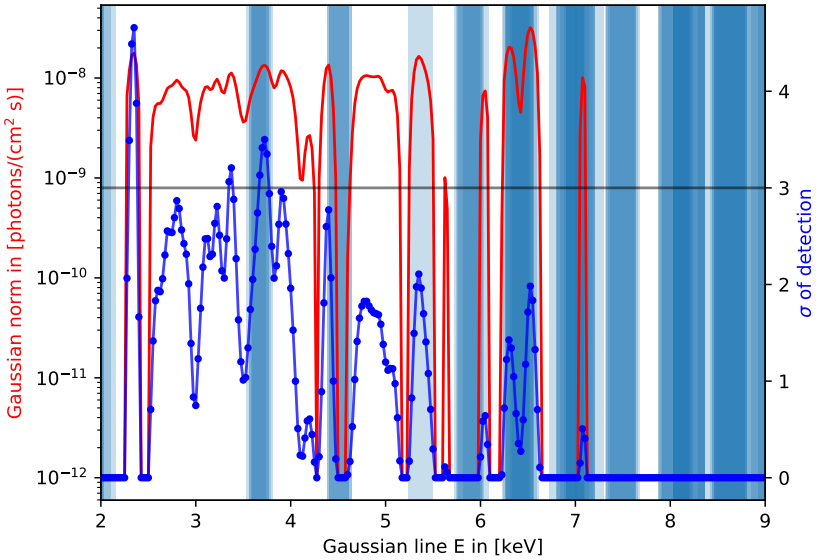

Figure A.31.: Plot of detected lines in the southern region for eRASS3 with norms in logarithmic scale

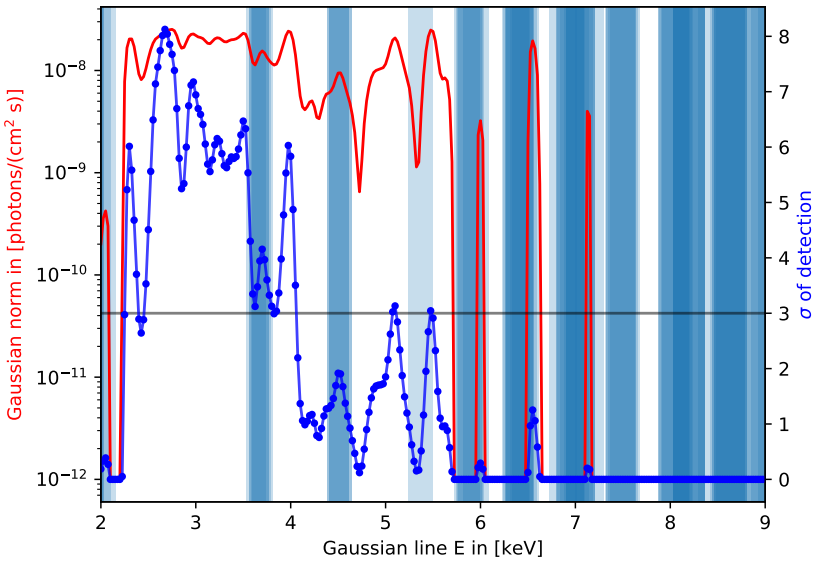

Figure A.32.: Plot of detected lines in the southern region for eRASS4 with norms in logarithmic scale

A.5.3. Overlap plots

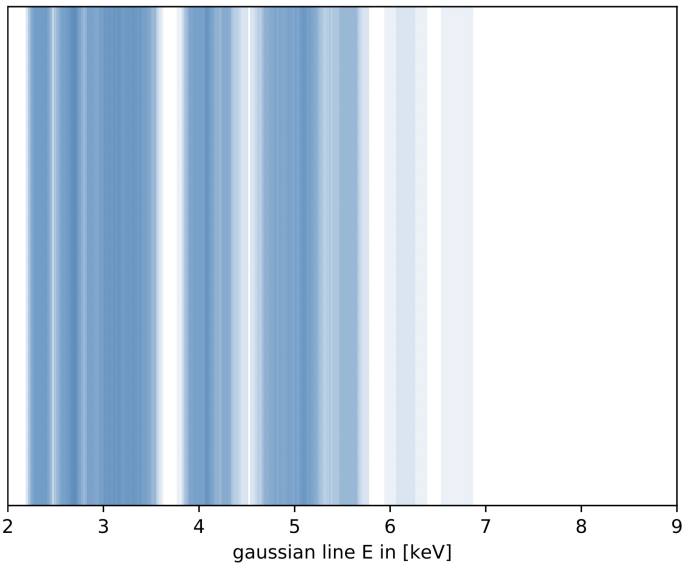

Figure A.33.: Plot showcasing the location and overlap of all detected lines

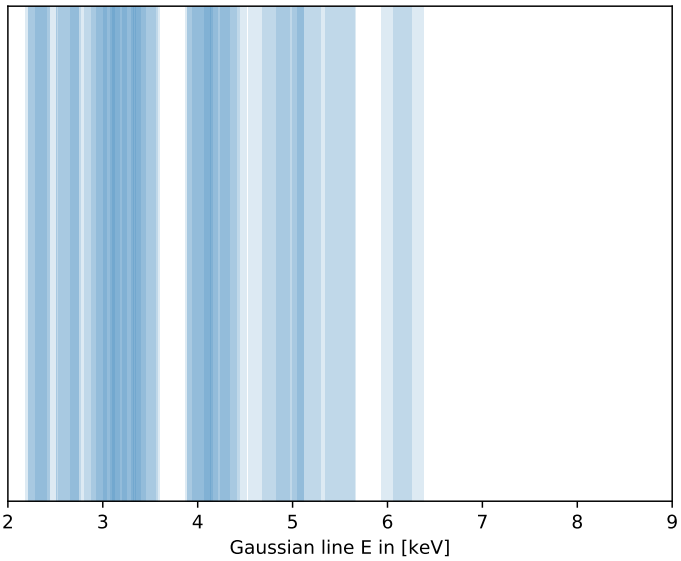

Figure A.34.: Plot showcasing the location and overlap of all detected lines in the northern region

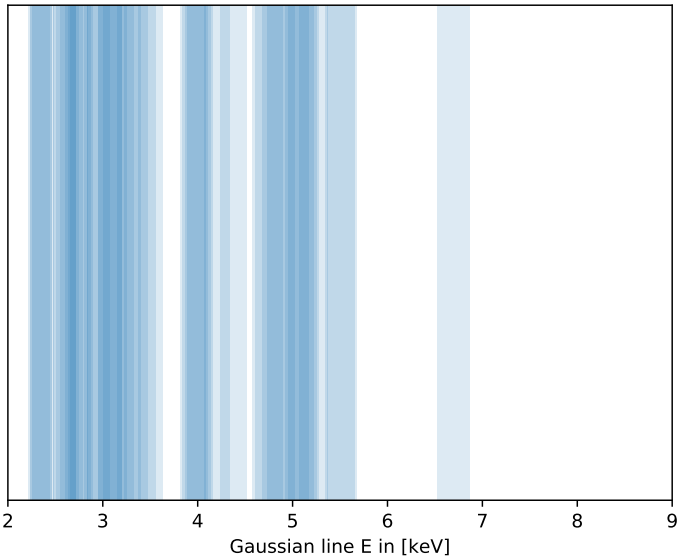

Figure A.35.: Plot showcasing the location and overlap of all detected lines in the disk region

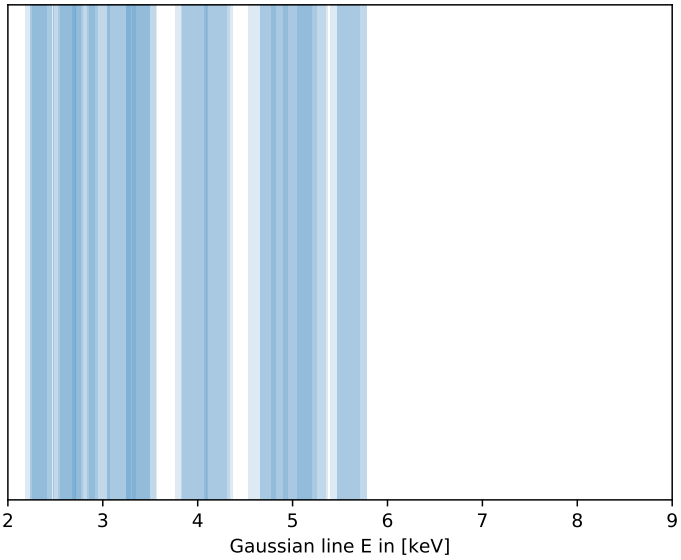

Figure A.36.: Plot showcasing the location and overlap of all detected lines in the southern region

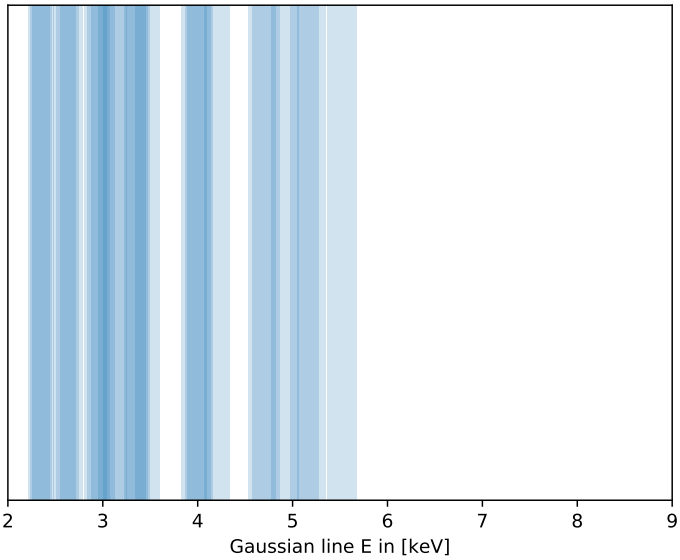

Figure A.37.: Plot showcasing the location and overlap of all detected lines in eRASS1 data

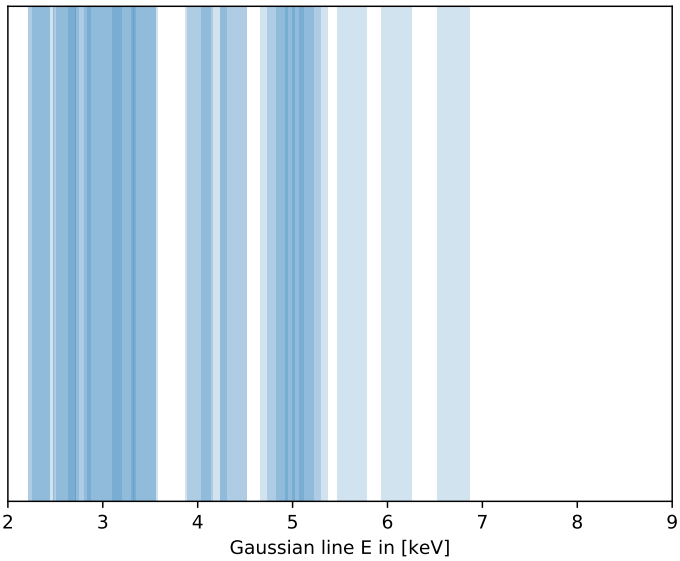

Figure A.38.: Plot showcasing the location and overlap of all detected lines in eRASS2 data

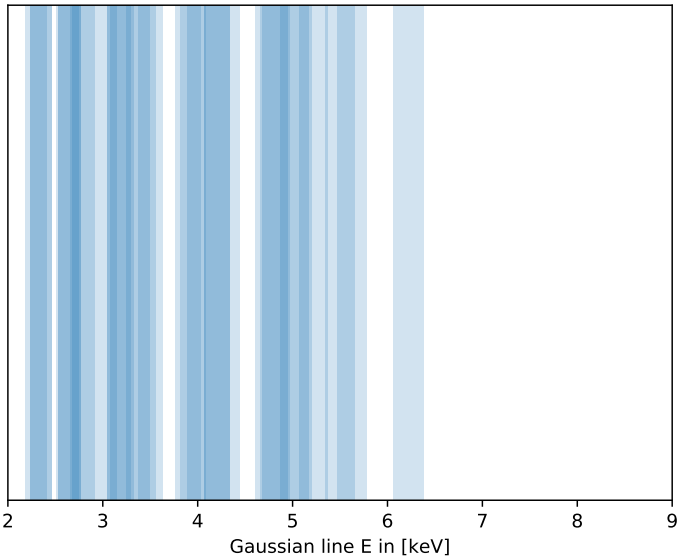

Figure A.39.: Plot showcasing the location and overlap of all detected lines in eRASS3 data

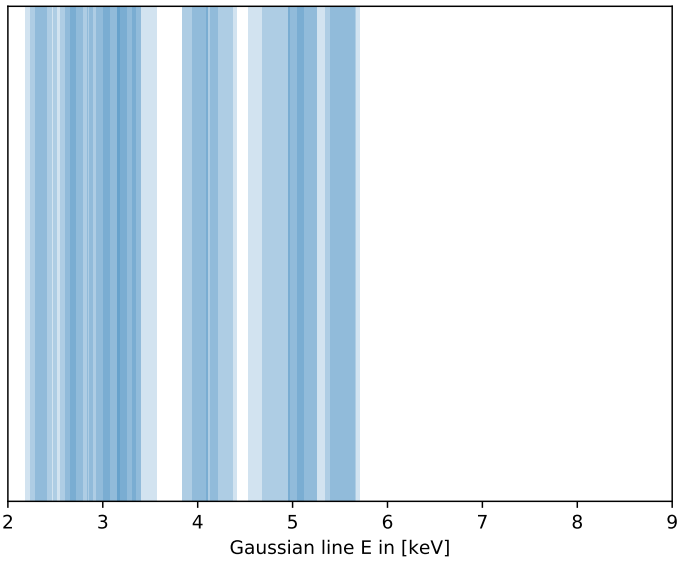

Figure A.40.: Plot showcasing the location and overlap of all detected lines in eRASS4 data

A.6. Charge exchange plots

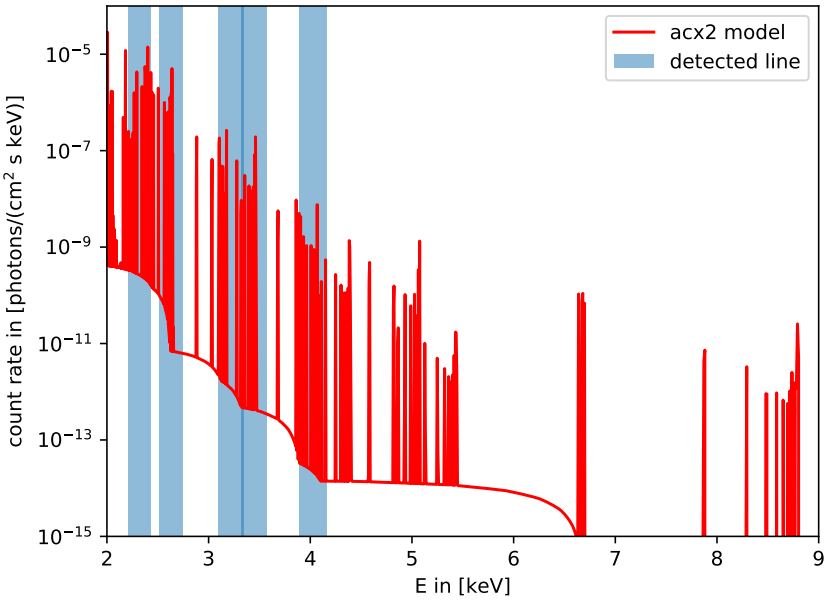

Figure A.41.: Plot showing the location of detected line features (blue) against line emission in the acx2 model (red) for the northern region in eRASS2

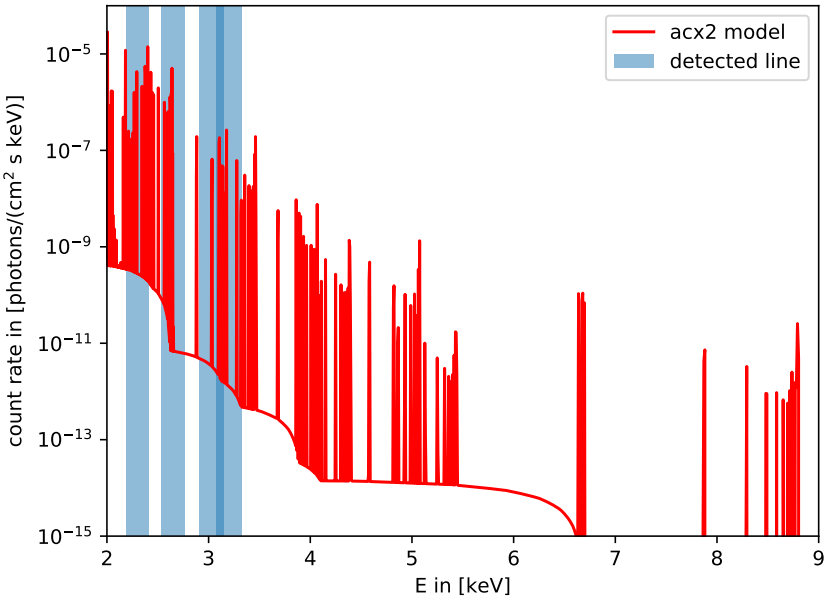

Figure A.42.: Plot showing the location of detected line features (blue) against line emission in the acx2 model (red) for the northern region in eRASS3

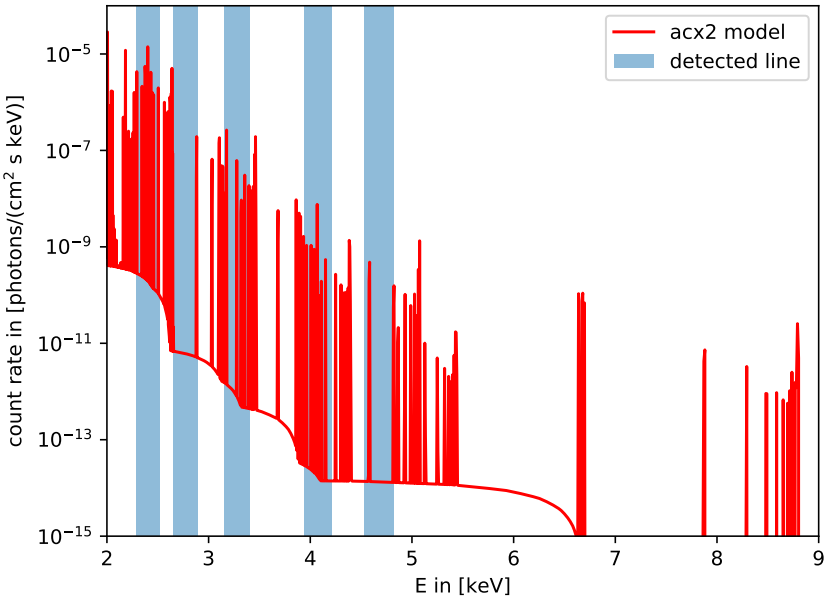

Figure A.43.: Plot showing the location of detected line features (blue) against line emission in the acx2 model (red) for the northern region in eRASS4

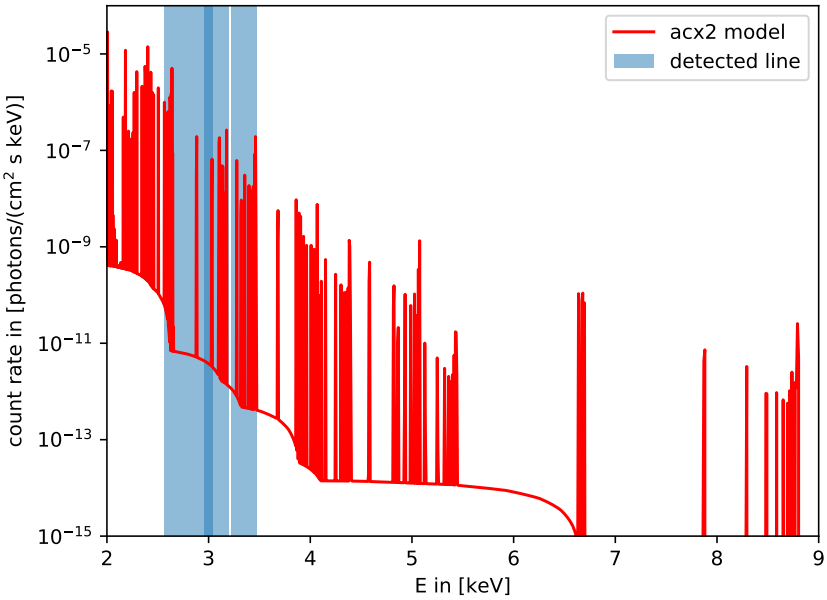

Figure A.44.: Plot showing the location of detected line features (blue) against line emission in the acx2 model (red) for the disk region in eRASS1

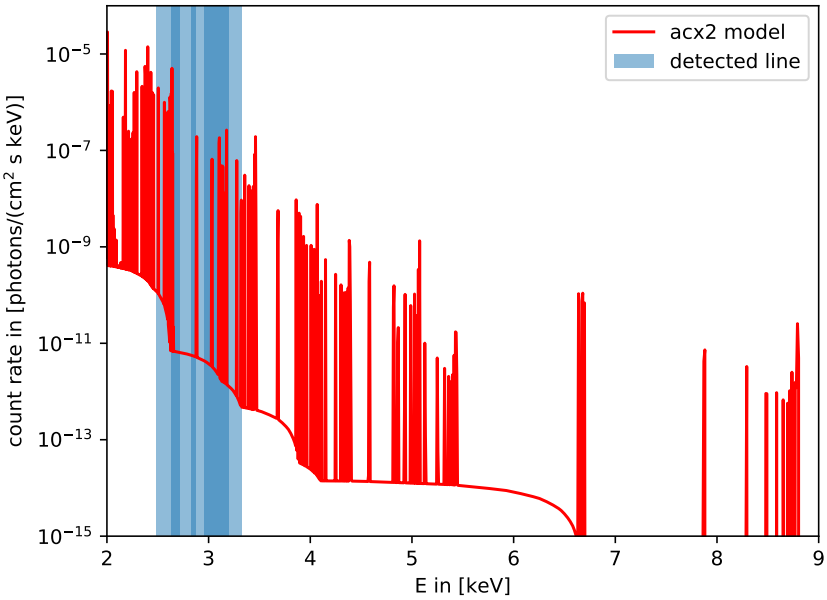

Figure A.45.: Plot showing the location of detected line features (blue) against line emission in the acx2 model (red) for the disk region in eRASS2

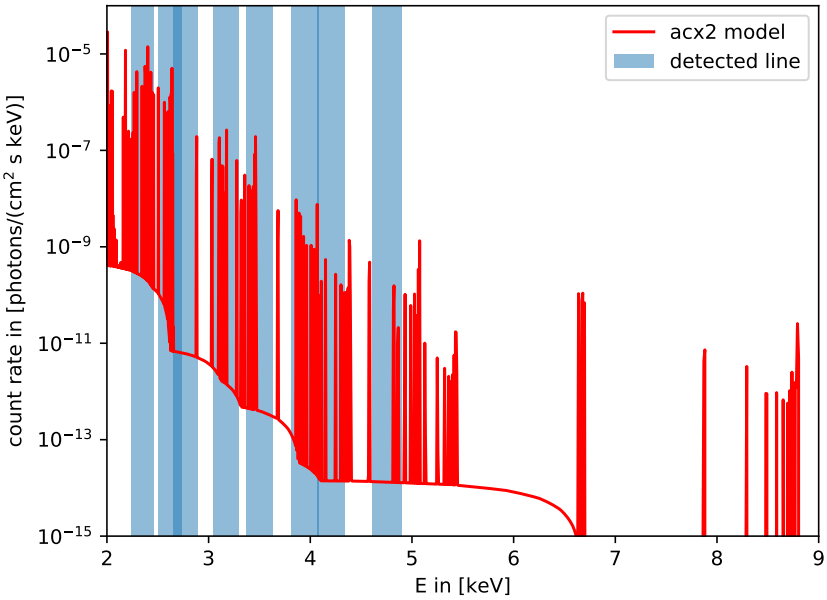

Figure A.46.: Plot showing the location of detected line features (blue) against line emission in the acx2 model (red) for the disk region in eRASS3

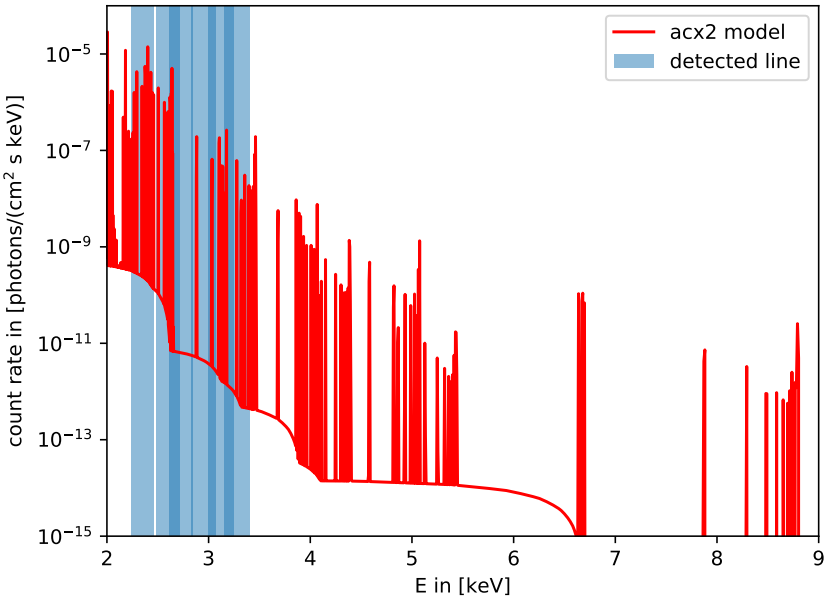

Figure A.47.: Plot showing the location of detected line features (blue) against line emission in the acx2 model (red) for the disk region in eRASS4

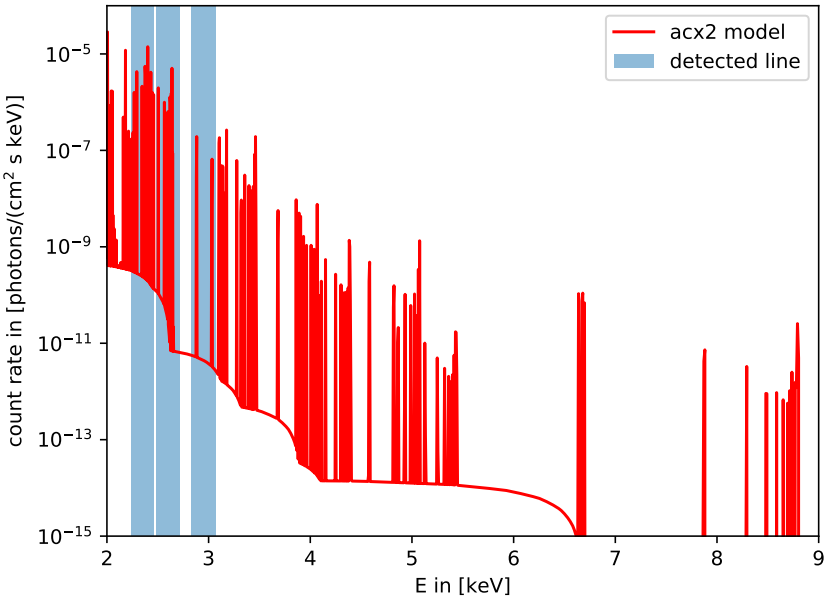

Figure A.48.: Plot showing the location of detected line features (blue) against line emission in the acx2 model (red) for the southern region in eRASS1

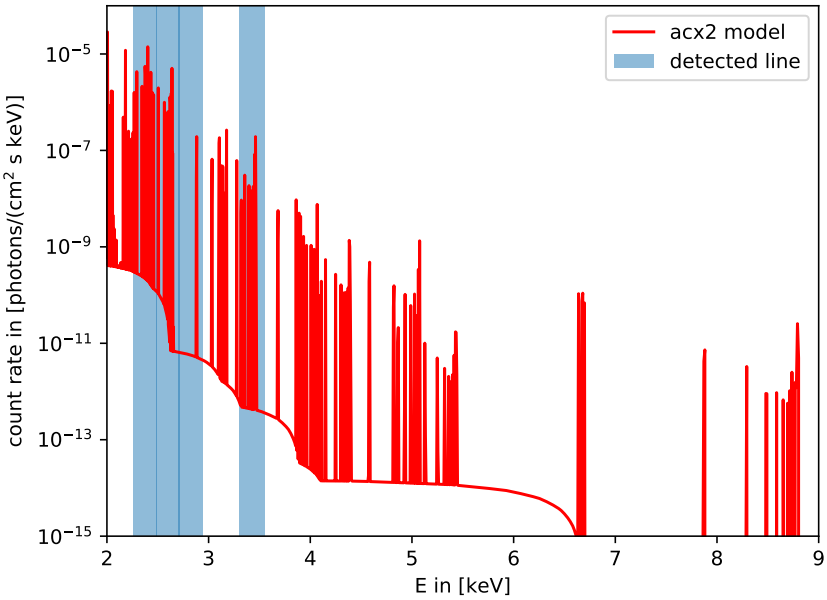

Figure A.49.: Plot showing the location of detected line features (blue) against line emission in the acx2 model (red) for the southern region in eRASS2

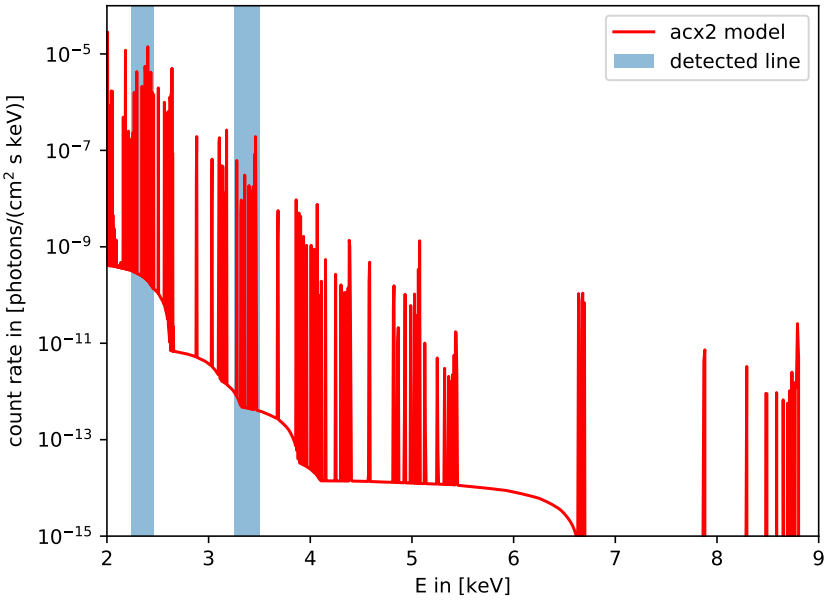

Figure A.50.: Plot showing the location of detected line features (blue) against line emission in the acx2 model (red) for the southern region in eRASS3

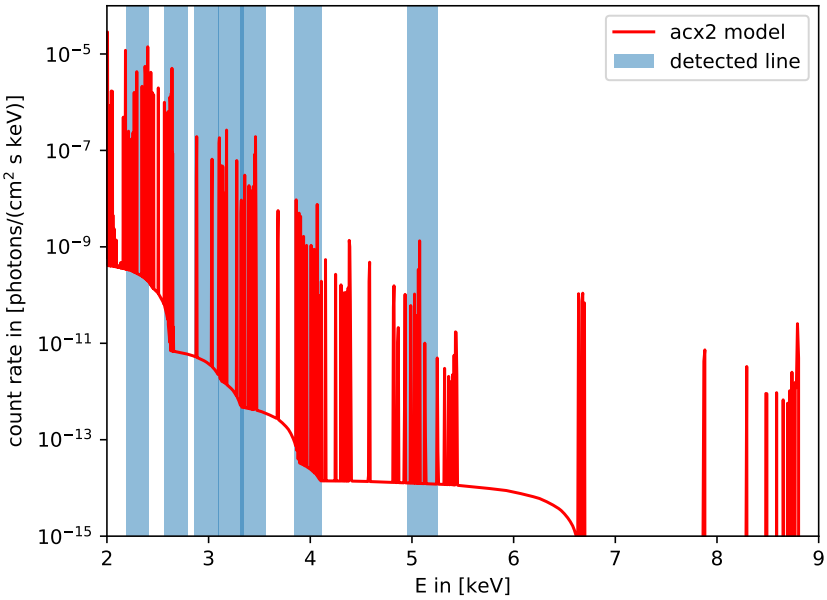

Figure A.51.: Plot showing the location of detected line features (blue) against line emission in the acx2 model (red) for the southern region in eRASS4

Erklärung

Hiermit bestätige ich, dass ich diese Arbeit selbständig und nur unter Verwendung der angegebenen Hilfsmittel angefertigt habe.